LASER (COOLING) REFRIGERATION IN ERBIUM BASED SOLID STATE MATERIALS

A Dissertation
Submitted to
the Temple University Graduate Board

In Partial Fulfillment
of the Requirements for the Degree
DOCTOR OF PHILOSOPHY

---

by
Jonathan W. Lynch
December 2015

Examining Committee Members:

Dr. Zameer Hasan, Advisory Chair, Physics
Dr. Peter Riseborough, Physics
Dr. Maria Iavarone, Physics
Dr. John Perdew, Physics
Dr. John Helferty, External Member, Temple University College of Engineering

ABSTRACT

The objective of this study was to investigate the potential of erbium based solid state materials for laser refrigeration in bulk material. A great deal of work in the field has been focused on the use of ytterbium based ZBLAN glass. Some experiments have also reported cooling in thulium based solid state materials but with considerably less success. We proposed that erbium had many attractive features compared to ytterbium and therefore should be tried for cooling. The low lying energy level structure of erbium provides energy levels that could bring obtainable temperatures two orders of magnitude lower. Erbium transitions of interest for cooling fall in the near IR region (0.87 microns and 1.5 microns). Lasers for one of these transitions, in the 1.5 micron region, are well developed for communication and are in the eye-safe and water and atmosphere transparent region.

Theoretical calculations are also presented so as to identify energy levels of the eleven 4f electrons in Er^{3+} in Cs_2NaYCl_6:Er^{3+} and the transitions between them. The strengths of the optical transitions between them have been calculated. Knowledge of such energy levels and the strength of the laser induced transitions between them is crucial for understanding the refrigeration mechanisms and different energy transfer pathways following the laser irradiation.

The crystal host for erbium was a hexa-chloro-elpasolite crystal, Cs_2NaYCl_6:Er^{3+} with an 80% (stoichiometric) concentration of erbium. The best cooling results were obtained using the 0.87 micron transition. We have demonstrated bulk cooling in this crystal with a temperature difference of ~6.2 K below the surrounding temperature. The

temperatures of the crystal and its immediate surrounding environment were measured using differential thermometry.

Refrigeration experiments using the 1.5 micron transition were performed and the results are presented. The demonstrated temperature difference was orders of magnitude smaller. Only a temperature of ~0.015 K below the temperature of the surrounding environment was observed in this case. These results are in agreement with another group's that has observed cooling, though a slightly poorer temperature difference, using this transition of erbium (Condon et. al., 2009).

Cooling was also attempted in the 0.87 micron transition of another crystal host, KPb_2Cl_5:Er, which has a concentration of about one percent of erbium. We did not observe any cooling in this crystal. However, the first cooling reports in erbium based systems were with this crystal where another group observed cooling by 0.7 K using the same transition (Fernández, García-Adeva, & Balda, 2006).

ACKNOWLEDGMENTS

I will begin by recognizing those that had a professional or academic involvement with the work that went into this dissertation. Obviously my advisor, Dr. Zameer Hasan, is at the top of that list. I would like to thank my committee for taking the time to read my dissertation and participate in the defense. Zhengle Qiu, a graduate student, who was also a member of the group, was involved in earlier work on the project and some of our work overlapped. Richard in the electronics shop and Ed and Matt in the machine shop provided equipment related support from time to time. Early work on the project was supported by a grant from the Air Force Office of Scientific Research (partly by grant numbers FA9550-05-1-0339 and F49620-96-1-0347).

I would like to acknowledge the support of many people who were not involved in my research but provided considerable support nonetheless. First and foremeost are my parents, Mark and Stacie Lynch and my sister Courtney Lynch. Their support and encouragement has been unwavering throughout my work on my dissertation.

Members of my extended family have also been particularly supportive and deserve a mention. My aunt and uncle, Judith and Milton Seeney and their children, my cousins, Lee, Sean, and Christina have my thanks for giving me a place to park near the train station, the occasional car ride in bad weather, and understanding the strange hours a graduate student sometimes needs to keep. I would have eaten many of my meals alone if not for them. My uncle, Andrew Lynch also deserves a mention for his support.

TABLE OF CONTENTS

Page

LIST OF TABLES

LIST OF FIGURES

CHAPTER 1: INTRODUCTION

The subject of this dissertation is the experimental investigation of optical refrigeration of solids. It was proposed by Pringsheim as early as 1929 (Pringsheim, 1929). It is based on an anti-stokes emission process where the absorption of a photon by a solid is followed by the emission of another photon of higher energy. The extra energy comes from the lattice vibrations or phonons. Anti-stokes emission involves the absorption of lattice vibrations, or phonons in creating a higher energy photon. This photon is eventually emitted by the solid. This annihilates phonons in the solid, thus, reducing its temperature. The energy levels involved in absorption and emission processes are electronic energy levels, typically of an optically active rare earth ion impurity in the solid. The process will be explained in greater detail in later parts of this dissertation (chapters 2 and 4).

It was not until 1995, thirty five years after the invention of the laser that laser cooling in a solid was first observed (Epstein, Buchwald, Edwards, Gosnell, & Mungan, 1995). The cooling was observed in a ZBLANP glass host doped with Yb, a rare earth lanthanide, using photothermal deflection and an infrared camera. The sample was irradiated with a diode laser working at a wavelength of 1010 nm. However, the observed temperature difference was 0.3 K.

In 2008 Epstien et. al. reported cooling in BaY_2F_8 doped with Tm. The group reported a temperature of 3 K below the surrounding temperature by irradiating their sample with 4.4 Watts from a pump laser at a wavelength of 1855 nm. Temperature was measured with a micro-bolometer camera (Patterson, et al., 2008).

Most successful early work in laser cooling in solids has made use of rare earth ions in inorganic glass or crystal hosts. Rare earth ions provide the absorption and emission characteristics necessary for cooling by anti-stokes emission. Thus far, glass hosts have provided the most successful results. Glass phonons are soft or low energy phonons. These systems have a high density of low energy phonon states and are relatively easy to fabricate or synthesize.

In 2006 a group in Spain reported a temperature drop of 0.7 K in KPb_2Cl_5 doped with Er and a temperature drop of 0.5 K in CNBZn glass doped with Er. These temperature changes were measured with an infrared thermal camera. The sample was irradiated with wavelengths of 860 nm and 870 nm (Fernández, García-Adeva, & Balda, 2006).

In 2008 (submitted, 2009 published) cooling was reported in KPb_2Cl_5 doped with Er and measured with thermocouples. The group asserted that an infrared camera was an inappropriate method of measurement because the crystal was “completely transparent in most of the mid-infrared and therefore invisible to the thermal camera.” In that case the temperature difference was even smaller, 0.0136 K when the sample was irradiated with a wavelength of 1567.6 nm (Condon, Bowman, O'Conner, Quimby, & Mungan, 2009).

In January of 2013 Zhang et. al. published a letter in Nature that reported laser cooling in semiconductors. Pumping with a 514 nm laser and measuring with a solid state 473 nm probe beam, the group reported cooling of ~40 K from 290K in CdS nanobelts. Pumping at 532 nm at 290 K the group reported a result of cooling of ~20 K. At 100 K only the wavelength of 532 nm produced cooling of 15 K (Zhang, Li, Chen, & Xiong, 2013).

Laser cooling provides an attractive alternative to other methods of cooling. Laser cooling does not require moving parts and so does not add vibrations to the surrounding system. Laser cooling does not require cryogenic liquids, which can be inconvenient over long periods of time or if weight must be limited, and so presents a smaller volume alternative to other methods. Thermo-electric coolers cannot match the low temperatures of cryogenic liquids and mechanical methods of cooling at low temperatures impose vibrations on their systems. In the case of laser cooling, cooling can be remote and localized. A small volume of material can be cooled by a focused laser instead of cooling all of the surrounding material. Some devices require a cooling apparatus that is larger than the device itself. This requirement imposes a limit on the miniaturization of technology. A smaller volume alternative, which laser cooling could provide, would allow further miniaturization of technology.

Erbium provides an attractive option for laser cooling. The wavelengths required are in atmosphere transparent and water transparent windows. That characteristic removes potential problems in designing systems to utilize the material. One of the transitions, the $^4I_{15/2}$-$^4I_{13/2}$ transition, is eye safe, making it less hazardous than some other alternatives. That wavelength is also in the region of communication lasers which is very well developed. Additionally, examining the ground state splittings of Er and Yb ions, presented in Figure 1.1, one notes that the energy difference between the electronic ground state and the first crystal field excited state in Er is 25 cm^{-1} while Yb contains an energy difference of 180 cm^{-1}. This smaller energy difference indicates that Er should allow for a lower minimum attainable temperature than Yb. Energy level calculations will be addressed in greater detail in chapter 3.

Erbium systems were not developed earlier because the energy levels are very complicated. Many upconversions and heating processes are possible. So, initial investigations showed heating.

Chapter 2 presents the experimental background of the work presented in this dissertation. Sample preparation and storage will be detailed and the experimental apparatuses utilized in the absorption and cooling experiments will be presented.

Chapter 3 addresses the electron configuration of the sample and the energy level calculations which provided the starting point for the cooling experiments. The steps of the calculations are explained and the results are presented at the end of the chapter.

Chapter 4 presents the laser cooling experiments. The necessary broadening of the energy level transitions is explained and the observed absorption spectrum of the sample is presented. The details of the experiments are explained and the results are presented.

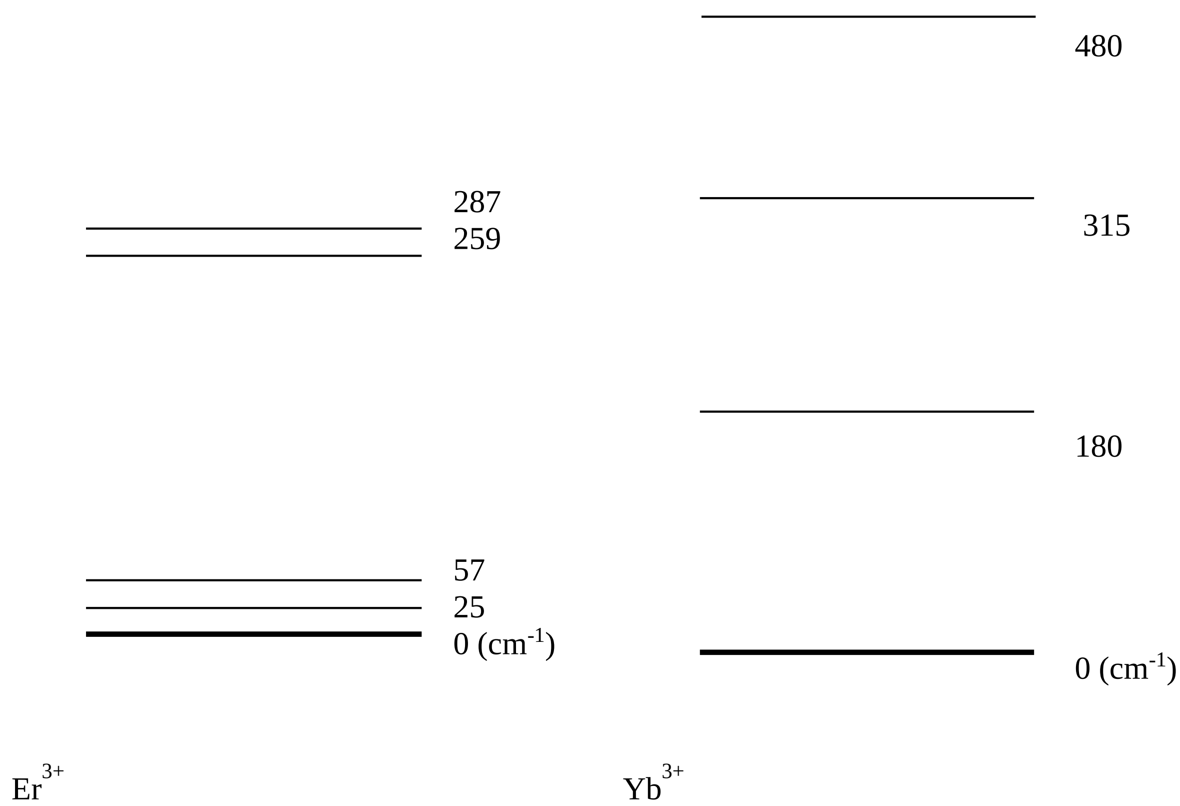

Figure 1.1 The left side of the figure displays the ground state splitting of Er^{3+} and the right side of the figure displays the ground state splittings of Yb^{3+}. Energy is displayed in units of (cm^{-1}).

Chapter 5 includes the initial attempts at cooling experiments in our system, $Cs_2NaYCl_6:Er^{3+}$ using the $^4I_{15/2}$-$^4I_{13/2}$ transition. Conclusions of this work are presented in chapter 6 and the appendix give some extra details of calculations presented in chapter 3.

CHAPTER 2: EXPERIMENTAL BACKGROUND

2.1 Sample Preparation and Storage

The crystal that was the primary focus of the work presented in this dissertation is a $Cs_2NaYCl_6:Er^{3+}$ crystal with 80 percent of the yttrium replaced with erbium. It is very hygroscopic and reacts readily with water in the surrounding atmosphere. Left unprotected from the water in the atmosphere, the crystal would hydrate. Brief exposure to the traces of water in the atmosphere would result in cloudy surface deposition on the crystal. This presented serious problems for the experiment. A hydrated surface is uneven and amorphous. Thus, it contains more topographical features that would scatter light. Increased scattered light presents three serious problems for experiments. First, it decreases the light that is absorbed by the crystal. The mechanism of laser refrigeration which is exploited in the refrigeration experiments depends upon the absorption of light in the crystal. Decreased absorption decreases the refrigeration that is possible during a given irradiation. Second, the resulting internal scattering of light in the crystal will increase the temperature of the crystal. Third, the resulting external scattering, and the reflection from the walls of the chamber which will follow will also serve to increase the temperature of the crystal and its surroundings.

Additionally, the deposition of unwanted material on the surface of the crystal provides its own difficulties. If material is left, by the hydrating process, on the surface of the crystal, it could be heated by the laser during the experiments and provide an additional source of heat to influence the temperature measurements recorded while performing the refrigeration experiments. More severe incidents of hydration would result in the chemical transformation of a significant part of the crystal or all of the crystal.

To prevent hydration, long term storage of the crystals involved sealing the crystals in a quartz ampoule under vacuum. For short term storage in the lab, the crystal was immersed in mineral oil while not in use and was kept coated in mineral oil as long as possible before it was mounted in the vacuum chamber. Handling of the crystal was carried out in neutral dry environments, preferably in nitrogen or a vacuum environment. The crystal was not touched with uncovered hands. Masks and rubber gloves were used to protect the crystals from any traces of water from hands or exhalations.

To prepare the surface before using the crystal in the laser refrigeration experiments, the crystal was polished to optical quality. The polishing was done with mineral oil and lapping films from Allied High Tech Products or mineral oil and optical window polishing material from Lambda Physik Inc. The crystal was kept coated in mineral oil throughout the polishing process to minimize hydration. In some cases, the crystal was polished inside of one of three glove boxes that were available in the lab. The largest glove box, pictured in Figure 2.1 was the most stable and allowed more than one person to work with the sample at one time. The second glove box, pictured in Figure 2.2, could be placed on a cart and moved closer to the mount of the chamber. The third and smallest glove box, pictured in Figure 2.3, was placed around the vacuum chamber so that the crystal could be both polished and mounted without exposing it to the

Figure 2.1 This glove box for polishing the crystal is larger and more stable than the others and allows more than one person to work with the sample at one time.

Figure 2.2 This glove box for polishing the crystal was kept on a cart and could be moved closer to the mount for the vacuum chamber before it was opened.

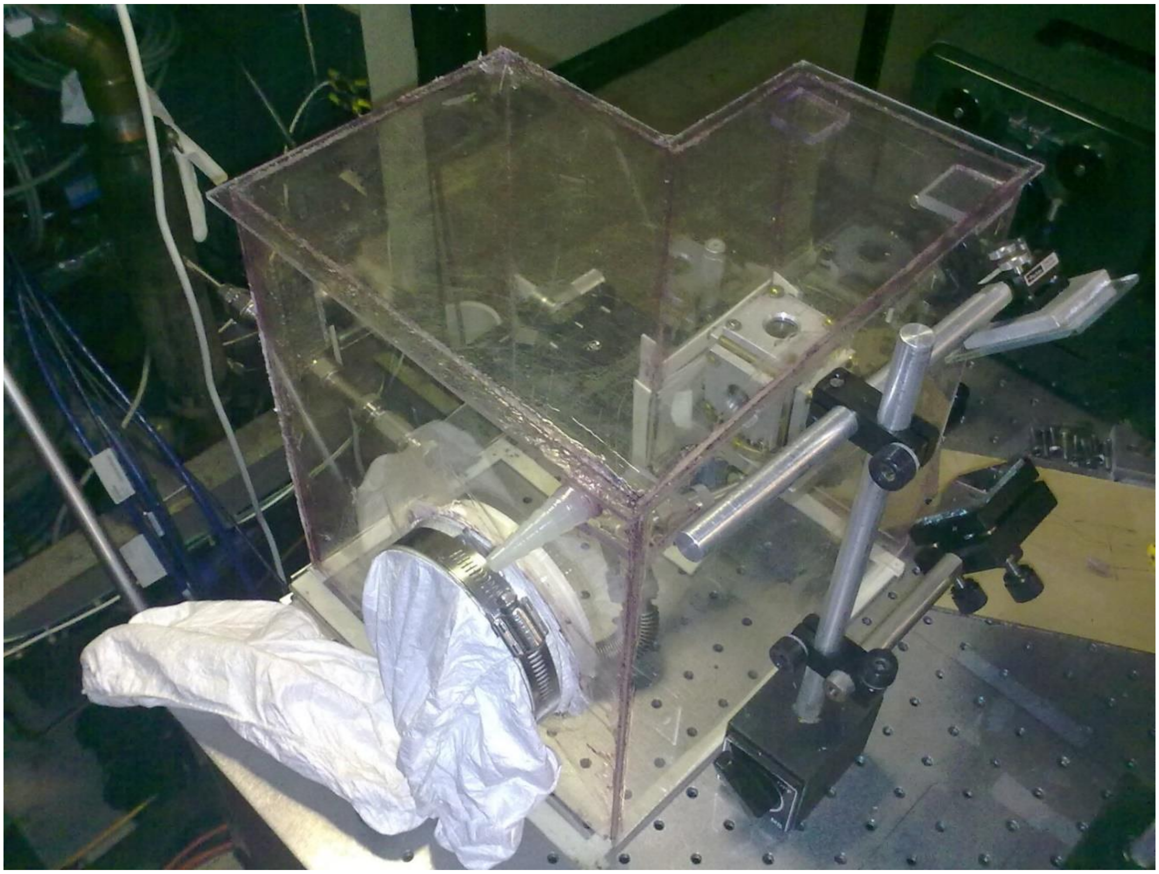

Figure 2.3 This smaller glove box for polishing the crystal covers the vacuum chamber and allows the crystal to be polished and mounted in the vacuum chamber before the glove box is removed.

atmosphere. These glove boxes were used and flushed with nitrogen gas to eliminate the amount of water vapor to which the crystal would otherwise be exposed.

The crystal was cleaned with methanol to remove any traces of mineral oil before it was mounted in the chamber for experiments. Each time the crystal is removed from the chamber, it is a good practice to polish the crystal again before it is replaced in the chamber for the next series of experiments.

While the crystal that was the primary focus of the work in this dissertation is a $Cs_2NaYCl_6:Er^{3+}$ crystal doped with an 80 percent concentration of erbium (stoichiometric), other, smaller, $Cs_2NaYCl_6:Er^{3+}$ crystals with different concentrations of erbium were also investigated. These smaller crystals had a 60 percent concentration of erbium and cross-sectional areas of ~2 mm^2 as opposed to the larger cross-section of the 80 percent crystal which was ~18 mm^2.

In the case of these smaller crystals, only the smaller glove box displayed in Figure 2.3 was used for the polishing process. And, when it was deemed useful, the crystal was encased in wax, with only one face exposed for the polishing process to provide an added layer of protection.

We also tested a different crystal host for Er, a pentachloride elpasolite ($KPb_2Cl_5:Er$), for laser refrigeration. The crystal was synthesized elsewhere and was on loan to the group. This crystal had a much smaller concentration of erbium, about one percent. However, this crystal is not hygroscopic. So, the protective measures used to prevent the hydration of the previously mentioned crystals were not necessary to safeguard the pentachloride crystal. This crystal was polished using the same method as for the hexachloride crystals.

2.2 Absorption Experimental Setup

The absorption spectrum was obtained using a Varian Cary 500 spectrophotometer. This spectrophotometer utilizes a dual beam design which allows for the application of a baseline correction. This correction minimizes any errors caused by ambient light detected by the device. The light from a lamp is passed through a monochromator before being split and sent through the sample chamber and reference chamber. This allows for monochromatic light of selected wavelengths passing through both the sample and the reference. A diagram is presented in Figure 2.4 to show the dual beam configuration on the spectrophotometer (adapted from a Varian diagram). The crystal was held in an evacuated cryostat to prevent hydration, which was placed in the spectrophotometer's sample compartment.

2.3 Laser Refrigeration Experimental Setup $^4I_{15/2}$-$^4I_{9/2}$ Transition

For the refrigeration experiments in the $^4I_{15/2}$-$^4I_{9/2}$ transition a Coherent 899 Titanium-Sapphire ring laser powered by a Coherent Sabre Argon-ion laser was used. The Argon-ion laser irradiated the Titanium-Sapphire crystal. A multi-plate birefringent

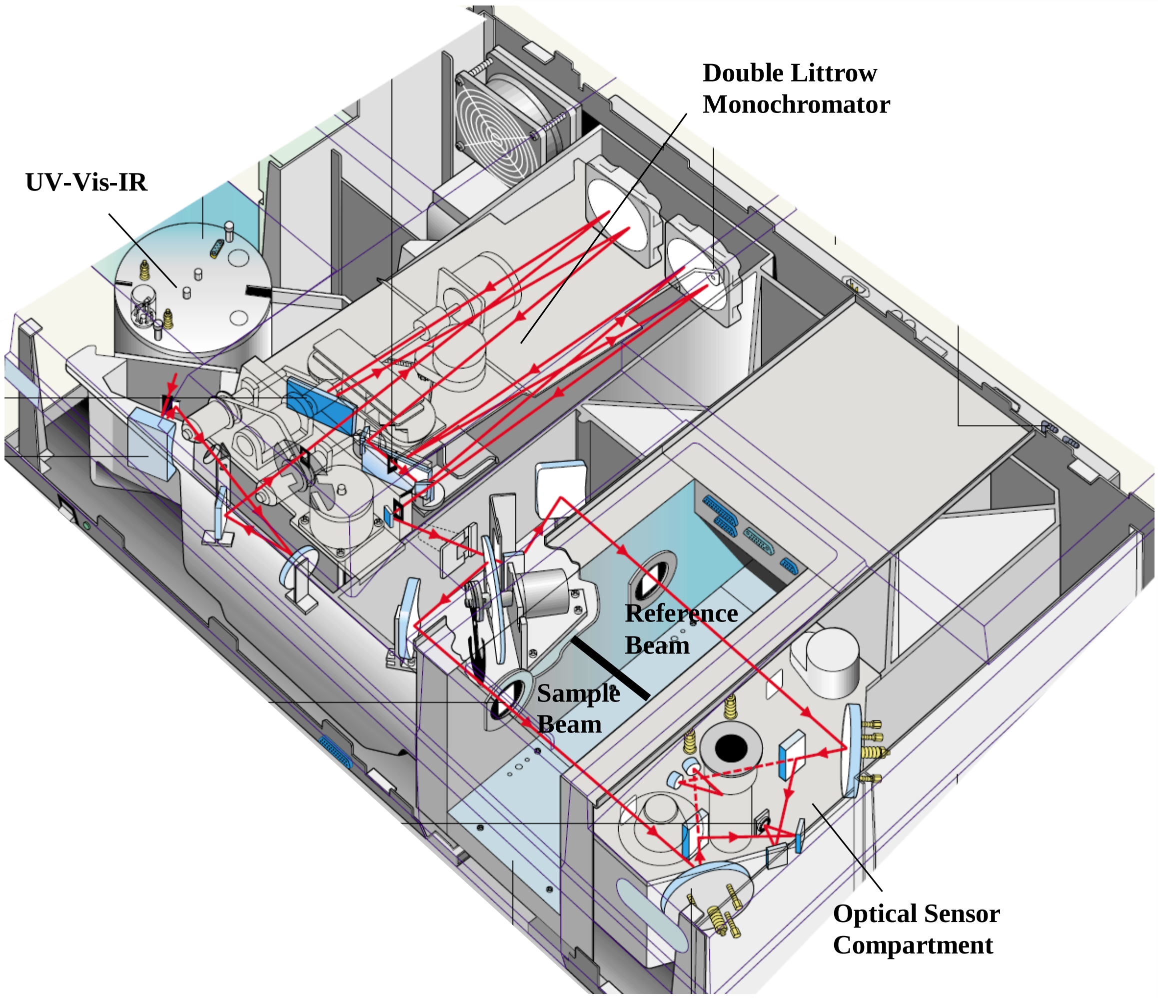

Figure 2.4 A Varian Cary 500 dual beam spectrophotometer (Agilent Cary UV-Vis)

filter in the ring laser allowed for the selection of the output wavelength which was used to irradiate the sample (Figure 2.5).

The sample was placed in a vacuum chamber, the base of which was mounted on movable stages which could be adjusted to position the chamber and sample in line with the laser beam. The vacuum chamber was evacuated with a diffusion pump. Both the chamber and the diffusion pump were fabricated in Temple University's machine shop. Antireflection coated windows and optics allowed for minimum losses due to reflection. The windows of the chamber were determined to have a coefficient of transmission of 0.92 in the region of interest. A photograph of the experimental setup appears in Figure 2.6. Figure 2.7 displays a diagram of the experimental setup and Figure 2.8 displays a more detailed diagram of the vacuum chamber.

Temperatures were measured with K type thermocouples from Omega Engineering. The thermocouple wires selected for use inside of the vacuum chamber were thin, with a diameter of .001 inches, 25.4 microns, to minimize the thermal load that the wires would introduce in the experiment. The temperature of the sample was monitored with a thermocouple junction in contact with the sample. This thermocouple will be referred to as TC1. A similar thermocouple junction monitored the temperature of the surroundings. This thermocouple will be referred to as TC2. The thermocouple wires extended to Omega Engineering K type connectors. These connectors allowed the thermocouples inside of the chamber to connect to the reference junctions outside of the chamber (Figure 2.8). The reference junctions were produced with thicker wires of chromium-nickel alloy and aluminum-nickel alloy spot welded together in Temple

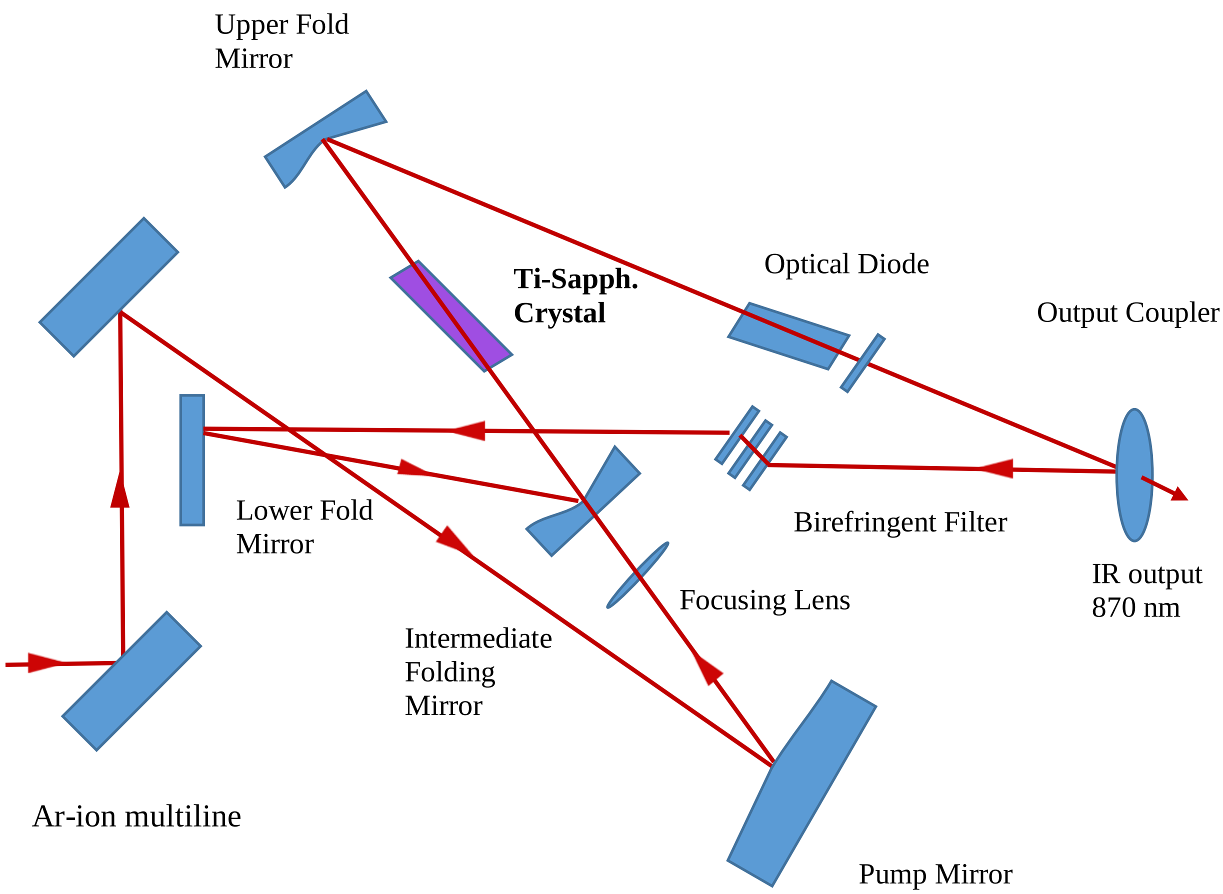

Figure 2.5 Diagram of Titanium-Sapphire laser (Coherent 899)

Figure 2.6 The photo of the experimental Setup for $^4I_{15/2}$-$^4I_{9/2}$ transition shows the vacuum chamber used to hold the sample and the Ti-Sapp laser and an iris can be seen in the upper left corner.

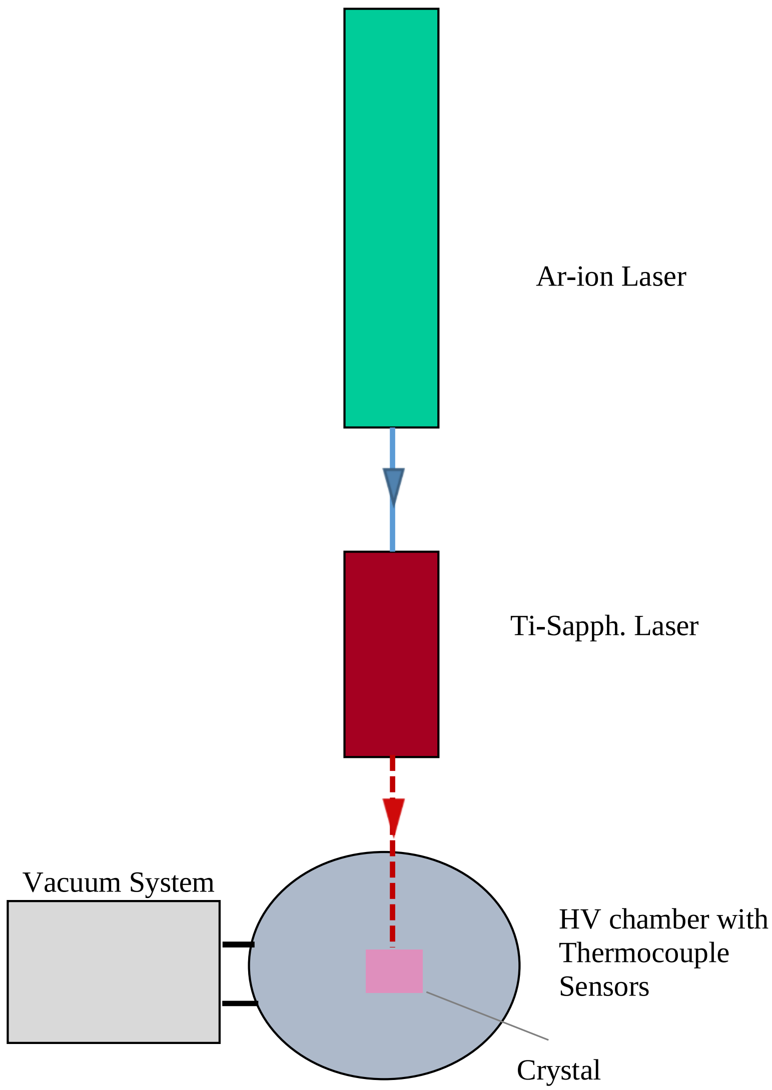

Figure 2.7 Experimental Setup for $^4I_{15/2}$-$^4I_{9/2}$ transition (Diagram)

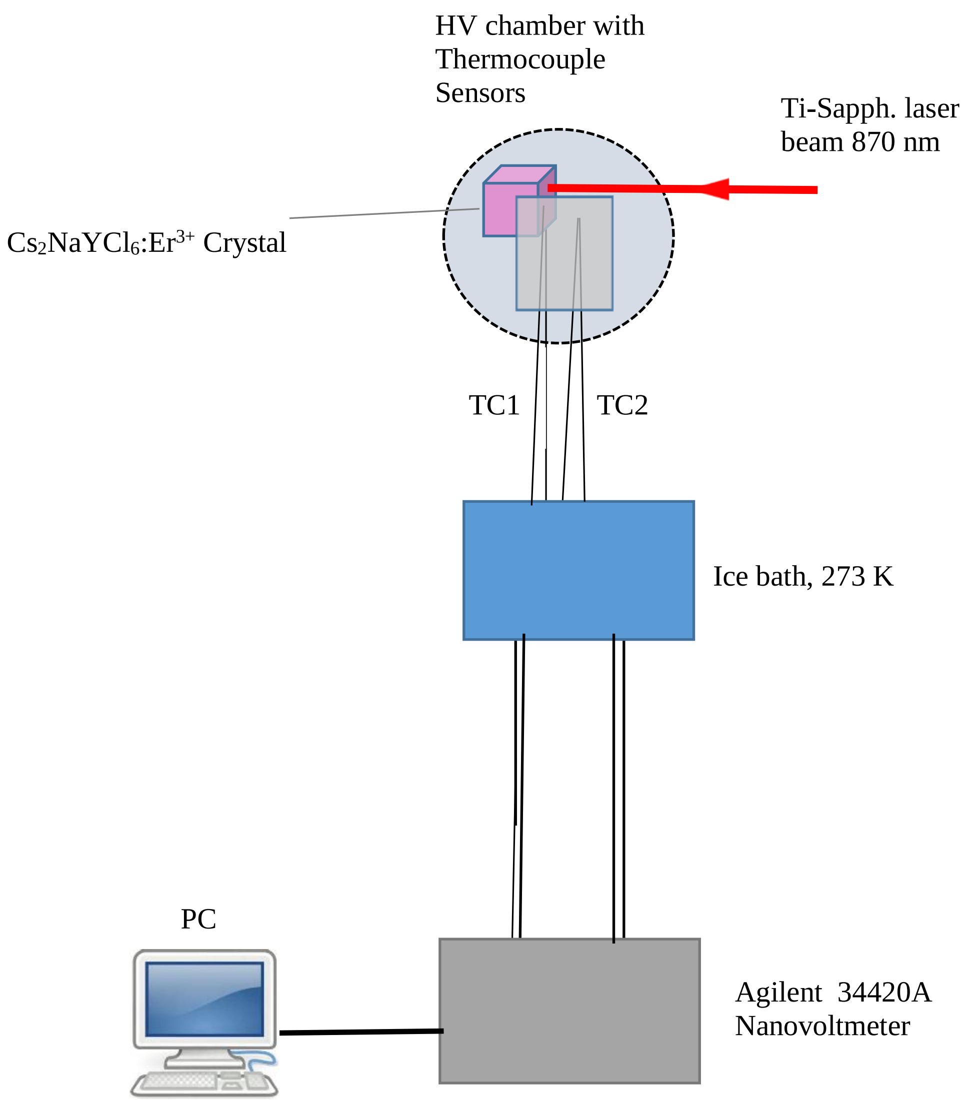

Figure 2.8 Vacuum Chamber and data collection equipment

University's machine shop. Minimizing the thermal load was not nearly as important for the reference junctions as they were not used inside of the vacuum chamber. Therefore, thicker wires were the preferred option as they offered greater durability. An ice bath at 273 K served as the reference for both TC1 and TC2. The voltage drop across the junctions of TC1 and TC2 as compared to their reference junctions was measured with an Agilent 34420A digital nano multimeter and the difference between TC1 and TC2 and their reference junctions was recorded at fixed intervals. The data was collected via a connection from the Agilent 34420A to a PC established with an RS-232 cable and using software, developed by another member of the research group, set to record alternating readings from TC1 and TC2 at fixed intervals (Figure 2.8).

In a typical laser refrigeration experiment the data collection began before the sample was irradiated. This established an initial difference between the voltages from thermocouples TC1 and TC2 as the base voltage difference to account for the initial difference during analysis. This will be explained in greater detail later. The sample was then irradiated for a set amount of time determined before the start of the data collection. After that determined amount of time, Δt, the laser was shut off or blocked and the collection continued to record the changing temperatures of the sample and the surrounding chamber as the sample warmed up and the surrounding cooled down to a stable common temperature.

For the data collected on or before 6/24/2010 the experiments utilized a mounting for the crystal and the thermocouple wires that was built into the base of the chamber. Male K type thermocouple connectors were inserted into the base of the chamber and the openings were sealed with a Loctite sealant compound. Additional metal prongs from another disassembled male K type connector was attached to allow the use of a female K type connector inside the chamber (Figure 2.9). The fine thermocouple wires that formed TC1 and TC2 in the chamber connected to the contacts on the connectors and extended upward toward the sample. The reference junctions outside of the chamber were connected to the contacts of female K type thermocouple connectors which were plugged into the male connectors that extended from the base of the chamber. Whenever possible, the junction of TC1 was placed in contact with the crystal without any adhesive. However, when necessary, a small an amount of glue as possible was used to stabilize the crystal and secure TC1 to the crystal. Using a Cary 500 spectrophotometer, it was determined that this glue did not absorb a significant amount of light at the wavelengths used for our experiments.

2.4 Laser Refrigeration Experimental Setup $^4I_{15/2}$-$^4I_{13/2}$ Transition

For the cooling experiments in the $^4I_{15/2}$-$^4I_{13/2}$ Transition a diode laser with a tunable cavity from Thorlabs was used to provide the pump beam, the TLK-L1550M. The diode laser had a peak wavelength of 1550 nm and the adjustable cavity allowed the selection of the output wavelength. The cavity output had an optional fiber optic cable attachment to allow for easier positioning of the beam. The experiments designed to

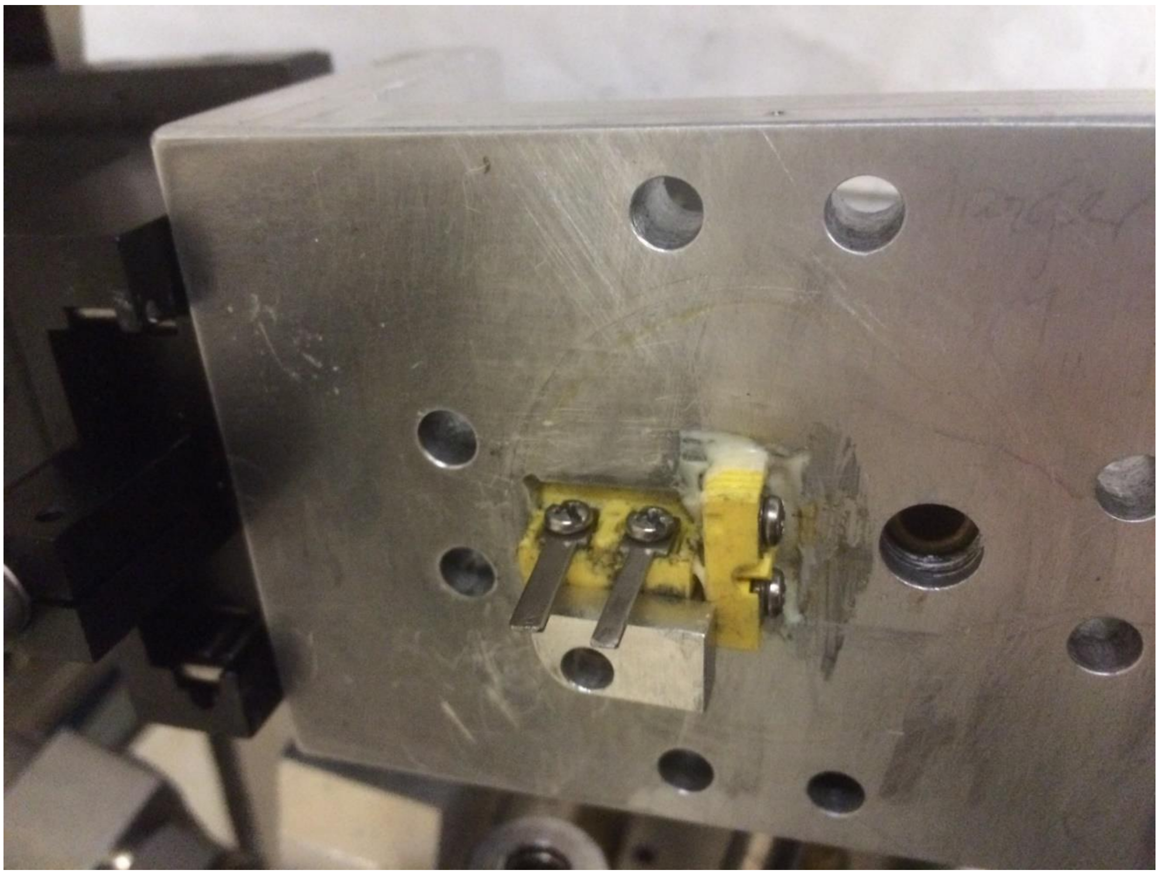

Figure 2.9 K-type thermocouple connectors inserted into the base of the vacuum chamber allow for the connection between the fine wire thermocouple junctions inside the vacuum chamber to the reference junctions in the ice bath outside of the vacuum chamber

investigate this transition utilized the same vacuum chamber and vacuum pump system that was used in the experiments to investigate the $^4I_{15/2}$-$^4I_{9/2}$ transition (Figure 2.10).

Some additional difficulties arose during the setup for the experiments in this transition. Since the peak laser wavelength is so much farther into the infrared region, there was no visible portion of the beam that could be used for alignment. To check the beam position outside of the chamber, we utilized an IR detection card which contained a material that would react to exposure to infrared light by fluorescing. To check the alignment of the beam once it entered the chamber, the wavelength was tuned to 1553 nm. At this wavelength there is significant absorption in one of the Er^{3+} ion's electronic transitions and fortunately it causes green upconversion which is very clearly visible. This green emission was used to verify the alignment of the beam inside of the vacuum chamber.

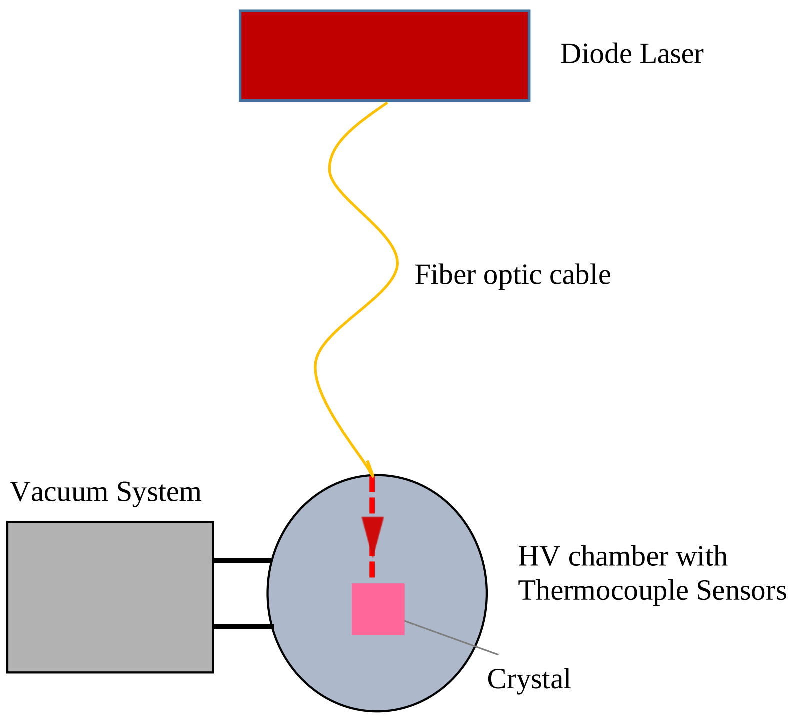

Figure 2.10 Experimental setup for the ${}^4I_{15/2}$-${}^4I_{13/2}$ transition

CHAPTER 3: THEORETICAL BACKGROUND FOR ENERGY LEVEL CALCULATIONS

3.1 Introduction

This chapter includes a description of the theoretical background relevant to the calculation of energy levels and wavefunctions of Er^{3+} in a single crystal, Cs_2NaYCl_6. The results of these calculations are presented at the end of the chapter. The calculations were performed only for the Cs_2NaYCl_6:Er^{3+} crystal, which, as mentioned previously, was the sample used in the majority of the work presented in this thesis. This crystal is a cubic system. Cubic systems possess several advantageous properties which make them considerably easier to utilize. Cubic systems like this crystal have only two adjustable crystal field parameters and Er^{3+} has a relatively large number of electronic energy levels, so the parameters are much more easily identified. Cubic transitions are weakly allowed by the cubic symmetry. This leads to sharp transitions which are observed without ambiguity. For these reasons, cubic systems have been very thoroughly investigated both theoretically and experimentally. While considerable experimental data is available for non-cubic systems, these systems cannot be tested by theory the way that cubic systems can.

Although data will be presented for Er^{3+} in a pentachloride crystal in chapter 4, where heating was observed rather than refrigeration, energy level calculations have not been performed for that sample. In a non-cubic crystal field, energy levels could not be easily identified. In the case of a non-cubic crystal field the number of parameters increases and more splitting of the energy levels take place. The transitions are less identifiable due to electric dipole selection rules. For all of these reasons, only the calculations for the cubic system have been presented.

A calculation of the energy levels of Er^{3+} in Cs_2NaYCl_6 is useful in understanding the energy levels and the transitions between them that are involved in the cooling processes. It will help in predicting the transition probabilities of the relevant cooling processes. With this information at hand, one has wavelength regions to investigate in laser refrigeration experiments.

3.2 Er^{3+} Doping in Cs_2NaYCl_6

3.2.1 Structure

The Er in the Cs_2NaYCl_6 crystal replaces Y^{3+} and appears as Er^{3+} which sits at a site with octahedral symmetry. Figure 3.1 displays the crystal structure surrounding one of the Er^{3+} ions. In this crystal, the Erbium has $4f^{11}$ optically active electrons. Therefore, the energy levels of this system for any optical transitions of these electrons are addressed. In Cs_2NaYCl_6 these transitions fall within the band gap of the crystal. The lattice parameter of Cs_2NaYCl_6 is 10.740 Å. The separation between Y^{3+} and its nearest neighbors, Cl^- is 2.62 Å (Woods, et al., 1993). The crystal remains cubic for all concentrations of Er^{3+} up to 100 percent (stoichiometric).

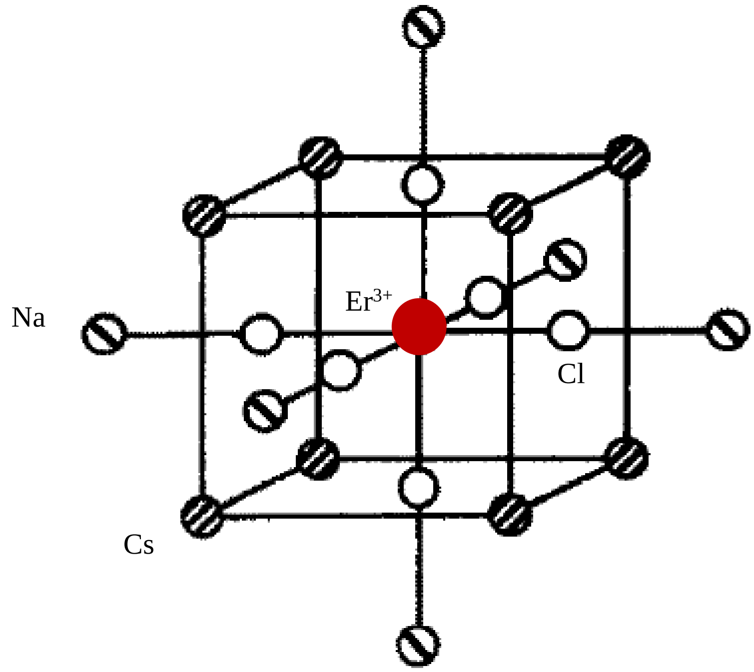

Figure 3.1 The crystal structure of the elpasolite Cs_2NaYCl_6:Er with Er at the center. Er^{3+} replaces Y at a cubic site (Woods, et al., 1993)

Er, with 11 electrons in its incomplete shell has a $4f^{11}$ configuration. The complete outer shells, 5s and 5p, shield the 4f electrons from the effect of any environmental influences such as the bulk electrons and the ionic lattice in its host crystal.

3.2.2 Electronic Energy Levels

Er^{3+} with $4f^{11}$ electrons is very similar in its energy levels to Nd^{3+} which has only 3 electrons in the 4f shell. All atomic energy level calculations can be performed as 3 holes in a complete 4f shell, which would have 14 electrons.

In the following calculations the $4f^{11}$ electron system will be treated as a $4f^3$ hole system. The energy levels will be calculated taking all atomic interactions into consideration for Er^{3+}. The

energy levels and wavefunctions, thus calculated for the Er^{3+} ion, will be referred to as barycenters of Er^{3+} energy levels.

Once the barycenter values are obtained, the crystal field perturbation can be applied in the calculation scheme to arrive at the crystal field energy levels and wavefunctions. These can be used as the calculated energy levels and wavefunctions for the relevant transitions for Er^{3+} in Cs_2NaYCl_6.

The calculations were carried out using of a series of computer programs which were developed elsewhere for previous studies. (Hasan & Richardson, 1982) These programs first calculate the barycenter energy levels and wavefunctions. The barycenter values are then used as a basis to calculate the energy levels and wavefunctions that result from the application of the crystal field in the Cs_2NaYCl_6 crystal host.

The first step in the process establishes the states of the Er^{3+} $4f^{11}$ system that will be used to calculate the different energy levels. The result is the generation the barycenter L-S-J state labels:

$$|\psi[SL]J\rangle$$

such as the $^4I_{15/2}$, the ground state. These states will be used in the subsequent steps to calculate the barycenter energy levels and wavefunctions.

The next step in calculating the energy levels and identifying the wavefunctions is to take the electrostatic interaction between the $4f^{11}$ electrons into account.

In a crystal, the Hamiltonian relevant to the energy levels of Er^{3+} has two major contributions, one from the free-ion Hamiltonian and the other from the crystal field Hamiltonian.

The Hamiltonian can be written as:

$$H = H_{fi} + H_{CF} \qquad \text{(Eq 3.1)}$$

In Er^{3+}, in optical transitions, the energy levels of the unfilled $4f^{11}$ shell are involved. All of the electron shells, except the 4f electron shell, are full and therefore are spherically symmetric. As a result, they do not provide significant contributions to the relative energy levels of the 4f electrons. The crystal field has a very small effect for shielded 4f electron energy levels. Therefore, the first step of the calculation is to determine the barycenter energy levels.

In this case, the free-ion Hamiltonian can be written as:

$$H_{fi} = -\frac{\hbar^2}{2m}\sum_{i=1}^{N}\nabla_i^2 - \sum_{i=1}^{N}\frac{Z^* e^2}{r_i} + \sum_{i>j}^{N}\frac{e^2}{r_{ij}} + \sum_{i=1}^{N}\xi(r_i)\vec{s}_i \cdot \vec{\ell}_i + H_{CI} \qquad \text{(Eq 3.2)}$$

In equation 3.2, the first term represents the kinetic energy contribution. It adds to the energy of each state but a constant energy term and does not influence the relative energy of the states arising from the Er^{3+} $4f^{11}$ electrons. Therefore, this contribution can be neglected for the optical transitions which occur between the energy levels of $4f^{11}$ electrons.

The second term represents the contribution from the screened charge of the nucleus. Like the kinetic energy term, this term only adds a constant value to each state and does not affect the degeneracy of the 4f states. So, it can be neglected as well.

The third term represents the electrostatic interaction. The fourth term represents the spin-orbit interaction. The final term represents the configuration interaction. It is another electrostatic interaction but the interaction is between electrons in different configurations. This will be addressed in more detail later in this section.

For calculating the energy differences between $4f^{11}$ |[LS]JM> states, the relevant Hamiltonian consists of terms from the electrostatic interaction, the spin-orbit interaction, the configuration interaction and the crystal field interaction. So, from here on, The Hamiltonian for our system will be written:

$$H' = H_{el} + H_{SO} + H_{CI} + H_{CF} \quad \text{(Eq 3.3)}$$

Where H_{el}, H_{SO}, and H_{CI} comprise the barycenter Hamiltonian and H_{CF} is the contribution from the crystal field. The eigenvalues and eigenfunctions of the barycenter Hamiltonian are calculated first. Then the crystal field is taken into account as a perturbation.

The matrix elements are obtained for this Hamiltonian in the rare earth metal-ion basis:

$$| \alpha[SL]JM \rangle$$

Where α represents seniority in case more than one |[LS]J> states appear in the $4f^{11}$ configuration; *S* represents total spin, *L* represents orbital angular momentum, *J* represents the total angular momentum, and M represents the component of the total angular momentum in a magnetic field.

3.2.3 The Electrostatic Interaction

The electrostatic interaction is the interaction in the free-ion Hamiltonian that provides the largest contribution. Therefore, it was the first interaction taken into account for these calculations. Since it is the difference in energy levels that is of interest, all terms that would add a constant value to all f^n states have been neglected and the electrons in the f^n configuration are included in the H_{el} calculation.

The electrostatic interaction Hamiltonian can be written as:

$$H_{el} = \sum_{i>j} \frac{e^2}{r_{ij}} \qquad \text{(Eq. 3.4)}$$

Where $i \neq j$ and the indices run over the $4f^{11}$ electron pairs.

The electrostatic matrices can be computed in terms of the Slater radial integrals or in terms of the Racah radial integrals which will be defined later in this section. The Slater radial integral is defined (Hufner, 1978) in the expression:

$$F^k = e^2 \int \left(\frac{r_<^k}{r_>^{k+1}} \right) R_{4f}^2 (r_1) R_{4f}^2 (r_2) dr_1 dr_2 \qquad \text{(Eq. 3.5)}$$

Where $r_>$ and $r_<$ are the larger and smaller radii of the two electrons. Since ℓ=3 for the f electrons, the only non-vanishing terms are F_0, F_2, F_4, and F_6.

In order to avoid large denominators, these radial integrals are sometimes rewritten in another form:

$$F^0 = F_0 \qquad \text{(Eq. 3.6)}$$

$$F^2 = 225F_2 \qquad \text{(Eq. 3.7)}$$

$$F^4 = 1089F_4 \qquad \text{(Eq. 3.8)}$$

$$F^6 = (184041/25)F_6 \qquad \text{(Eq. 3.9)}$$

The calculation utilized the reduced matrices presented in Nielson and Koster's tables (Nielson & Koster, Spectroscopic Coefficients for the pn, dn, and fn Configurations, 1963). For this f^n configuration, Nielson and Koster presented the expansion in terms of the Racah radial integrals. Using these programs, F_2, F_4, and F_6 are treated as adjustable parameters.

The matrix elements of H_{el} in the stated basis, using the Racah integrals, are given by

$$\langle \alpha[SL]JM \mid H_{el} \mid \alpha'[S'L']J'M' \rangle = \delta(S,S')\delta(L,L')\delta(J,J')\delta(M,M')\sum_{k=0}^{3} e_k E^k \qquad \text{(Eq. 3.10)}$$

Where $e_k = e_k(\alpha,\alpha',S,L)$ and E^k are the Racah radial integrals.

The relationship between the Slater radial integrals and the Racah radial integrals are defined in the following equations 3.11-3.14.

$$E^0 = F_0 - 10F_2 - 33F_4 - 286F_6 \quad \text{(Eq. 3.11)}$$

$$E^1 = \frac{70F_2 + 231F_4 + 2002F_6}{9} \quad \text{(Eq. 3.12)}$$

$$E^2 = \frac{F_2 - 3F_4 + 7F_6}{9} \quad \text{(Eq. 3.13)}$$

$$E^3 = \frac{5F_2 + 6F_4 - 91F_6}{3} \quad \text{(Eq. 3.14)}$$

3.2.4 The Spin-Orbit Interaction

Once the electrostatic interaction was addressed, the spin-orbit interaction, which provides the next largest contribution, was considered at the second stage of the calculation. It is the spin-orbit coupling that effects the mixing of states which have the same J value and different L and S values (Hufner, 1978). While the electrostatic matrix elements do not change when comparing configurations with n electrons and n holes, the matrix elements of the spin-orbit interaction change sign when comparing such configurations. So, when treating the energy level calculations as a system with 3 holes, the matrix elements presented in Nielson and Koster's tables for f^3 electrons may be used. However, the changed sign must be taken into account. The spin-orbit interaction Hamiltonian can be written as:

$$H_{so} = \sum_i \xi(r_i)\vec{\ell}_i \cdot \vec{s}_i \quad \text{(Eq. 3.15)}$$

Where

$$\xi(r_i) = \frac{\hbar^2}{2m^2c^2r_i}\frac{\partial U(r_i)}{\partial r_i} \qquad \text{(Eq. 3.16)}$$

Where $U(r_i)$ is the central field potential.

The matrix elements for H_{so} in this basis are given by

$$\begin{aligned}&\varsigma_{n\ell}\delta(J,J')\delta(M,M')(-1)^{J+L+S'} = \langle \alpha[SL]JM \mid H_{SO} \mid \alpha'[S'L']J'M'\rangle \\ &\times[\ell(\ell+1)(2\ell+1)]^{\frac{1}{2}}\begin{Bmatrix} L & L' & 1 \\ S' & S & J\end{Bmatrix}\langle \alpha SL \parallel v^{(11)} \parallel \alpha' S'L'\rangle\end{aligned} \qquad \text{(Eq. 3.17)}$$

Where

$$\varsigma_{n\ell} = \int_0^\infty [R_{n\ell}(r)]^2\,\xi(r)r^2dr \qquad \text{(Eq. 3.18)}$$

And ℓ=3 for f^n configurations.

$\varsigma_{n\ell}$ is the spin-orbit coupling parameter. Based on the assumed equivalence of all of the 4f electrons, it was assumed that the parameter remains equal for all of the 4f electrons (Hufner 1978). This is treated as an adjustable parameter in these calculations.

The matrix elements of the $v^{(11)}$ operator are provided by Nielson and Koster's tables. (Nielson & Koster, Spectroscopic Coefficients for the pn, dn, and fn Configurations, 1963).

3.2.5 The Configuration Interaction

Despite the fact that the electrostatic interaction and the spin-orbit interaction are the most important in calculating barycenter energy levels in our system, and provide much larger contributions than the configuration interaction, discrepancies may exist when comparing calculated values to the experimental results. In addressing the previous interactions, the configuration interaction has been neglected. The interaction of the $4f^n$ configuration with configurations of the same parity must be considered (Wybourne, 1965).

The configuration interaction is a Coulomb interaction between the electrons of different configurations in which they can be arranged. It is the interaction which provides the smallest contribution of the barycenter interactions and is applied as a correction to the electrostatic interaction. Without the configuration interaction, the calculation scheme assumes that the model in use is a complete and perfect match for the $4f^n$ configuration. For example, considering the f^n configuration, $f^{n-1}d^1$ and $f^{n-2}d^2$ are two possible configurations of the same electrons and these configurations interact with the $4f^n$ configuration.

A configuration interaction potential is applied such that diagonal corrections are applied to the electrostatic matrices.

$$\left(\overline{\psi} \mid V_{ci} \mid \overline{\psi}'\right) = \delta(\psi, \psi')\left[\alpha L(L+1) + \beta G(G_2) + \gamma G(R_7)\right] \qquad \text{(Eq. 3.19)}$$

Here

$$\psi \equiv \psi[SL]JM \qquad \text{(Eq. 3.20)}$$

And α, β, and γ are treated as adjustable parameters and G represents the Coulomb repulsion energy.

$G(G_2)$ and $G(R_7)$ represent eigenvalues of Casimir operators of the G_2 and R_7 groups which classify the states of the f^n configuration. More detailed information about these groups is provided by Wybourne (Wybourne, 1965).

In this classification scheme, a set of indices is assigned to each ψ[SL] term. Said indices are listed as $U=(u_1,u_2)$ and $W=(w_1,w_2,w_3)$ and are provided in the state listings of Nielson and Koster's table.

The eigenvalues are given by the equations:

$$((u_1,u_2)|\,G(G_2)\,|\,(u_1,u_2)) = \frac{1}{12}\left(u_1{}^2 + u_1u_2 + u_2{}^2 + 5u_1 + 4u_2\right) \qquad \text{(Eq. 3.21)}$$

$$((w_1,w_2,w_3)|\,G(R_7)\,|\,(w_1,w_2,w_3)) = \frac{1}{2}\begin{bmatrix} w_1(w_1+5) \\ + w_2(w_2+3) + w_3(w_3+1) \end{bmatrix} \qquad \text{(Eq. 3.22)}$$

3.2.6 Crystal Field Interaction

Once the barycenter energy levels and wavefunctions had been determined, the crystal field contribution was applied.

Examining a free atom or ion, one would find spherical symmetry with a degeneracy of (2J+1) for each energy level. When a crystal field is introduced, that spherical symmetry is removed and the field effects a splitting of each level. According to Kramers' Theorem, in odd electron systems there is a twofold degeneracy in energy levels that arises due to unpaired spin that electric fields cannot remove. Only a magnetic field or exchange interactions between paramagnetic ions can remove that remaining degeneracy. So, for an odd electron system in a cubic environment, with the application of the crystal field, the spin-orbit multiplets will be split into crystal field states with, at most, 4-fold degeneracy remaining intact. A low symmetry crystal field will lift the 4-fold degeneracy as well and only Kramer's doublets will result.

Our system, which utilizes Er^{3+}, is a $4f^{11}$ system. The relevant electrons are shielded by the outer shell. So, the crystal field contribution is very small. Its contribution is less than one tenth the magnitude of the spin-orbit interaction's contribution. This means that the contribution from the crystal field will be applied as a perturbation. Figure 3.2 displays the radial charge distribution of a rare earth material and demonstrates that the 4f electron shell is well within the 5s, 5p, and 6s shells (Freeman & Watson, 1962). This serves to shield the electrons of the 4f shell from the influence of the rest of the crystal.

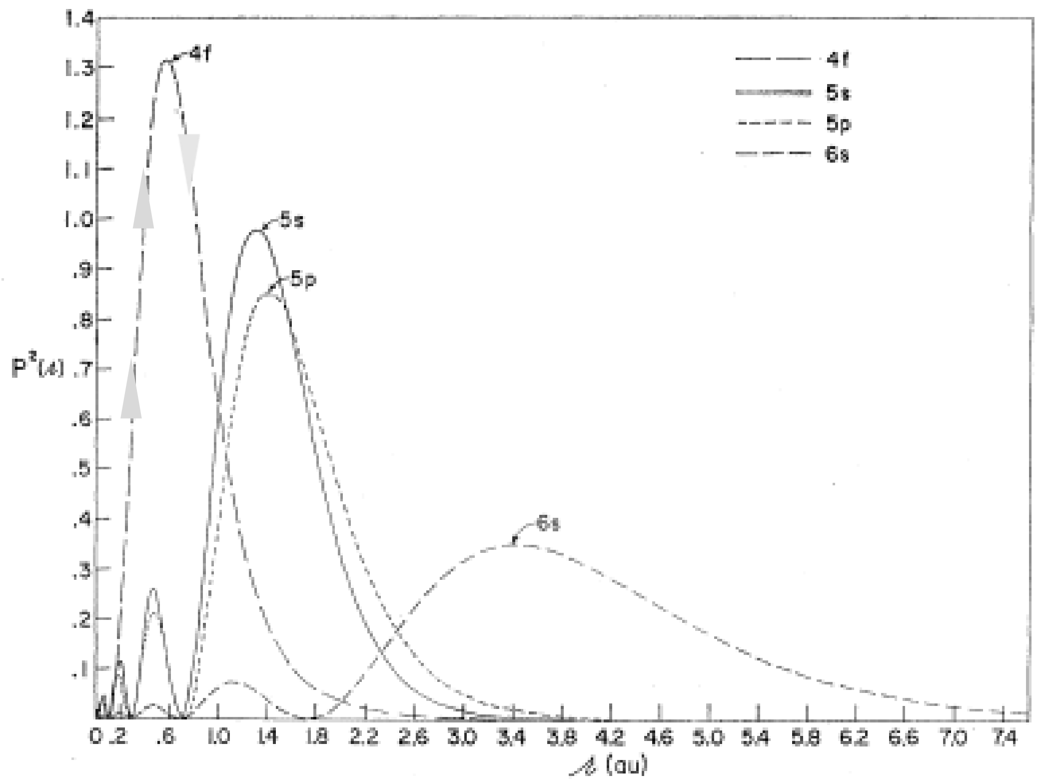

Figure 3.2 Radial charge distribution $P^2(r)$ as a function of r, the distance from the nucleus where r=0, for Gd^+. The 4f shell is well isolated from the crystal field by 5s, 5p, and 6s (Freeman & Watson, 1962)

The crystal field interaction is an electrostatic interaction. So the relevant term in the Hamiltonian could be written in terms of the charge distribution, a function of position. This would result in the term expressed in the form:

$$V(\vec{r}) = -\int \frac{e\rho(\vec{R})d\tau}{|\vec{R}-\vec{r}|} \qquad \text{(Eq. 3.23)}$$

Here, ρ is the charge distribution. R is a general point in the system and r is the electron position (Wybourne, 1965).

Without the perturbation applied, the eigenfunctions from the barycenter Hamiltonian will be spherically symmetric. So, the crystal field contribution can be expressed in terms of the crystal field parameters in spherical notation and the solid harmonics as:

$$H_{CF} = \sum_{i}\sum_{k=0}^{\infty}\sum_{q=-k}^{k} B_q^k C_q^{(k)}(i) \qquad \text{(Eq. 3.24)}$$

Equation 3.23 which is the crystal field contribution of the Hamiltonian, the H_{CF} term, B_q^k represents the crystal field parameters in spherical notation and $C_q^{(k)}(i)$ represents the solid harmonics in the coordinate of the i^{th} ℓ^n electron. Here:

$$B_q^k = -e\int \rho(R)\frac{r_<^k}{r_>^{k+1}}(-1)^q C_{-q}^{(k)}(\Theta,\Phi)d\tau \qquad \text{(Eq. 3.25)}$$

$$C_q^{(k)} = \left(\frac{4\pi}{2k+1}\right)^{\frac{1}{2}} Y_{kq} \qquad \text{(Eq. 3.26)}$$

Since the concern is with the crystal field splitting of the energy levels, the first term in the expansion can be ignored. B_0 is spherically symmetric and, in the first approximation, it provides a uniform shift to all of the energy levels and tells us nothing about the differences in the energy levels.

Matrix elements of H_{cf} in the $|\alpha[SL]JM\rangle$ basis are given by

$$\left\langle \alpha[SL]JM \mid H_{cf} \mid \alpha'[S'L']J'M' \right\rangle = \delta(S,S')\sum_{k,q} B_q^k \left\langle \alpha[SL]JM \mid U_q^{(k)} \mid \alpha'[SL']J'M' \right\rangle \times \left\langle \ell \parallel C^{(k)} \parallel \ell \right\rangle \qquad \text{(Eq. 3.27)}$$

Where $U_q^{(k)}$ is the intraconfigurational unit tensor.

The crystal in question, Cs_2NaYCl_6:Er has octahedral, O_h symmetry. This symmetry leads to a crystal field expansion of:

$$B_0^4\left[U_0^{(4)} + \sqrt{\frac{5}{4}}\left(U_4^{(4)} + U_{-4}^{(4)}\right)\right] + B_0^6\left[U_0^{(6)} - \sqrt{\frac{7}{2}}\left(U_4^{(6)} + U_{-4}^{(6)}\right)\right]$$

With the cubic crystal field one is left with two non-spherically symmetric components which are treated as parameters that are adjusted to fit the experimentally observed spectra (Hasan & Richardson, 1982). The U_q^k terms are provided in Nielson and Koster's tables. The B_q^k terms are treated as adjustable parameters.

3.2.7 Parameters

As identified earlier in this section, the complete calculations utilize nine adjustable parameters. Seven of those parameters arise from considering the barycenter interactions. The remaining two parameters arise from the crystal field interaction. The seven parameters relevant to the barycenter interactions could be found in previous studies and used as a starting point for the barycenter calculations. These are given by Hufner (Hufner, 1978). The values of the parameters are displayed in Table 3.1. Taking those values as a starting point left the two crystal field parameters.

In our system, there are a large number of spin-orbit multiplets that will split under the crystal field. Er has the richest spectrum of any rare-earth in a crystal. The large number of states compared to the small number of crystal field parameters allows calculations to define those parameters very well. The parameters were adjusted in reiteration to obtain an excellent fit between experimental and theoretical data compared to other lanthanides. For the values obtained for the crystal field energy levels and states, presented later in this section, the crystal field parameters were set to $B_0^4 = 1608\ cm^{-1}$ and $B_0^6 = -195\ cm^{-1}$.

3.3 Results

The energy levels and states obtained from the barycenter calculations, before the application of the crystal field, are presented in Table 3.2. The crystal field energy levels and states, which were calculated after the barycenter values were obtained, are presented in Table 3.3.

3.4 Optical Transition Probabilities

The transition most thoroughly investigated for laser refrigeration here, the $^4I_{15/2}$-$^4I_{9/2}$ transition, is forbidden by some of the relevant selection rules. Those selection rules are: $\Delta S = 0$, $\Delta L = 0, \pm 1$ and $\Delta J = 0, \pm 1$ but not 0 to 0. The transition is between f^n electrons. For these states $\ell = 3$ ($\Delta\ell = 0$ for these transitions which is forbidden by electric dipole selection rules). In this transition the J value changes by 3. Since $\Delta J \neq 0, \pm 1$ for the electric dipole transition, the transition is forbidden by another selection rule. These circumstances make the probability of this transition far less than the probability of transitions which do not violate this selection rule.

The transition properties responsible for cooling are vibronic transition properties in which a phonon or phonons combine with an electronic state and change the involved energy values. This will be addressed in in chapter 4, which explains the theoretical background of laser refrigeration in greater detail.

Parameter	Value in cm^{-1} (8.0655 cm^{-1} = 1 meV)
F2	436 cm^{-1}
F4	64 cm^{-1}
F6	6.67 cm^{-1}
ζ_{SO}	2370 cm^{-1}
α	15.9 cm^{-1}
β	-632 cm^{-1}
γ	2017 cm^{-1}

Table 3.1 Free Er^{3+} ion adjusted parameters for the $4f^{11}$ energy level calculations. F_2, F_4, and F_6 are parameters for the electrostatic interaction. ζ_{SO} is a parameter for the spin-orbit interaction. α, β, and γ are parameters for the configuration interaction

Barycenter States	cm^{-1}	Composition of States
$^4I_{15/2}$	0	$-.99\ ^4I_{15/2}$
$^4I_{13/2}$	6469.1	$1.00\ ^4I_{13/2}$
$^4I_{11/2}$	10084	$.91\ ^4I_{11/2} + .38\ ^2H_{11/2}(2)$
$^4I_{9/2}$	12332	$.73\ ^4I_{9/2} + .42\ ^2H_{9/2}(2) - .35\ ^4F_{9/2}$
$^4F_{9/2}$	15300	$-.77\ ^4F_{9/2} - .50\ ^4I_{9/2} - .30\ ^2G_{9/2}(1)$
$^4S_{3/2}$	18673	$.82\ ^4S_{3/2} - .43\ ^2P_{3/2}$
$^2H_{11/2}$	19226	$-.69\ ^2H_{11/2}(2) - .59\ ^4G_{11/2} + .39\ ^4I_{11/2}$
$^4F_{7/2}$	20542	$.96\ ^4F_{7/2}$
$^4F_{5/2}$	22186	$.92\ ^4F_{5/2} - .36\ ^2D_{5/2}(1)$
$^4F_{3/2}$	22567	$.79\ ^4F_{3/2} - .45\ ^2D_{3/2}(1) - .41\ ^4S_{3/2}$
$^2G_{9/2}$	24523	$.50\ ^4F_{9/2} - .43\ ^2G_{9/2}(1) + .41\ ^2H_{9/2}(2) + .39\ ^2G_{9/2}(2) - .35\ ^4I_{9/2}$
$^4G_{11/2}$	26535	$-.79\ ^4G_{11/2} + .50\ ^2H_{11/2}(2) - .32\ ^2H_{11/2}(1)$
$^4G_{9/2}$	27527	$-.89\ ^4G_{9/2} - .38\ ^2H_{9/2}(2)$
$^2K_{15/2}$	27691	$.96\ ^2K_{15/2}$
$^4G_{7/2}$	27987	$.64\ ^4G_{7/2} + .51\ ^2G_{7/2}(1) - .49\ ^2G_{7/2}(2)$

Table 3.2 Energies (in cm^{-1}) and composition of the wavefunctions of spin-orbit multiplets of $4f^{11}$ states in Er^{3+} (barycenters) (Hasan & Richardson, 1982).

Free ion state	Crystal field symmetry	Calculated energy (cm^{-1})[a]	Observed energy (cm^{-1})[b]
$^4I_{15/2}$	$a\Gamma_8$	0	0
	Γ_7	27.1	25
	$b\Gamma_8$	56.6	57
	Γ_6	253.3	259
	$c\Gamma_8$	282.3	288
$^4I_{13/2}$	Γ_6	6492.5	6492
	$a\Gamma_8$	6519.2	6517
	$a\Gamma_7$	6534.2	6532
	$b\Gamma_8$	6671.1	6682
	$b\Gamma_7$	6687.2	6686
$^4I_{11/2}$	Γ_6	10153	10166
	$a\Gamma_8$	10165	10174
	$b\Gamma_8$	10247	10238
	Γ_7	10248	10238
$^4I_{9/2}$	$a\Gamma_8$	12352	12345
	Γ_6	12464	12410
	$b\Gamma_8$	12522	12489
$^4F_{9/2}$	$a\Gamma_8$	15353	15152
	$b\Gamma_8$	15445	15246
	Γ_6	15516	15337
$^4S_{3/2}$	Γ_8	18745	18275

Table 3.3 Calculated and observed energy levels of Er^{3+} $4f^{11}$ states in Cs_2NaYCl_6 [a] (Hasan & Richardson, 1982) [b] (Hasan, et al., 1997)

Free ion state	Crystal field symmetry	Calculated energy (cm^{-1})[a]	Observed energy (cm^{-1})[b]
$^2H_{11/2}$	$a\Gamma_8$	19324	19016
	Γ_7	19338	19049
	$b\Gamma_8$	19386	19140
	Γ_6	19410	19174
$^4F_{7/2}$	Γ_6	20621	20376
	Γ_8	20678	20446
	Γ_7	20688	20467
$^4F_{5/2}$	Γ_8	22293	22056
	Γ_6	22345	22135
$^4F_{3/2}$	Γ_8	22701	22447
$^2G_{9/2}$	$a\Gamma_8$	24557	24428
	Γ_6	24665	24462
	$b\Gamma_8$	24702	24519
$^4G_{11/2}$	$a\Gamma_8$	26532	26110
	Γ_7	26612	26193
	$b\Gamma_8$	26729	26367
	Γ_6	26781	26425

Table 3.3 cont. Calculated and observed energy levels of Er^{3+} $4f^{11}$ states in Cs_2NaYCl_6
[a] (Hasan & Richardson, 1982) [b] (Hasan, et al., 1997)

CHAPTER 4: LASER REFRIGERATION IN $Cs_2NaYCl_6:Er^{3+}$

4.1 Introduction

Optical cooling or refrigeration of solids was proposed by Pringsheim in 1929 (Pringsheim, 1929). It is based on an anti-stokes emission process where the absorption of a photon by a solid is followed by the emission of another photon of higher energy. The extra energy comes from the lattice vibrations or phonons. Anti-stokes emission involves the absorption of lattice vibrations, or phonons in creating a higher energy photon. This annihilates phonons in the solid, thus, reducing its temperature. The energy levels involved in absorption and emission processes are electronic energy levels, typically of an optically active rare earth ion impurity in the solid.

Figure 4.1 gives a simple illustration of the processes involved in laser cooling of a solid by anti-stokes emission. Consider an ideal system with two electronic energy levels. State 0 is the electronic ground state and state 2 is the electronic excited state as depicted in the diagram by the two thicker horizontal black lines. State 1 in the diagram represents the vibrationally excited state associated with the ground electronic state 0 as depicted in the diagram by the narrower horizontal black line. This vibrational level exists at an energy above the ground state and will be populated at room temperature due to the phonons depicted by the dark red dashed arrow. An incident photon of energy E, for example, from a laser, depicted by the bright red dashed arrow, is absorbed by the rare earth ion causing the transition from state 1 to state 2. This transition is represented by the solid red arrow. An upconverted photon of higher energy, E', depicted by the blue

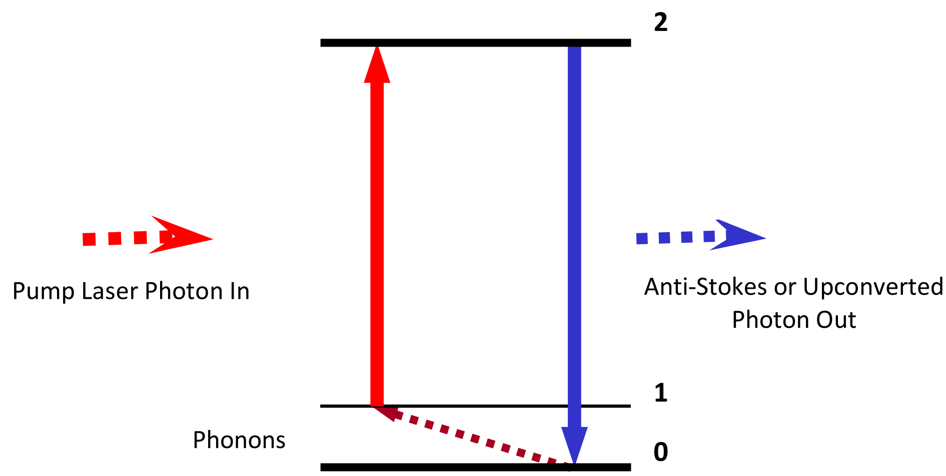

Figure 4.1 Mechanism of Anti-Stokes laser cooling in an ideal solid system. States 0 and 2 are the electronic ground and excited states. State 1 is the vibrationally excited state of the ground state.

dashed arrow, is emitted as the electron returns from state 2 to state 0. This transition is shown by a solid blue arrow. The additional energy is provided by a lattice phonon such that:

$$E' = E + \hbar\omega_{ph} \qquad \text{(Eq. 4.1)}$$

where $\hbar\omega_{ph}$ is the energy of the phonon with a frequency of ω_{ph}. With every cycle of this process a phonon is annihilated resulting in a reduction of phonons in the solid and so, the solid is cooled. It should be noted that the actual energy level structure in a solid is much more complicated than in the simplified diagram and will be addressed in more detail later.

The concept of cooling by anti-stokes emission was contested as a thermodynamic impossibility. It seemed to create a lower temperature of a solid from a higher temperature by irradiating it with light, thus violating the second law of thermodynamics. Optical cooling was accepted as a thermodynamic possibility in 1946 when Landau pointed out that the entropy of the light source should be included in the system. Taking into account that the emitted light has a higher entropy than the pump light, the entropy of the system, as a whole, increases. Thus, no violation of the second law of thermodynamics occurs.

Bulk cooling of a solid that has ~10^{24} atoms per cm^3 requires a powerful light source to achieve sufficient incident photon density to excite a sufficient fraction of atoms for cooling. In principle, a laser could provide such a powerful source. However, lasers were invented in 1960, more than three decades after Pringsheim's prediction. It took another thirty five years after the invention of the laser before laser cooling in solids was first demonstrated by Epstien et. al. (Epstein, Buchwald, Edwards, Gosnell, & Mungan, 1995). This was mainly because of very stringent requirements that are set for the energy level scheme for cooling and different competing heating processes that, generally, dominate in solids. The temperature differences of up to 0.3 K were observed in a ZBLANP host doped with ytterbium, a rare earth lanthanide ion, when irradiated with light at wavelengths between 1008 nm and 1030 nm.

Laser cooling of atoms in gases was accomplished well before laser cooling in the solid state. It should be noted that the first proof of principle was experimentally observed in 1981 when experiments on cooling of CO_2 molecules were reported (Djeu & Whitney, 1981). Therefore, the phrase "laser cooling" is often, understandably, considered to be in reference to atoms or molecules. To be clear, the laser cooling discussed in this dissertation is the bulk cooling of solid state materials.

As stated previously, cooling involves the anti-stokes process which annihilates phonons. The probability that such an anti-stokes process will take place without an accompanying Stokes and other phonon generating processes is very small. Therefore, generally, and almost always, laser irradiation of solids leads to their heating, melting, evaporating, etc. For this reason optical cooling can only take place in certain special circumstances:

- First, the cooling processes should win over the heating processes. If more phonons are created than are annihilated, the temperature of the solid will increase.
- Second, at least some overlap is required between the absorption and emission of the electronic transition to be utilized for the cooling. Figure 4.2 shows such an electronic transition in emission and absorption spectra schematically. If no overlap exists between the two absorption and emission profiles, optical cooling is not possible with the transition in question.
- Third, there should be a minimum of nonradiative energy transfer between the optically active ions. Invariably, in all such processes there is a net phonon generation, thus heating the solid.

Yb^{3+} was the focus of considerable earlier work. This $4f^{13}$ electron ($4f^{1}$ hole) system has one ground and one excited state, ${}^{4}F_{7/2}$ and ${}^{4}F_{5/2}$. Therefore some undesirable energy transfer processes and multi-photon absorptions will not be present.

Epstein's group reported a minimum attainable temperature of 110 ± 5 K in a 5% doped Yb:YLF system (Seletskiy, et al., 2011). Any further lowering of the cooling temperature is limited by the crystal field energy level splittings of the Yb^{3+} ground state. With its $4f^{13}$ electrons, the ground state, ${}^{4}F_{7/2}$, has 2J+1 = 8 fold degeneracy which, in non-cubic systems, results in 4 Kramer's doublets, can split into no more than 4 energy levels. The energy level separation between these states is large. Using such an energy level structure for the ground state, cooling temperatures will be higher. Erbium has the advantage of a crystal field splitting structure with smaller energy gaps and therefore a possible lower attainable cooling temperature.

4.2 Lifetime and Broadening of Transitions

Consider an absorption or emission transition between the purely electronic states of an ion in a crystal. At 0 K, it would appear as a very sharp, narrow peak in a material's absorption/emission spectrum (Figure 4.2 a). This absorption/emission profile is termed as a Zero Phonon Line (ZPL). However, the presence of phonons at room temperature serves to broaden the peak in such an absorption/emission profile (Figure 4.2 b). With the temperature, the peak absorption/emission position may or may not change. However, broadening would be roughly the same in the absorption and emission profiles. All of the cooling experiments presented in this work were conducted at room temperature, i.e., around 300 K. If the temperature broadened peak allows for the absorption at a longer wavelength (lower energy), than the peak emission wavelength, λ_0, cooling by anti-stokes emission would be possible in principle. Generally speaking, heat generating processes win over the heat absorbing process, especially in a solid. Many energy down conversions, radiative and non-radiative energy transfers, etc. can take place which involve the generation of multiple phonons thus heating the solid.

At T = 0 K the natural lifetime of the state gives the broadening of a transition known as lifetime limited broadening, it arises from the uncertainty principle in its energy-time manifestation (De Bartolo, 1968):

a)

b)

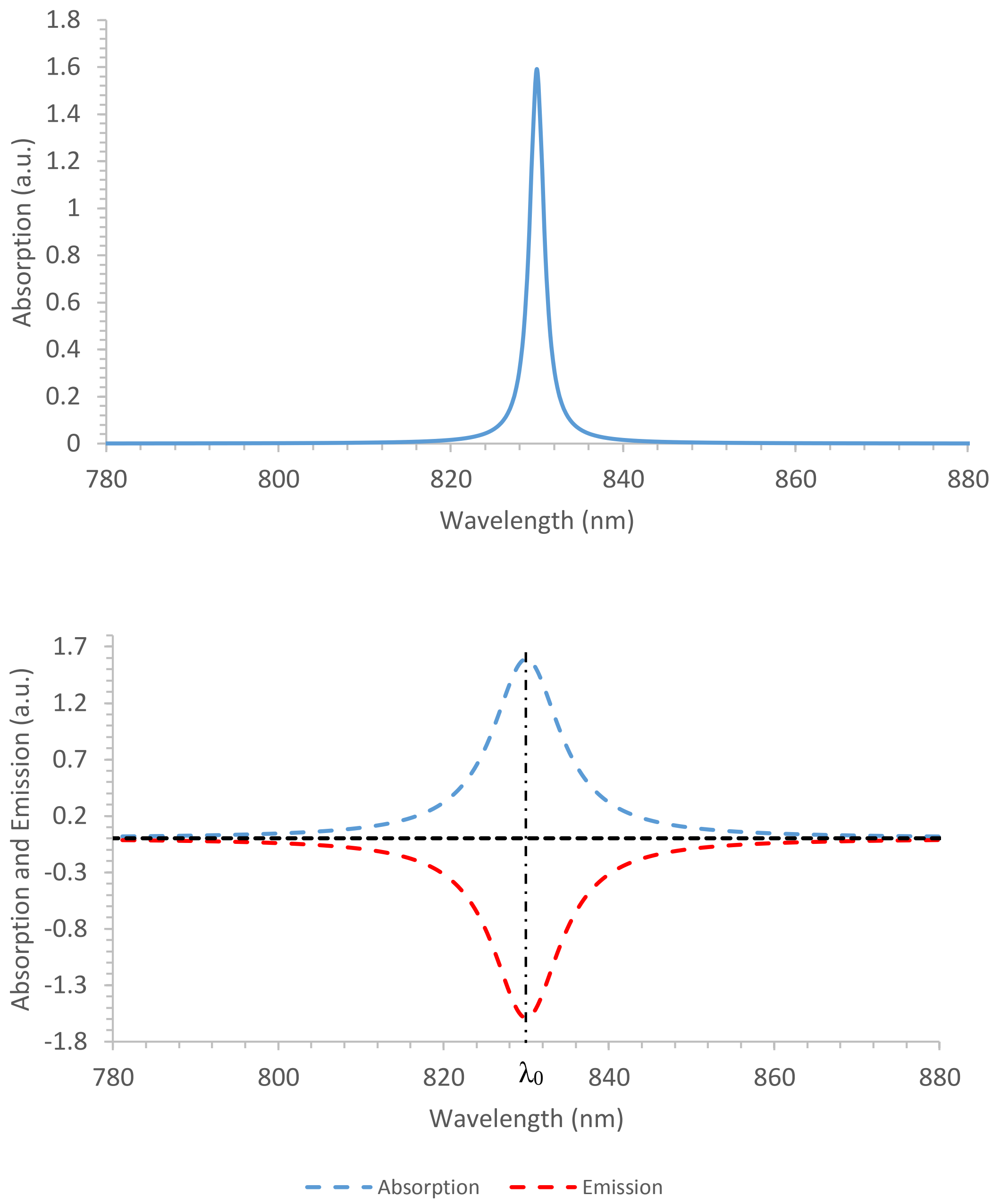

Figure 4.2 a) The purely electronic absorption at low temperature centered at λ_0 = 830 nm
b) Phonon broadened absorption and emission at room temperature centered at λ_0 = 830 nm

$$(\Delta E)\tau = \hbar \qquad \text{(Eq. 4.2)}$$

In $Cs_2NaYCl_6{:}Er^{3+}$ the lifetime limited broadening of the relevant states has an effect of ~10^{-3} cm^{-1} (8.06554 cm^{-1} = 1 meV) .

The longer the lifetime of an electronic excited state, the sharper the transition involving that state. At room temperature, the lifetime of the transition is decreased due to phonon assisted transitions playing a dominant role. This results in the corresponding phonon broadening of the transition, the lifetime of the transition is decreased. Thus, the transition intensity is increased at higher temperature.

Broadening of the linewidth of the absorption/emission profiles, ΔE, caused by the presence of lattice phonons at a nonzero temperature, T, was modelled by Kiel for the d electrons in ruby (Kiel, 1962):

$$\Delta E(T) \cong 10^3 \left(\frac{T}{T_D}\right)^4 \int_0^{\frac{T_D}{T}} \frac{x^3}{e^x - 1} dx \left(cm^{-1}\right) \qquad \text{(Eq. 4.3)}$$

T_D is the Debye temperature of the material and x is $W/(k_B T)$. So, x roughly represents a ratio of the width of the transition to the energy at a given temperature.

Kiel reports that the experimentally observed linewidth in ruby is about 15 cm^{-1} at 300 K. The model presented in equation 4.3 yields a calculated value of about 30 cm^{-1} at the same temperature. This is the case for ruby. However, a quick examination of a transition of $Cs_2NaYCl_6{:}Er^{3+}$ ($^4I_{15/2}$-$^4I_{13/2}$) shows that one of the peaks on the absorption spectrum reveals a width of slightly more than 16 cm^{-1} experimentally (Figure 4.3).

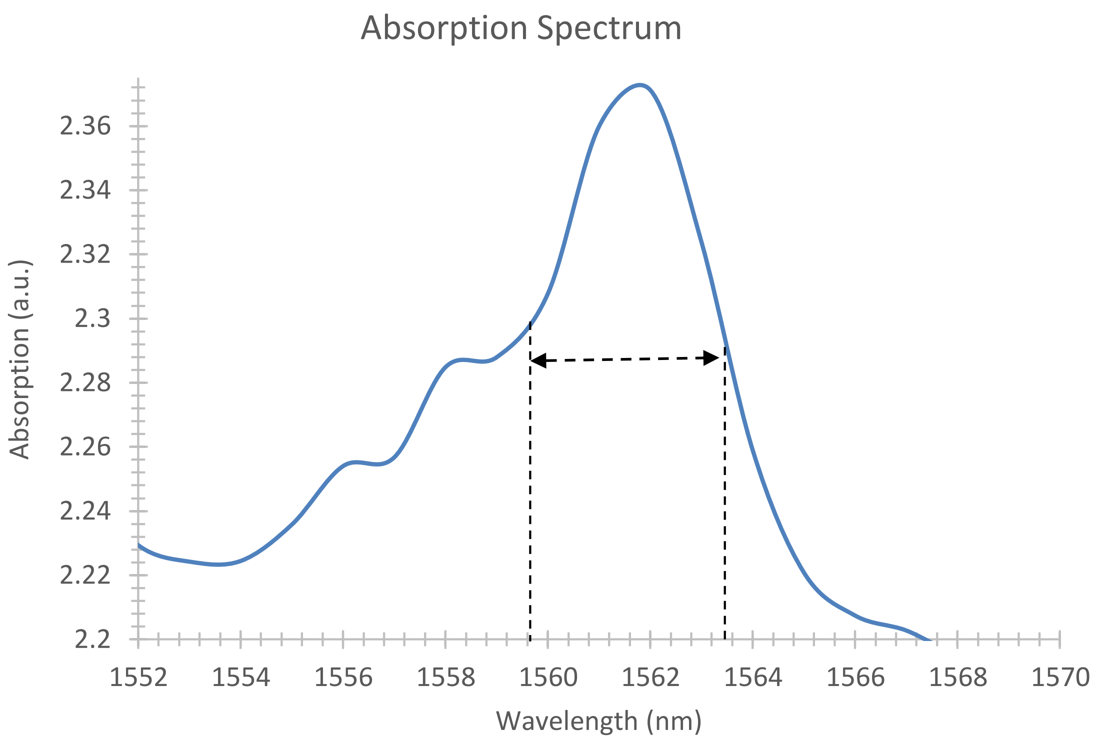

Figure 4.3 The absorption profile of $Cs_2NaYCl_6:Er^{3+}$ at room temperature (300 K) displays a peak relevant to the $^4I_{15/2}$-$^4I_{13/2}$ transition.

Therefore, the two systems display similar linewidth at room temperature, and hence, a comparison is worthwhile and follows.

Using the Debye temperature of NaCl, 321 K, as an approximation for the Debye temperature of $Cs_2NaYCl_6:Er^3$ equation 4.3 yields a result of more than 204 cm^{-1} at room temperature. A number of assumptions were made in the calculation which could account for the difference. The numerical factor of 10^3 is a simplified approximation of terms dependent on the parameters for ruby and its energy levels.

This approximation may not be a good one for $Cs_2NaYCl_6:Er^{3+}$. If the parameters are changed and a different linewidth obtained, the agreement could change considerably.

Additionally, the Debye temperature of NaCl is used as to approximate the Debye temperature of $Cs_2NaYCl_6:Er^{3+}$. A difference in the Debye temperature would influence the result yielded by equation 4.3. For example, increasing the Debye temperature by 20 percent to 385.2 results in a calculated value of slightly less than 156 cm^{-1}.

The similar linewidths of ruby and $Cs_2NaYCl_6:Er^{3+}$ can be explained via the individual characteristics of the materials which make them resistant to greater thermal broadening. In ruby, of the two relevant energy levels, ^4A and ^2E, the former is spherically symmetric and there is no asymmetric crystal field and so is immune to thermal broadening. The latter experiences only a second order effect from the crystal field, minimizing the thermal broadening for that state. This is due to the symmetry of these states.

The broadening in the $^4I_{15/2}$-$^4I_{9/2}$ transition of Cs_2NaYCl_6:Er^{3+} would be similar to the broadening seen in the $^4I_{15/2}$-$^4I_{13/2}$ transition. Data is not as readily available for the $^4I_{15/2}$-$^4I_{9/2}$ transition. It is very weak at room temperature and so, the $^4I_{15/2}$-$^4I_{13/2}$ transition is a useful reference.

The expected linewidth of the transition in ruby is twice the value of the experimental linewidth. The expected linewidth of the transition in Cs_2NaYCl_6:Er^{3+} is more than 10 times the value of the experimental linewidth. The optically active $4f^{11}$ electrons in Cs_2NaYCl_6:Er^{3+} are shielded by the filled outer electron shells from the effects of the crystal field from the rest of the crystal lattice. Taking this shielding into account, the greater disparity between the experimental linewidth and the expected linewidth calculated by the model in equation 4.3 makes sense.

Equation 4.3 includes a factor of T^4 which indicates that the equation should result in a very nonlinear effect based on temperature. However, the $^4I_{15/2}$-$^4I_{9/2}$ transition of Cs_2NaYCl_6:Er^{3+} has properties which makes it equally or more resistant to thermal broadening, at room temperature. At 300 K a temperature difference of 6 K, the greatest reduction obtained in the cooling experiments in our case, will have a very small effect on linewidth.

Phonon broadened absorption and emission spectra have been depicted for illustrative purposes in Figure 4.2 b. The absorption spectrum is represented by the blue dashed curve. The emission spectrum is represented by the red dashed curve. Note that both the absorption and emission spectra are centered at 830 nm, the peak of the emission spectrum of the ZPL at λ_0. We have assumed that both absorption and emission graphs have a width at half maximum of around 5 nm due to the temperature of 300 K. Because of the overlap between the absorption and emission profiles, if one irradiates the sample at, $\lambda_0+\Delta\lambda$, there will be a high probability that a photon will be emitted at a shorter wavelength. This results in the creation of an upconverted photon, sometimes also called anti-stokes emission.

For a cooling process to be efficient, reabsorption of the upconverted photon should be avoided as much as possible as any photons that are recaptured will decrease the effectiveness of the cooling because they will very likely result in phonon generation. Another potential impediment to laser cooling is the presence of non-radiative energy transfer processes, processes that result in the creation of another phonon, or multiple phonons, instead of an upconverted photon. Such processes result in an increase in the thermal energy in the solid and heat the sample instead of cooling it.

4.3 Relevant Calculated Energy Levels for Er^{3+} in Cs_2NaYCl_6

The calculated energy levels which are relevant for the laser refrigeration experiments are the $^4I_{15/2}$, $^4I_{13/2}$, $^4I_{11/2}$, and $^4I_{9/2}$ states. These are the ground state and first three excited states of the optically active $4f^{11}$ electrons in $Cs_2NaYCl_6:Er^{3+}$ and have been displayed in Figure 4.4. The splittings of the states are depicted by horizontal lines in the diagram. The L-S-J states are identified to the left and the observed and calculated energy levels are displayed to the right of each state in units of cm^{-1}. The vertical arrows

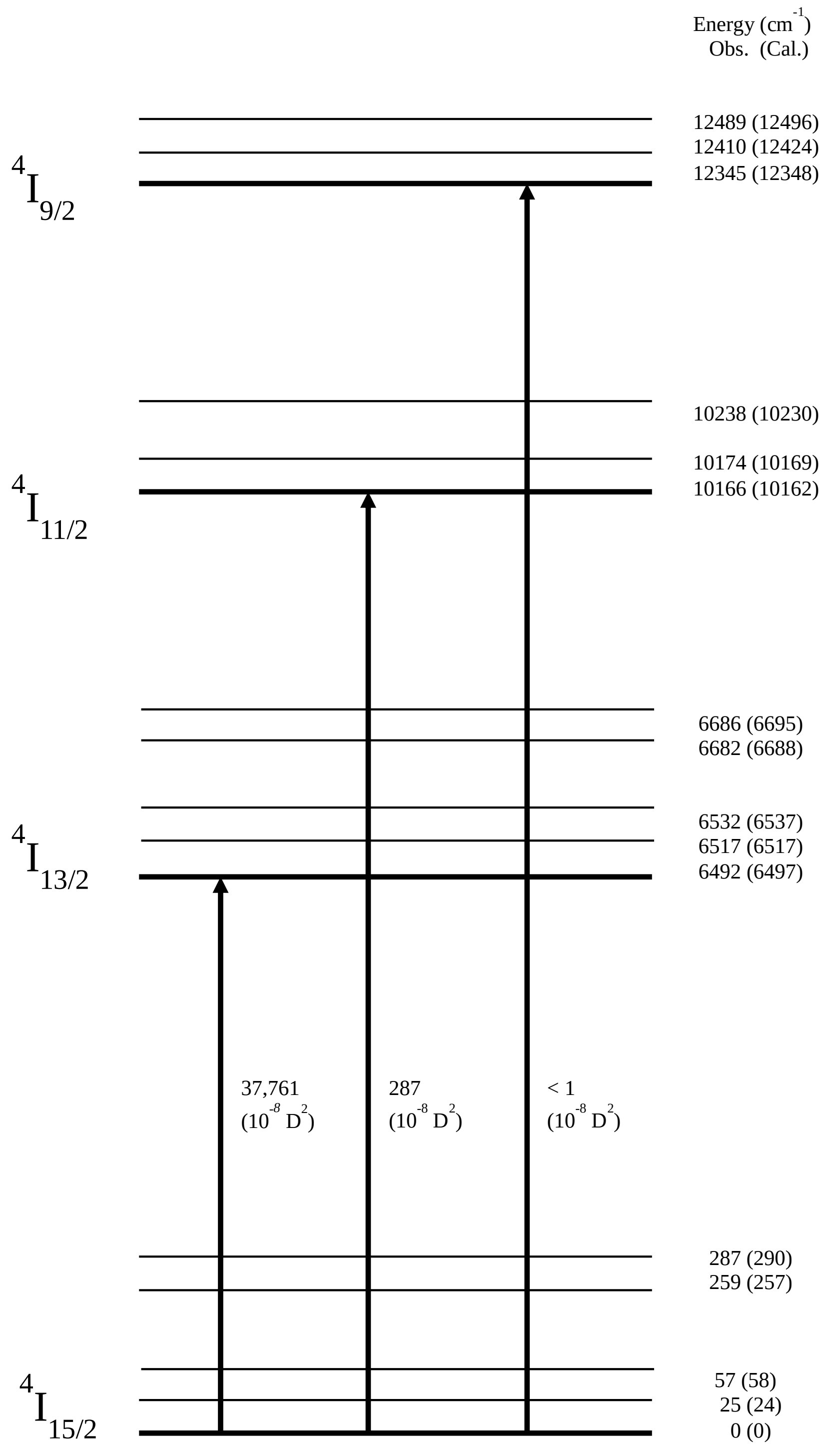

Figure 4.4 The energy levels relevant to laser cooling in Cs_2NaYCl_6:Er and the corresponding transition intensities. $^4I_{15/2}$ is the ground state. $^4I_{13/2}$, $^4I_{11/2}$, and $^4I_{9/2}$ are excited states. Energy levels are displayed on the right in units of cm^{-1}. Transition intensities are expressed in 10^{-8} D^2.

represent transitions between the states and the transition intensities have been included in units of 10^{-8} D^2.

The $^4I_{15/2}$-$^4I_{13/2}$ transition was investigated as a possible mechanism of laser refrigeration in Cs_2NaYCl_6:Er^{3+}. The $^4I_{15/2}$-$^4I_{9/2}$ transition was investigated as a mechanism of cooling and this transition is the focus of this work where significant cooling has been observed. As can be seen, the second excited state, $^4I_{11/2}$, is far from the ground state so as not to be populated by multiple phonon processes at room temperature. Therefore, it will not interfere with the cooling mechanism. This could otherwise lead to undesired or unexpected phonon generating processes during the sample's irradiation.

Examining the difference between the lowest energy crystal field split state of the $^4I_{9/2}$ manifold and the highest energy crystal field state of $^4I_{15/2}$ state calculated energy levels, one calculates an energy level difference of 12069.7 cm^{-1} which corresponds to a wavelength of about 828.5 nm. Examining the difference between the highest crystal field state of the $^4I_{9/2}$ manifold and the highest energy crystal field state of $^4I_{15/2}$ manifold yields an energy difference of 12496 cm^{-1} this corresponds to a wavelength of about 800 nm. Experimental observations along with this calculation together with the observed spectra provide an estimate of the wavelength region best suited for investigation (Hasan & Richardson, 1982) (Hasan, et al., 1997).

Similarly, the crystal field states of relevant to the $^4I_{15/2}$-$^4I_{13/2}$ transition can used to obtain a predictive region of wavelengths for cooling in that transition. Such a calculation yields values of 1611.1 nm and 1493.6 nm.

The resulting calculated energy levels reliably fall within ~10 cm^{-1} of experimental values. The results of the calculations presented here have excellent agreement with experimental observation. The filled outer shells shield the 4f electrons in the cubic $Cs_2NaYCl_6:Er^{3+}$ system from the influence of the rest of the crystal resulting in a very small contribution from the crystal field. Due to this small influence and the symmetry of the crystal field, which allows the crystal field to be represented in terms of only two parameters, the calculations are much more accurate than in other systems.

4.4 Observed Spectra of Er^{3+} in Cs_2NaYCl_6

The absorption spectrum of the previously listed transitions, the $^4I_{15/2}$-$^4I_{13/2}$ transition, the $^4I_{15/2}$-$^4I_{11/2}$ transition, and the $^4I_{15/2}$-$^4I_{9/2}$ transition are displayed in Figure 4.5. The horizontal axis displays the wavelength of the light incident on the sample in nm. The vertical axis displays absorption in absorbance units. The sample, $Cs_2NaYCl_6:Er^{3+}$, is very hygroscopic and therefore an evacuated chamber was necessary to protect the crystal from traces of water in the atmosphere. The spectrum was taken using a Varian Cary 500 dual beam spectrophotometer as previously described in chapter 2 at room temperature.

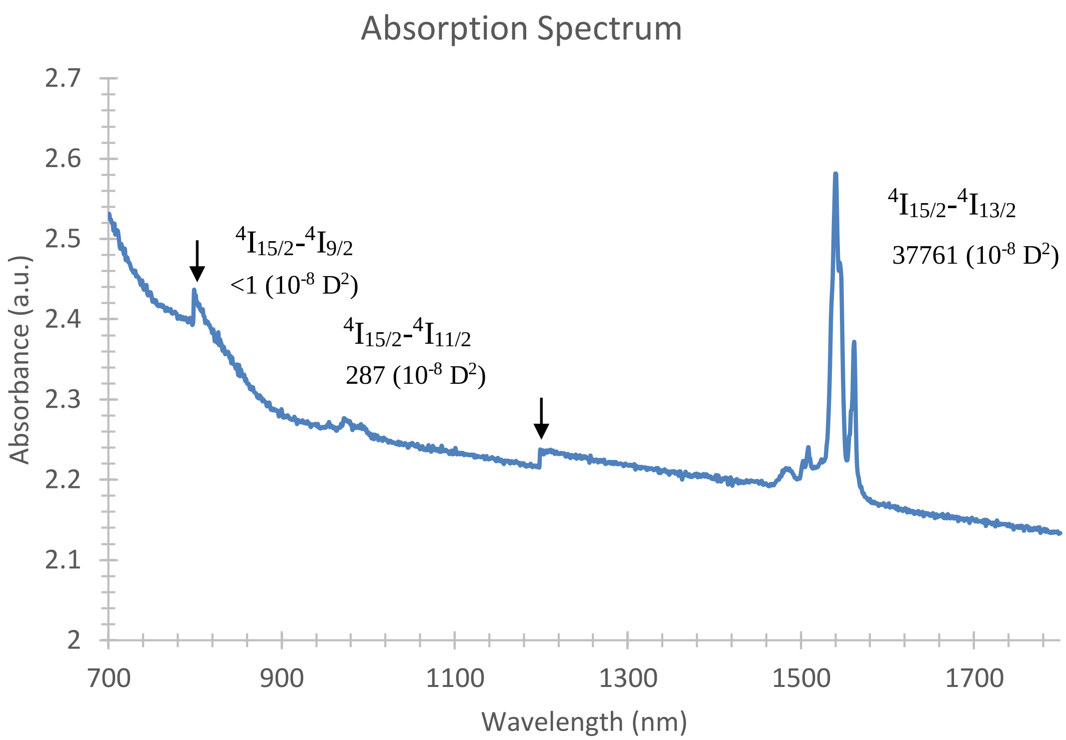

Figure 4.5 Absorption spectrum of Cs_2NaYCl_6:Er^{3+} at room temperature taken with a Varian Cary 500 spectrophotometer. The transitions $^4I_{15/2}$-$^4I_{13/2}$, $^4I_{15/2}$-$^4I_{11/2}$, and $^4I_{15/2}$-$^4I_{9/2}$ are identified on the graph and dipole strength is shown below the state labels in units of 10^{-8} D^2. The abrupt changes appearing in the spectrum caused by the change in optics/detectors are marked by two small arrows.

The strongest absorption features are seen around 1500 nm corresponding to the $^4I_{15/2}$-$^4I_{13/2}$ transition. This transition is particularly strong because it is a magnetic dipole allowed transition, $\Delta J = \pm 1$. The ZPL is strong and isolated and therefore has allowed us to estimate broadening at room temperature due to lattice phonons. Some of the peaks of this transition make it the most favorable transition for attempting laser cooling that will be discussed later. Most of the laser cooling work presented in this dissertation is not on this transition. Chapter 5 will briefly discuss cooling attempts in this transition.

The $^4I_{15/2}$-$^4I_{11/2}$ transition is much weaker than the $^4I_{15/2}$-$^4I_{13/2}$ transition as can be seen by the calculated absorption strength and the observed very weak features on the spectra between 900 nm and 1000 nm. Cooling was not attempted using the $^4I_{15/2}$-$^4I_{11/2}$ transition. The upconversion and energy transfer processes possible from this state prohibited us from attempting cooling in this transition.

The $^4I_{15/2}$-$^4I_{9/2}$ transition is even weaker, less allowed than the $^4I_{15/2}$-$^4I_{11/2}$ transition. This transition strength is 4 orders of magnitude smaller. It is very faint in absorption. However, the ZPL corresponding to this manifold can be identified from low temperature, 10 K, emission spectra (Hasan, et al., 1997). This helps us identify the very faint absorption features corresponding to the $^4I_{15/2}$-$^4I_{9/2}$ transition. This transition was the focus of most of the cooling attempts presented in this dissertation. The two sharp features near 800 nm and 1200 nm are fictitious and caused by changes in the optics of the Varian Cary 500 spectrophotometer as indicated by arrows.

4.5 Experimental Data on Laser Refrigeration

During the laser refrigeration experiments, efforts were taken to isolate the sample from any unnecessary conductive, convective, or radiative sources of heating. The sample was held in a vacuum chamber and its mount was made as small as possible to minimize the sample's thermal contact with other materials. While the sample was irradiated with a laser which was incident on the sample, a shield or iris was used to minimize the amount of scattered light that reached sensitive components of the apparatus. Temperature measurements were taken with two thermocouples. The first thermocouple, TC1, was in direct contact with the sample and measured the sample's temperature while the second thermocouple, TC2, was placed in close proximity to TC1 but was not in contact with the sample. TC2 measured the temperature of the surrounding environment in close proximity to the sample. A description of the experimental design is provided in greater detail in Figure 2.8 in chapter 2.

In order to establish a baseline of the room temperature for the laser refrigeration experiments, initial voltages of the thermocouples TC1 and TC2 were recorded for 30-100 seconds before irradiating the sample with the laser. The data collection before irradiation accounted for any sources of noise in the lab causing variations in the thermocouple voltage measurements. During this time the laser was not incident on the sample nor on any part of the chamber. It was completely blocked by a stopper. Once the initial values were established, the laser was unblocked to irradiate the sample for a predetermined duration of time, 2-120 minutes. During this time, no data relevant to the analysis was collected as the multiple scatterings of the laser beam from the sample, the walls and windows of the chamber would irradiate the thermocouples. Typical power of the incident laser ranged from 1.4 W to 3 W cw around 870 nm and the voltage measurements could easily exceed 2.5 mV during irradiation. This would render any recorded voltages useless for analysis of cooling data. However, monitoring of the voltages of TC1 and TC2 was continued during irradiation because it was useful in determining any accidental changes such as the dislodging of a thermocouple or the sample from their mounts. These mounts are very fragile and are microscopic in size.

After the irradiation was completed, the laser was blocked and the collection of the cooling data started. The collection was continued while the sample returned to room temperature from its initial cooling temperature. This time duration varied from 30 minutes to 120 minutes. Figure 4.6 displays an example of the raw data from one such collection. The graph in Figure 4.6 displays voltage measured by the thermocouple junctions on the vertical axis. The horizontal axis displays time. Due to the nature of the software used to collect the data, each data point on the horizontal axis corresponds to 857 ms (70 data points were collected per minute). TC1 was in direct contact with the sample and its measurements are depicted by a solid blue curve. TC2 was near TC1 and measured the temperature in close proximity to the sample and is depicted by a dashed red curve. The sharp vertical increase beginning with the 53rd data point corresponds to the sample's exposure to the laser. The sharp decrease near 1500 on the horizontal axis corresponds to the laser being blocked.

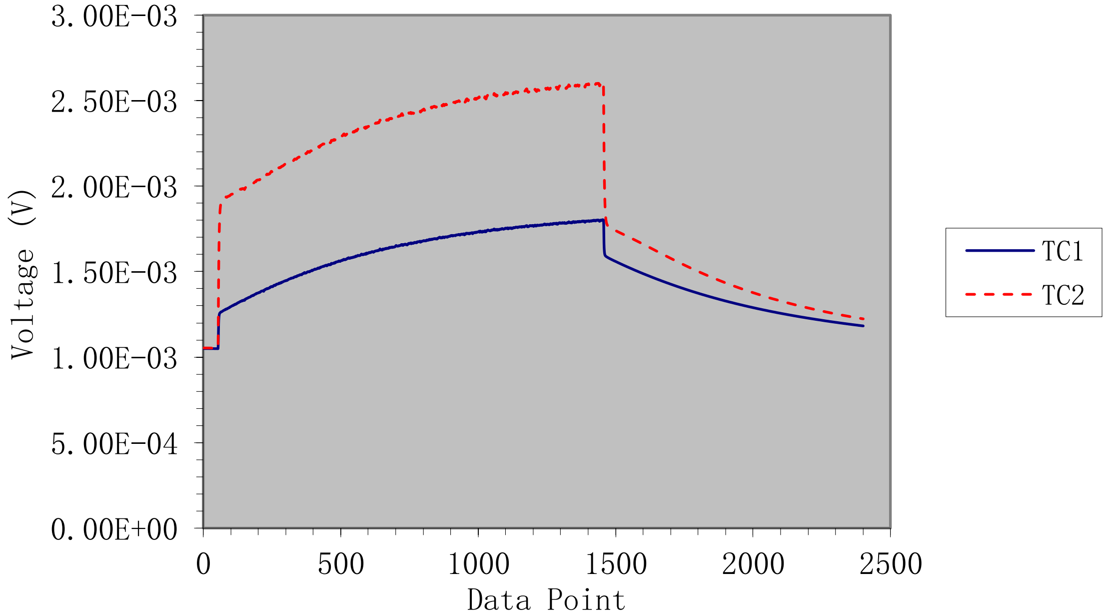

Figure 4.6 The graph above displays the raw data for a laser cooling experiment. The wavelength was set to 870 nm. The power incident on the sample was cw 2.21 W. The sample was irradiated for 20 minutes. The vertical axis displays the thermocouple readings in volts. The horizontal axis displays time (70 data points/minute).

A relative temperature measurement can be obtained by taking the difference between the voltages measured by TC1 and TC2. The graph in Figure 4.7 displays the relative voltage on the vertical axis. The horizontal axis displays time. A positive value on the vertical axis indicates that the sample is hotter than its surroundings while a negative value indicates that the sample is cooler in comparison.

Thermocouple voltages are specific to the load in the circuit. Therefore, initial difference in two thermocouple voltages at room temperature were recorded and this initial difference can be subtracted from all data points to take into account the slight difference in design of the two circuits of the thermocouples. The initial difference was subtracted from all data points. The graph in Figure 4.8 displays the difference in the voltages measured by the thermocouple junctions on the vertical axis adjusted so that the value on the vertical axis for the first data point is 0. The horizontal axis displays time. As usual, a positive value on the vertical axis indicates that the sample is hotter than its surroundings while a negative value indicates that the sample is cooler in comparison.

4.6 Experimental Verification of Cooling

4.6.1 Introduction

An investigation of the wavelength dependence of laser cooling in solids serves several purposes (Condon, Bowman, O'Conner, Quimby, & Mungan, 2009)

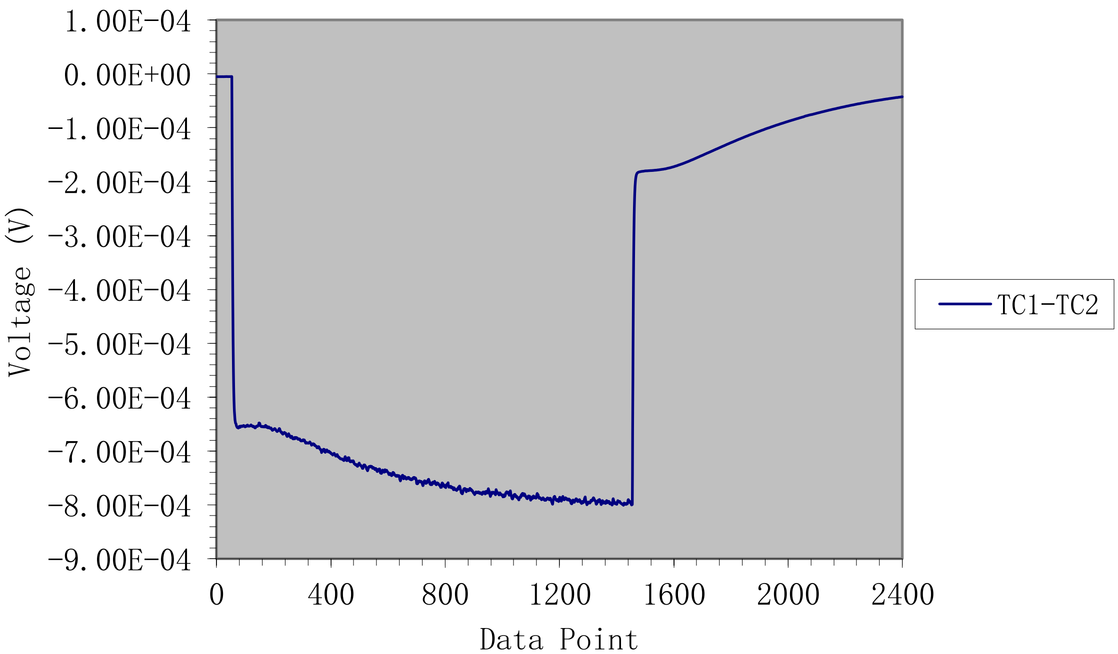

Figure 4.7 The graph above displays TC1-TC2 for a laser cooling experiment. The wavelength was set to 870 nm. The power incident on the sample was cw 2.21 W. The sample was irradiated for 20 minutes. The vertical axis displays the thermocouple measurements in volts. The horizontal axis displays time (70 data points/minute).

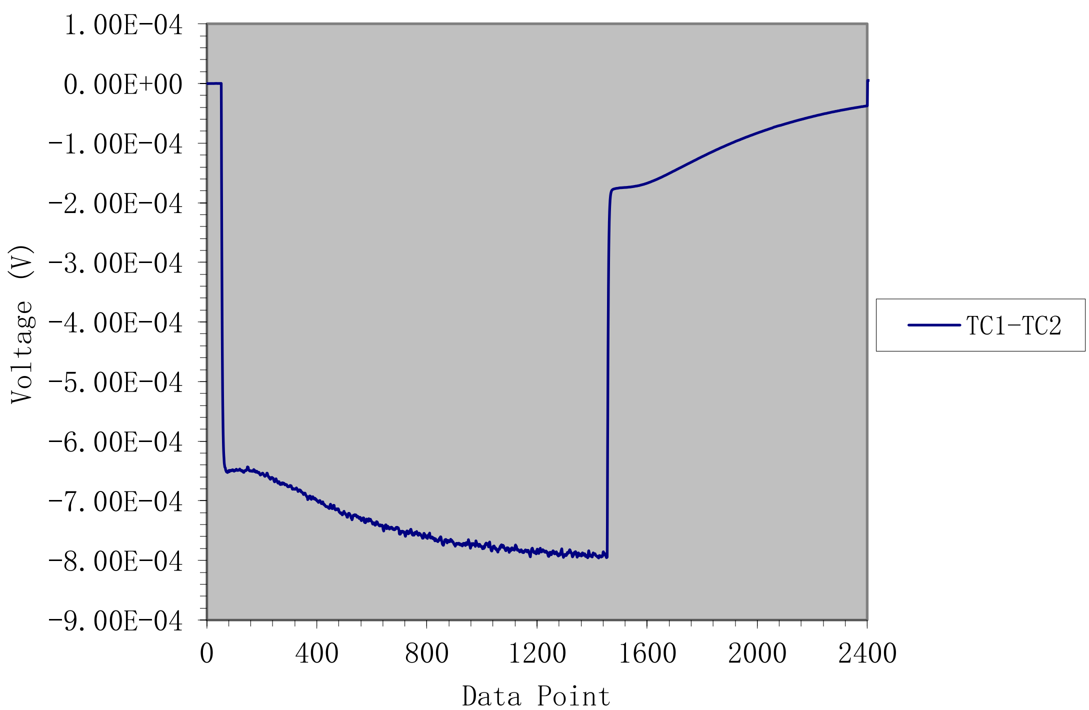

Figure 4.8 The graph above displays TC1-TC2 for a laser cooling experiment adjusted for the initial difference between TC1 and TC2. The wavelength was set to 870 nm. The power incident on the sample was cw 2.21 W. The sample was irradiated for 20 minutes. The vertical axis displays the thermocouple readings in volts. The horizontal axis displays time (70 data points/minute).

(Epstein, Buchwald, Edwards, Gosnell, & Mungan, 1995) (Fernández, García-Adeva, & Balda, 2006) (Fernández, García-Adeva, & Balda, Anti-Stokes laser-induced cooling in rare-earth doped low phonon materials, 2012). It identifies the wavelength which provides the best and most efficient cooling results. A wavelength dependence investigation helps to mitigate potentially misleading data that could come from several sources. Finally, any further complications by nonlinear energy transfer and upconversion processes are also highly dependent on the energy (wavelength) of the incident radiation.

In this section, results are presented on different wavelengths of the laser light. The cooling experiments were performed at different wavelengths of the irradiating laser light.

4.6.2 Cooling and Heating Results

Depending on the wavelength, a crystal may show cooling or heating or no change in temperature when the heating and cooling processes balance out. The following experimental data represents a comparison of the cooling and heating experiments. Figure 4.9 shows the results of two experiments.

During the first experiment, the crystal was irradiated with light at a λ_{irr} = 871 nm. The power output from the Ti-Sapph. laser was 1.6 watts in both cases. With the window's coefficient of transmission, 0.92, this resulted in 1.47 watts incident on the crystal. The crystal was irradiated for 8 minutes before the laser was shut off for

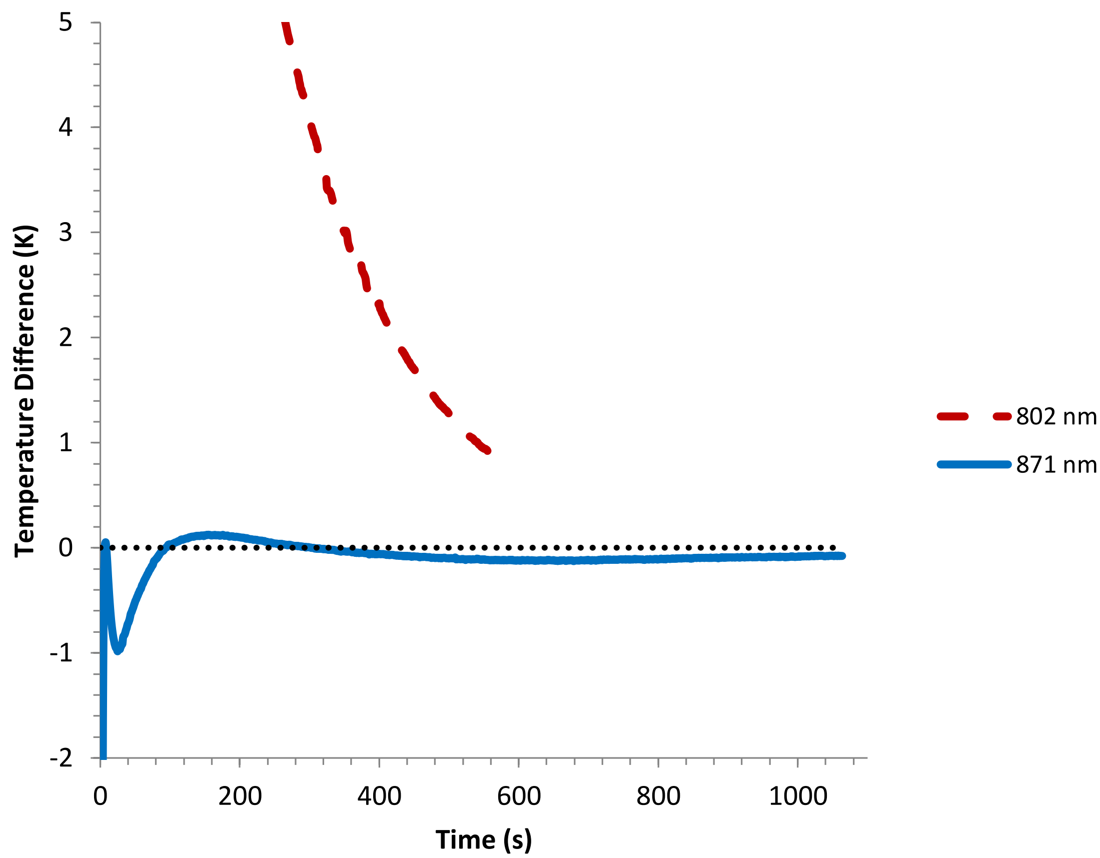

Figure 4.9 Cooling and heating results are presented for comparison. 871 nm is a larger wavelength than the peak wavelength of the $^4I_{15/2}$-$^4I_{9/2}$ transition. 802 nm is a smaller wavelength than the peak wavelength of the transition. Time t = 0 is set to correspond to the shutoff of the laser

λ_{irr} = 871 nm and 7 min for λ_{irr} = 802 nm. At this wavelength excessive absorption by the crystal and scattered light heat the chamber unnecessarily. During this irradiation, the voltage reading from TC2 reached a value of ~3.43 mV. This reading indicates TC2 reached a temperature of about 361 K. At that temperature, the sensor and the electronics were near saturating. We confirmed that the sensor and electronics were not saturating due to excessive heating by irradiation at 802 nm with shorter times of irradiation.

The vertical axis in Figure 4.9 displays the temperature difference that corresponds to the voltage readings (39 microvolts corresponds to $\Delta T = 1$ Kelvin). The horizontal axis displays time measured in seconds and has been set so that 0 corresponds to the shutoff of the laser. The data from the λ_{irr} = 802 nm collection, which provided the heating result, is represented by a dashed red curve. The data from the λ_{irr} = 871 nm collection, which provided the cooling result, is represented by a solid blue curve. A positive value on the vertical axis indicates that the sample is hotter than its surroundings. A negative value on the vertical axis indicates that the sample is cooler than its surroundings. A faint black dotted indicates a temperature difference of 0 K.

4.6.3 Wavelength Dependence

For the data collections on wavelength dependence, the λ_{irr} was the only parameter that was changed, whenever possible. The laser power was held constant throughout the wavelength dependence investigation. The sample was irradiated with a power of 1.47 W as in the experiments described above. Irradiating the sample at a wavelength close to the ZPL generally results in heating whereas irradiating the sample at a wavelength on the lower energy side of the absorption profile provides for a better chance of cooling. However, the first step in the cooling process is the absorption of radiation and therefore absorption is required for cooling to take place. Greater absorption results in greater emission, which is incoherent and scattered in all directions. Therefore, the closer the λ_{irr} is to λ_0, the hotter the surrounding temperature will become because of the scattered radiation. Thus, the duration of the irradiation was limited by the excessive temperature increase inside of the chamber.

During the experiment, if TC2 reached ~3 mV, indicating that the surroundings in the immediate vicinity of the crystal had reached a temperature of ~350 K, the irradiation was stopped. In the cases that TC2 did not reach ~3 mV the irradiation was stopped after 7 minutes. All of the data collections included in the wavelength dependence investigation were conducted using the same sample, a large crystal with a cross sectional area of ~18 mm^2 facing the laser and a volume of ~180 mm^3. It has an 80 percent concentration of erbium by formula.

For analysis and comparison, the data from all of the collections in the wavelength dependence tests is displayed on the single graph in Figure 4.10. Each λ_{irr} is represented by a different color as indicated by the legend to the right of the graph. The horizontal axis displays time in seconds and the vertical axis displays the temperature difference that corresponds to the voltage readings. The data was selected so that the shutoff of the laser corresponds to time = 0 seconds on the horizontal axis. A positive value on the vertical axis indicates that the sample was hotter than its surroundings. A

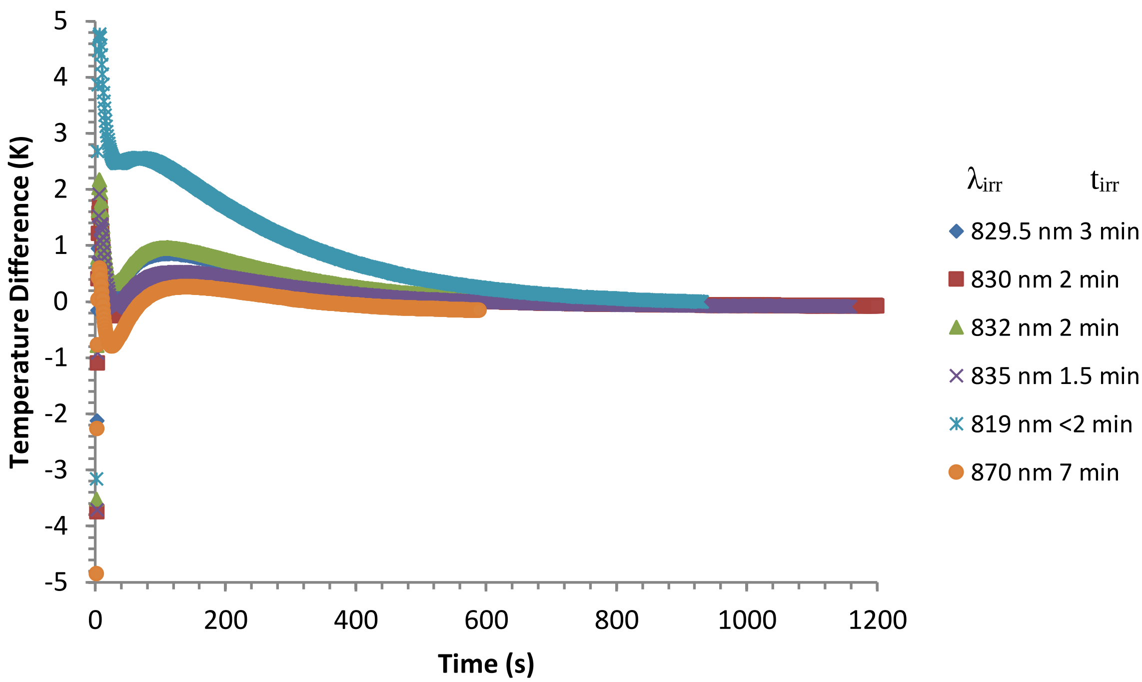

Figure 4.10 Wavelength, λ_{irr}, dependence results are presented for comparison. All irradiations in this investigation were conducted with a power of 1.47 W incident on the sample and lasted for t_{irr}=7 min or until TC2 reached a reading of ~3 mV. Time, t = 0 is set to correspond to the shutoff of the laser.

negative value on the vertical axis indicates that the sample was cooler than its surroundings. As can be seen, λ_{irr} = 870 proved to be the best cooling wavelength. ~6 K as will be explained in detail in a later section.

4.7 Power Dependence

A power dependence investigation was necessary to determine the power incident on the sample, P_{irr}, which would provide the best refrigeration results. Competition between cooling and heating processes determine the most effective value of P_{irr}. These processes could be internal to the atomic system, arriving from the energy level structure and different phonon baths. On the other hand, the external heating processes could depend on the size of the sample and the geometry of the experiment (the size of the chamber, for example). Scattering of the laser light is one such source of external heating processes. Below a minimum power, cooling generally should not overtake the heating processes. For a critical power level above P_{irr} once again, the heating processes gain enough strength to diminish the observable cooling. This is mainly because of the heating of the surrounding and the thermal coupling of the crystal to it.

At a fixed wavelength of λ_{irr} = 870 nm that provides the best refrigeration of the attempted wavelengths, this set of experiments was designed to determine which incident laser power might provide the best refrigeration results. All of the other parameters, t_{irr} and λ_{irr}, the crystal and the geometry of the experiment were identical for the entire set of experiments. Just as in the wavelength dependence, the crystal had an 80 percent concentration of erbium by formula and a cross sectional area of ~18 mm^2. For each data collection an irradiation time of 8 minutes was used. The vacuum system maintained a pressure inside the chamber of 1.2 x 10^{-5} torr. P_{irr} was varied from one data collection to the next, ranging from 1.84 W to 2.76 W.

The data collected at different powers is displayed for comparison on the single graph by different colors in Figure 4.11. The legend for different colors corresponding to different powers is shown to the right of the graph. The legend identifies the data by P_{irr}, not the power output of the laser. The horizontal axis displays time in seconds. The vertical axis displays the temperature difference as monitored from the thermocouple junction voltage difference for the crystal, TC1, and its surrounding, TC2. As in all cases, the data collection started 30-100 seconds before the crystal was exposed to the laser to account for the dark noise of the system. The data represented here was selected so that the shutoff time of the laser, after the irradiation was completed, corresponds to time t = 0 seconds on the horizontal axis. A positive value on the vertical axis indicates that the sample was hotter than its surroundings. A negative value on the vertical axis indicates that the sample was cooler than its surroundings. It is evident from the comparison that P_{irr} = 2.21 W (2.4 W incident on the chamber) provided the best cooling of the crystal.

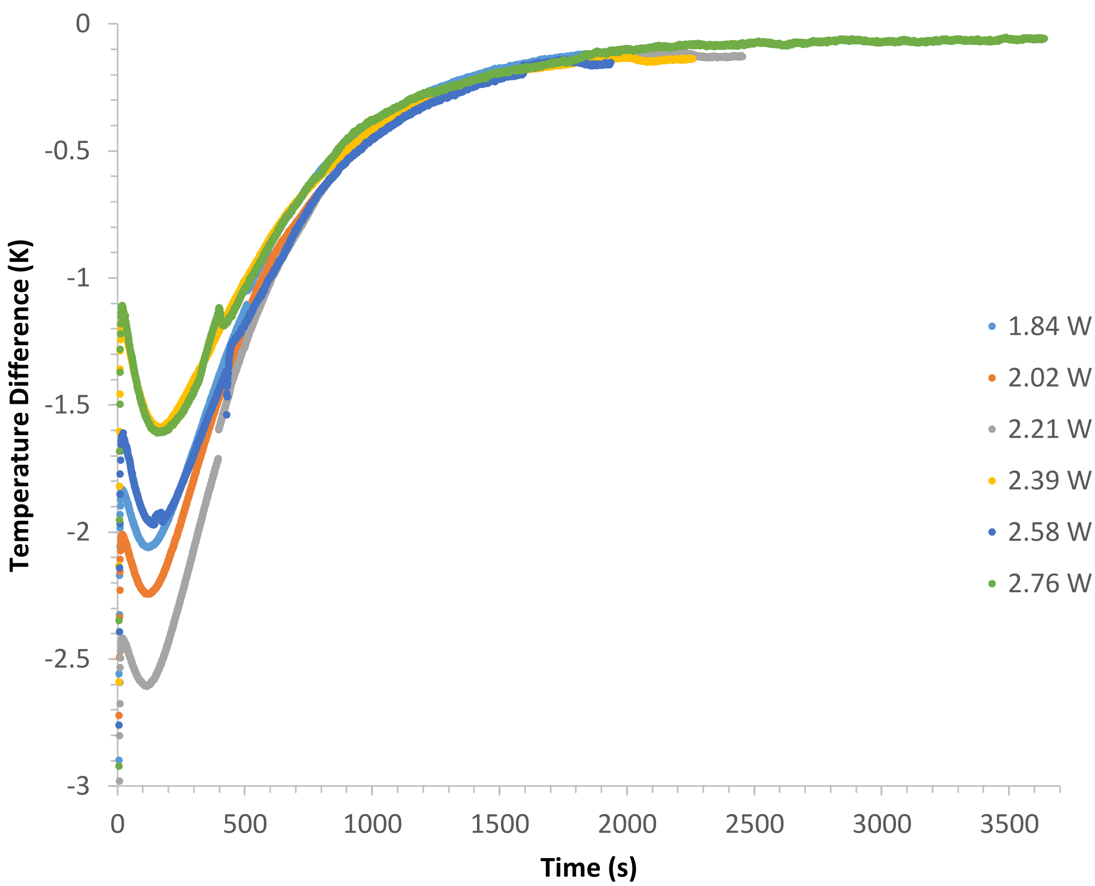

Figure 4.11 Power dependence results are presented for comparison. Each irradiation lasted 8 minutes and the wavelength was set to 870 nm. Time t = 0 is set to correspond to the shutoff time of the laser after the irradiation was completed.

4.8 Time Dependence

A time dependence investigation was necessary to determine which time duration of the irradiation of the sample, t_{irr}, provided the most effective cooling of the sample. Several factors influence the outcome of such time dependence investigations. The size and specific heat of the crystal determine how quickly heat is transferred through the crystal. The temperature baths of the system influence the temperature of the environment surrounding the crystal. The energy differences of the involved transition and the competing phonon generating processes also hold significant influence over the outcome of such time dependence investigations.

Throughout this investigation the only parameter which was varied was the time duration, t_{irr}, for the laser irradiation of the sample. The wavelength of the Ti-Sapph. laser was held constant and set to λ_{irr} = 870 nm, where the most efficient cooling was observed, for the entire set of experiments. The power incident on the sample, P_{irr}, was also held constant. For a pre-determined time duration, t_{irr}, the sample was irradiated with 2.21 W (2.4 W output from the laser). As stated in the previous sections, the sample remained the same for the entire set of experiments, a large crystal with an 80 percent concentration of erbium by formula and a cross sectional area of ~18 mm^2.

For comparison, the data from all of the collections in the power dependence investigation is displayed on the single graph in Figure 4.12. The data from each collection is represented by a marker of a different color as indicated by the legend to the right of the graph. The horizontal axis displays time in seconds. The vertical axis displays the temperature difference derived from the corresponding voltage

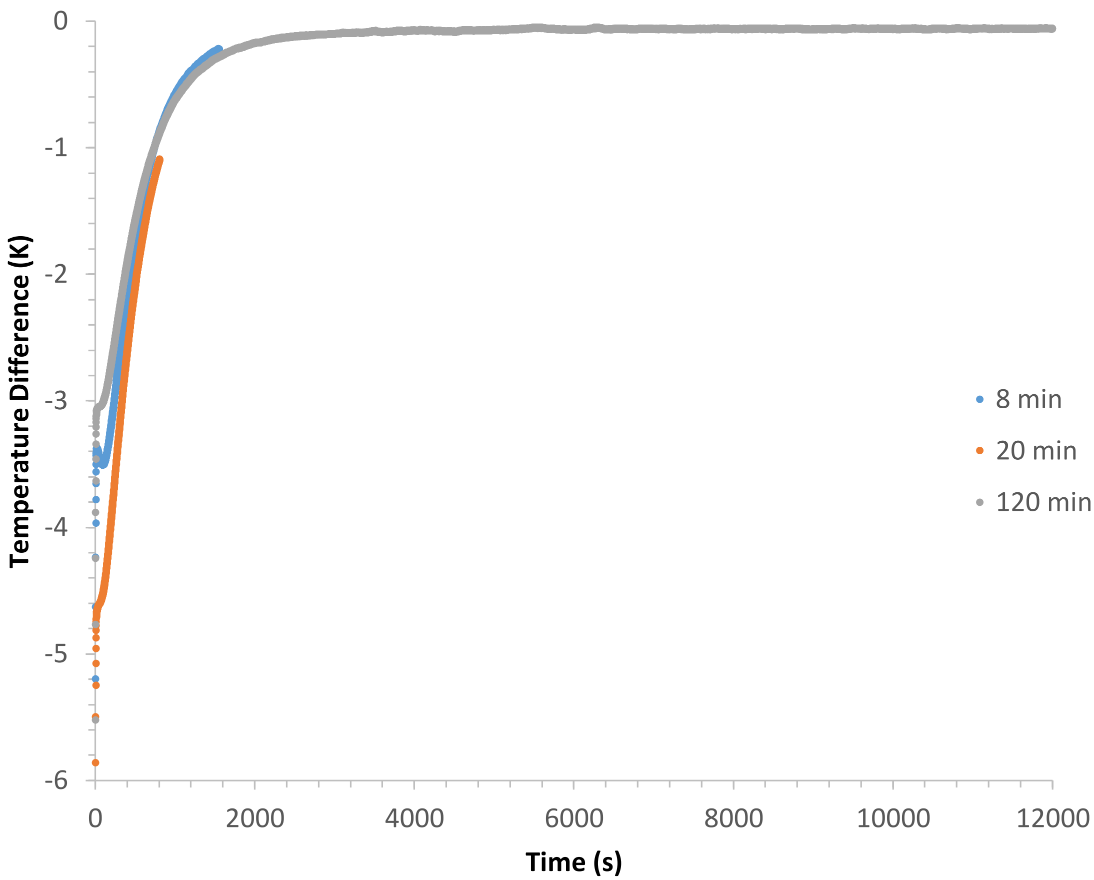

Figure 4.12 Time dependence results are presented for comparison. During each irradiation, the wavelength was set to λ_{irr} = 870 nm and the power incident on the crystal was set to 2.21 W. Time t = 0 is set to correspond to the shutoff of the laser.

measurements from the thermocouple junctions, TC1 and TC2. The data was selected so that the shutoff of the laser corresponds to time t = 0 seconds on the horizontal axis. A positive value on the vertical axis indicates that the sample was hotter than its surroundings. A negative value on the vertical axis indicates that the sample was cooler than its surroundings. As can be seen from the data represented in Figure 4.12, the irradiation lasting 20 minutes provided the best refrigeration results under the current geometry of the experiment.

4.9 Data Analysis

Additional analysis was performed on selected data to further understand the behavior of the sample during the cooling experiments. The purpose of the analysis was to obtain the lowest temperature differential reached by the thermocouples, TC1 and TC2, during the experiment. A trend was fitted to the data and examined at t = 0 s, when the laser was turned off. However, the fit could not be applied to short term behavior of the data as described below.

Some heating processes take place on such a small time scale that we could not be sure that the competition between heating and cooling processes was well captured by the sensors. The thermocouples behaved differently depending on whether or not the junction was in contact with sample. Though the thermocouples utilized in the cooling experiments were very small, 25.4 microns in diameter, as described in more detail in chapter 2, the epoxy used to adhere them to the sample still had a thermal load. The thermal load (epoxy) was kept as small as possible but the temperature changes could not be registered instantly because the epoxy has a high specific heat and low thermal conductivity. Additionally, radiative heating of the entire chamber varied from experiment to experiment. Therefore, recording any change in temperature still involved a slight delay.

The software collected readings from each thermocouple channel once every 857 ms. This was not fast enough to respond to the short term behavior of the sample, less than one second after the shutoff of the laser. Therefore, due to limitations in the software involved, the early data, shortly after the shutoff of the laser, is less than representative of the behavior of the sample. This, however, does not affect the conclusions from the data. It can be interpolated to shorter times approaching t = 0 s to extract the minimum temperature.

The amount of epoxy used to secure the sample and the thermocouple junctions was as small as possible. However the amount varied from experiment to experiment. Radiative heating from the surrounding environment also varied from experiment to experiment. For these reasons, in addition to the software limitations mentioned above, long term behavior was more representative of the sample's behavior than short term changes. Therefore, to extract the minimum temperature from the data, an exponential fit was applied to the long term data and interpolated back to t = 0 s.

Only the set of data that produced the best refrigeration results is presented here. Similar analysis can be done on any other data but analyzing this data also provides the lowest obtained temperature reached in our cooling experiments. The values of the wavelength, incident power, and time duration of irradiation were those that provided the best cooling of the crystal in the wavelength dependence, power dependence, and time dependence investigations described earlier in sections 4.6 through 4.8: λ_{irr} = 870 nm, P_{irr} of 2.21 W, and t_{irr} = 20 minutes.

Figure 4.13 represents only one set of data, the best cooling results already displayed in Figure 4.12. The horizontal axis displays time in seconds. The vertical axis displays the temperature difference which corresponds to the measured voltage difference between TC1 and TC2. The shutoff of the laser corresponds to time t = 0 s on the horizontal axis. It is evident from the data that the long term behavior is exponential. Several different exponential fits were tried, varying parameters to obtain the best long term behavior of the graph presented. The fit was obtained using Microsoft Excel software. The best fit follows the exponential behavior of temperature with time:

$$T = T_{\min} e^{\frac{-t}{B}} + C \qquad \text{(Eq. 4.4)}$$

Where T_{min} is the minimum temperature, B is the time constant, and C is a constant dependent on the initial difference between the voltages measured by TC1 and TC2. The parameter values which provided the best fit to the data are:

$$\mathrm{T} = -6.210 e^{\frac{-t}{459.733}} + 0.124 \qquad \text{(Eq. 4.5)}$$

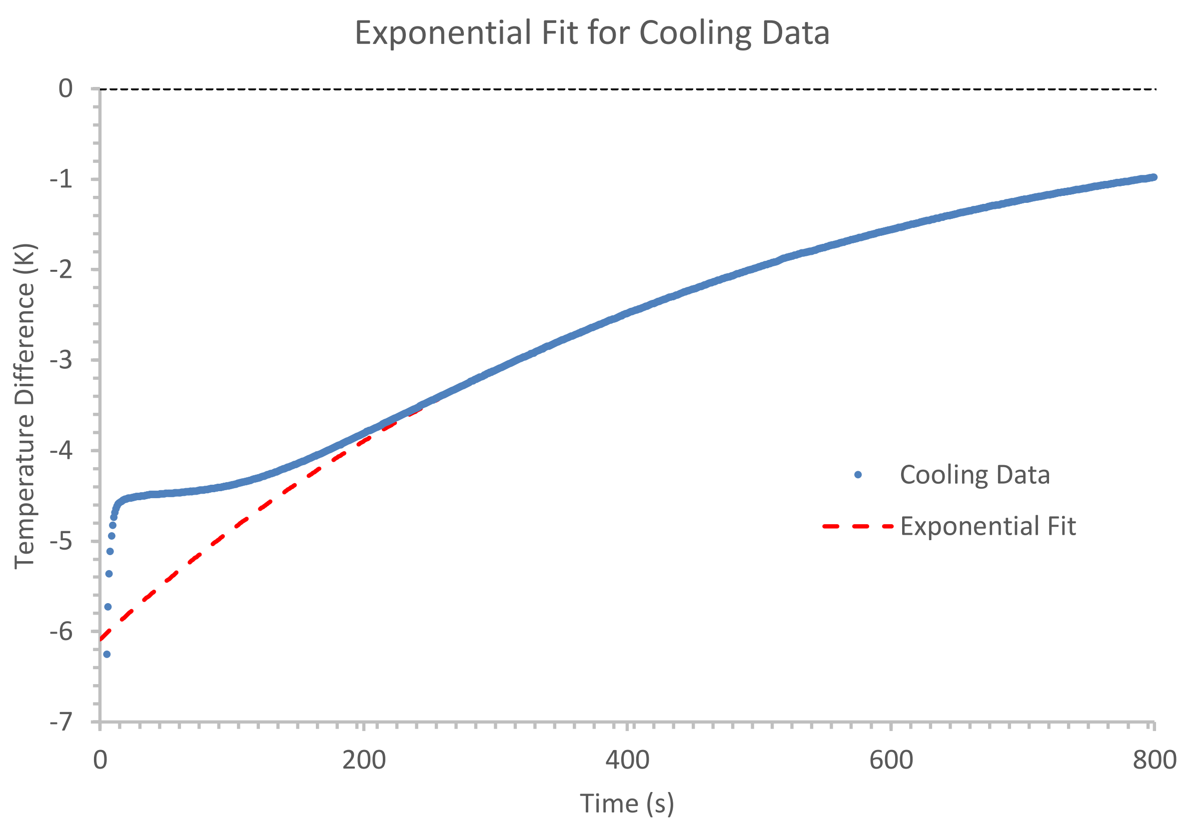

Figure 4.13 Data displaying the best obtained cooling result, the red curve represents the exponential fit and time t = 0 corresponds to the shutoff of the laser. The best fit was obtained with the parameters: $T= -6.210e^{-t/459.733}+0.124$

The parameters in Equation 4.5 are dependent on the geometry of the experiment and properties of the thermocouple sensors. In order to determine the minimum temperature achieved, this fit was then interpolated back to t = 0 s. The value of T at t = 0 s provides the lowest achieved temperature. The data is represented by blue markers and the fit is depicted by a red curve as indicated by the legend to the right of the graph. With this interpolation of the exponential, the best result that was obtained was a temperature difference of ~6.2 K as shown. Figure 4.14 extends the exponential fit to 1800 s as it approaches a temperature difference of 0 K.

The short term data is worth discussing to address its differences from the long term data. The cusp which is visible on the graph near t = 25 s can be attributed to the behavior of several things such as the materials used to manufacture the thermocouple junction, the epoxy, the size and shape of the chamber, the mounts, etc. This is a feature of the graph that is attributed to the experimental apparatus. Since our concern is with the behavior of the sample, which can be extracted utilizing the long term data, the short term data does not prevent that.

4.10 Experiments in KPb_2CL_5

Groups studying laser refrigeration of KPb_2Cl_5 doped with erbium have disagreed regarding reported refrigeration in this host crystal. In 2009, Bowman et. al. addressed methods of detection for experiments using KPb_2Cl_5 in a paper published in *Optics*

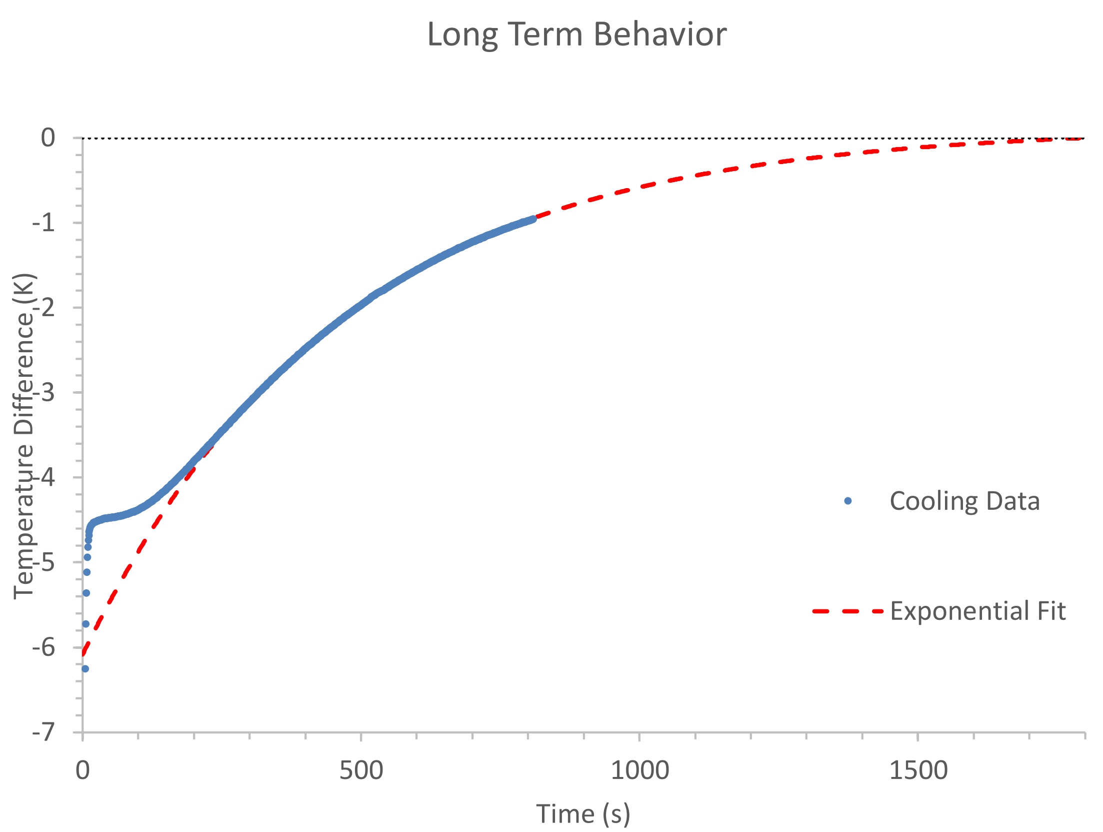

Figure 4.14 Data displaying the best obtained cooling result, the red curve represents the exponential fit and time t = 0 corresponds to the shutoff of the laser. The best fit was obtained with the parameters: $T = -6.210e^{-t/459.733}+0.124$. The fit has been extended to t = 1800 s to show the fit as it approaches a temperature difference approaches 0 K.

Express (Condon, Bowman, O'Conner, Quimby, & Mungan, 2009). The paper asserts that observation with a thermal camera is inappropriate for this crystal because it is transparent to most of the mid-infrared region and so, it is not detectable by such cameras. The paper further asserts that photothermal deflection is problematic because excited state population changes can change the index of refraction of the sample and lead false cooling indications. In 2011, Fernandez et. al. reported laser refrigeration in KPb_2Cl_5 doped with erbium. The method of detection that their group used was a thermal sensitive camera (Fernández, García-Adeva, & Balda, Anti-Stokes laser-induced cooling in rare-earth doped low phonon materials, 2012).

Initial cooling experiments were performed with a pentachloride crystal. The host crystal, KPb_2Cl_5 was doped with ~1% erbium. As in the experiments with Cs_2NaYCL_6:Er, the crystal was mounted in the vacuum chamber with TC1 in direct contact with the crystal to measure its temperature and TC2 in close proximity to the sample to measure the temperature of the surroundings.

During these experiments, there was no liquid nitrogen in the trap of the diffusion pump. So, the vacuum that the pump maintained in the chamber was ~10^{-4} torr.

The sample was irradiated in four separate data collections. Each collection utilized a different wavelength. The wavelengths investigated were 870 nm, 865 nm, 832 nm, and 802 nm.

The first experiment performed with the pentachloride crystal involved irradiation at a wavelength of 870 nm. The Ti-Sapph. laser gave an output power of 1.6 watts. This resulted in an incident power of 1.47 W on the crystal. The irradiation lasted for 7 minutes.

As with the graphs displaying the data for previously presented results. The vertical axis has been adjusted to display the temperature difference which corresponds to the measured voltage difference. The horizontal axis has been adjusted to display time and set so that the time equal to zero corresponds to the shutoff of the laser. A graph displaying the analyzed data has been included in Figure 4.15.

This graph portrays a heating result. There is no discernible evidence of cooling from this data.

The second experiment performed with this crystal involved irradiation at a wavelength of 865 nm. The Ti-Sapph. laser gave an output power of 2.25 watts, resulting in an incident power of 2.07 W on the crystal. A graph displaying the analyzed data for this collection has been included in Figure 4.16.

Like the first pentachloride experiment, this experiment gave a heating result. There is no discernible evidence of cooling from this data.

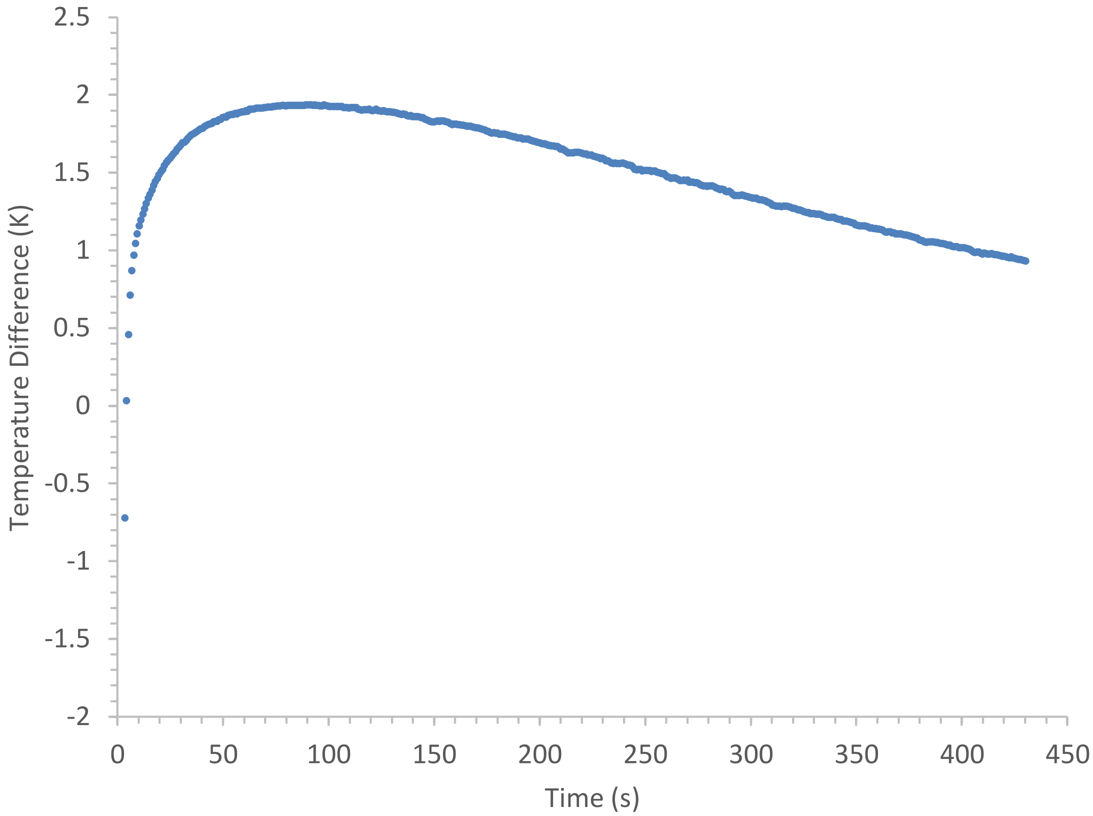

Figure 4.15 TC1-TC2 for pentachloride crystal 3 minute irradiation at 870 nm, 1.47W incident on the crystal

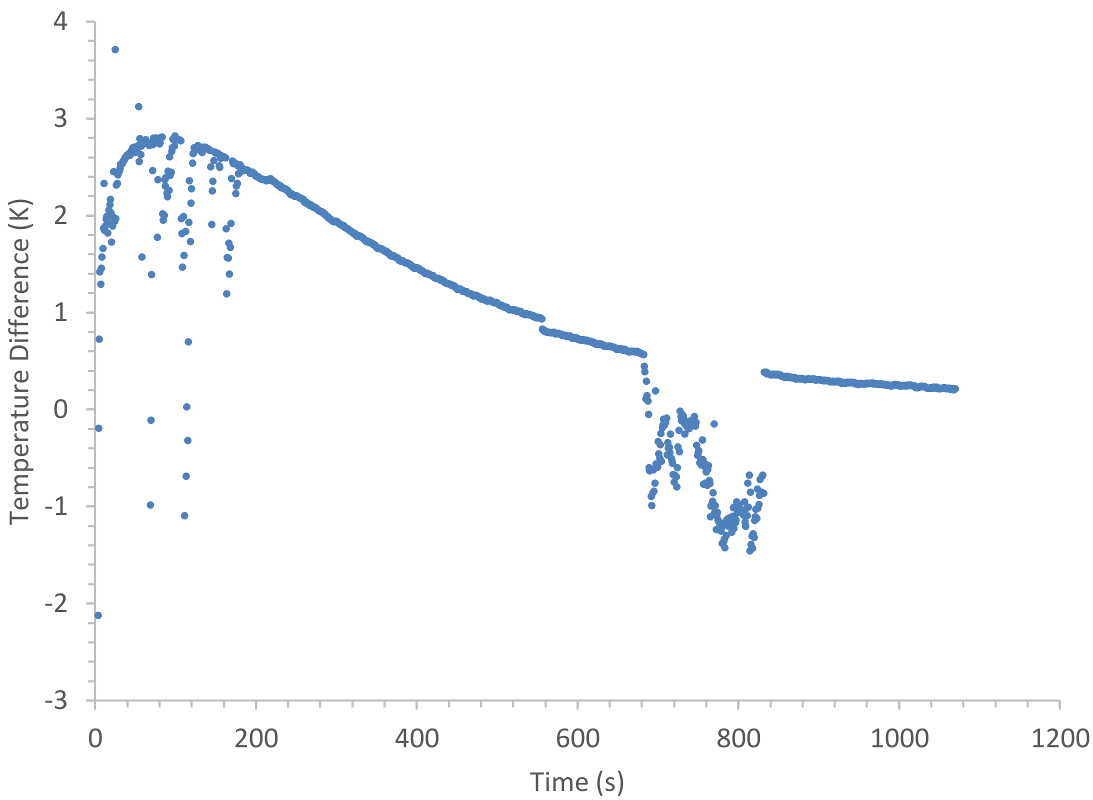

Figure 4.16 TC1-TC2 for 7 minute irradiation of pentachloride crystal at 865 nm and 2.07 W incident on the crystal

The third experiment performed with the pentachloride crystal involved irradiation at a wavelength of 832 nm. The Ti-Sapph. laser gave an output power of 1.6 watts. This resulted in an incident power of 1.47 W on the crystal. The irradiation lasted for 7 minutes. A graph displaying the analyzed data for this collection has been included in Figure 4.17.

The experiment gave a heating result. At a few isolated points, unstable readings from TC1 might give the impression of a sample cooler than the reference after the shutoff of the laser, but this is most likely a result of an equipment problem and these data points by themselves are not sufficient evidence to indicate refrigeration.

The fourth and final experiment performed with this crystal involved irradiation at a wavelength of 802 nm. The Ti-Sapph. laser gave an output power of 1 W. This resulted in an incident power of 0.92 watts on the crystal. The irradiation lasted for 7 minutes. A graph displaying the analyzed data for this collection has been included in Figure 4.18.

Like the previous pentachloride experiments with this crystal, this experiment gave a heating result. There is no discernible evidence of refrigeration from this data. No data collections for the KPb_2Cl_5 sample provided cooling results.

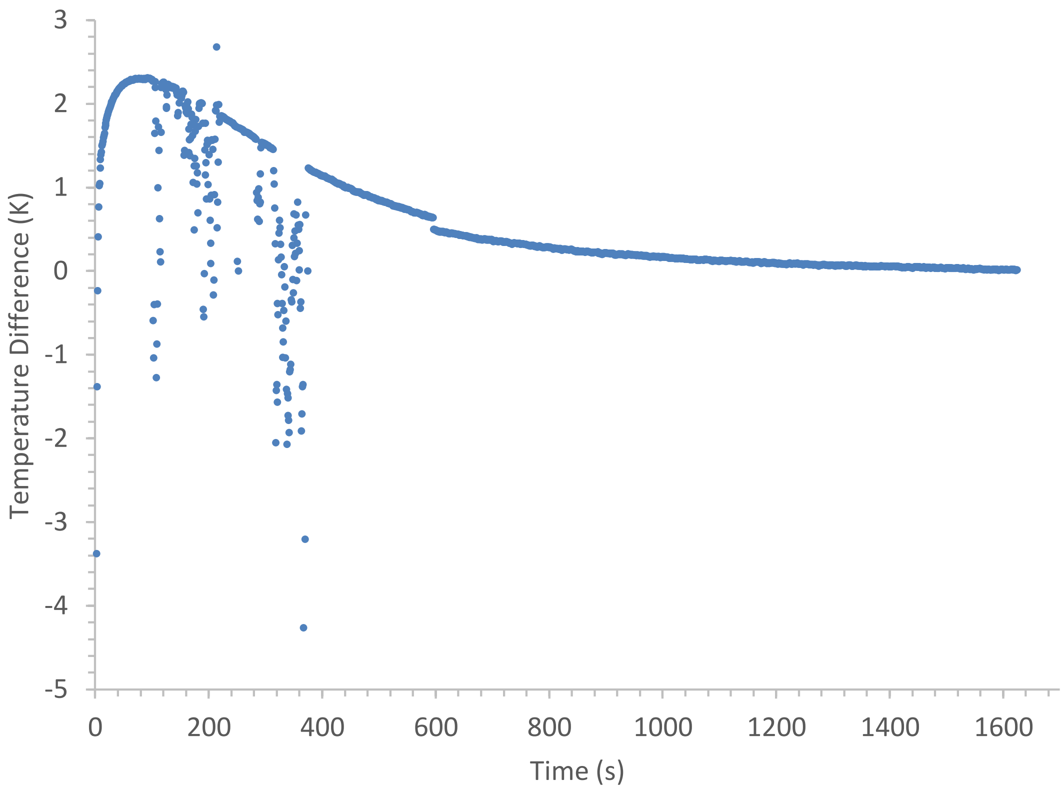

Figure 4.17 TC1-TC2 for 7 minute irradiation of pentachloride crystal at 832 nm with 1.47 W incident on the crystal

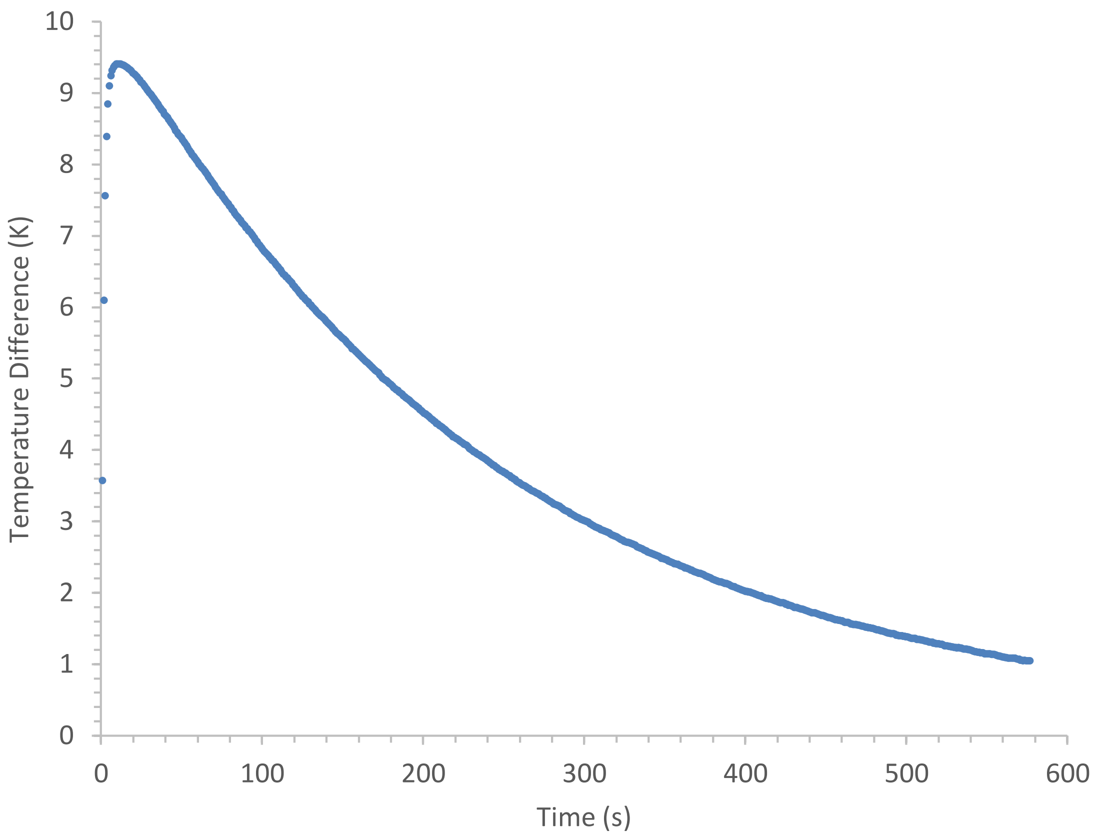

Figure 4.18 TC1-TC2 for irradiation of pentachloride crystal at 802 nm with 0.92 W incident on the crystal

CHAPTER 5: REFRIGERATION EXPERIMENTS IN ANOTHER Er^{3+} TRANSITION

5.1 Introduction

After the successful results of the investigation of cooling using the $^4I_{15/2}$-$^4I_{9/2}$ transition, an investigation of cooling using the $^4I_{15/2}$-$^4I_{13/2}$ transition was a logical continuation of the work. This transition is magnetic dipole allowed and has high oscillator strength, several orders of magnitude higher than the $^4I_{15/2}$-$^4I_{9/2}$ transition and should provide much more effective cooling. The selection rules for L-S coupling ($\Delta S = 0$, $\Delta L = 0, \pm 1$ and $\Delta J = 0, \pm 1$ but not 0 to 0) show that this transition does not violate any selection rule whereas the $^4I_{15/2}$-$^4I_{9/2}$ transition is not allowed under the selection rules for ΔJ, the change in total angular momentum.

That the $^4I_{15/2}$-$^4I_{13/2}$ transition is strongly allowed in comparison to the $^4I_{15/2}$-$^4I_{9/2}$ transition is reflected in the transition intensities. The $^4I_{15/2}$-$^4I_{13/2}$ transition has an intensity of $37{,}761 \times 10^{-8}$ D^2 while the $^4I_{15/2}$-$^4I_{9/2}$ transition has an intensity of less than 1.0×10^{-8} D^2; where the transition intensity is given in D^2 ($Debye^2$) (Hasan & Richardson, 1982).

Cooling with the $^4I_{15/2}$-$^4I_{13/2}$ transition has been attempted by another group but in pentachloride crystals, KPb_2Cl_5:Er (Condon, Bowman, O'Conner, Quimby, & Mungan, 2009). This chapter presents our attempts using the $^4I_{15/2}$-$^4I_{13/2}$ transition of Cs_2NaYCl_6:Er^{3+} for laser cooling.

The experiments to investigate cooling using the ${}^4I_{15/2}$-${}^4I_{13/2}$ transition were significantly different as compared to the experiments to investigate the ${}^4I_{15/2}$-${}^4I_{9/2}$ transition. The Ar-ion and Ti-Sapph. lasers used for ${}^4I_{15/2}$-${}^4I_{9/2}$ transition experiments did not cover the wavelength range required to investigate the ${}^4I_{15/2}$-${}^4I_{13/2}$ transition, $\lambda > 1500$ nm. Thorlabs Inc. kindly loaned the group a laser that covered some of the desired IR range, $\lambda \sim 1500$ nm to 1600 nm.

The experiments conducted exhibited cooling in this transition, although by few hundredths of a degree K. The extent of cooling achieved depends on the time of laser irradiation in a nontrivial way. Therefore, we studied cooling as a function of the total irradiation time of the sample by the cooling laser. In this chapter, the experiments and results will be described briefly but not in the same detail that was done for the ${}^4I_{15/2}$-${}^4I_{9/2}$ transition of Cs_2NaYCl_6:Er^{3+}.

5.2 Refrigeration Experiments in the ${}^4I_{15/2}$-${}^4I_{13/2}$ Transition in Cs_2NaYCl_6:Er^{3+}

As mentioned in chapter 2, for the cooling experiments using the ${}^4I_{15/2}$-${}^4I_{13/2}$ transition, a tunable diode laser, the TLK-L1550M, was used to provide the pump beam, this laser was on loan from Thorlabs. This laser had a center wavelength of 1550 nm and the tunable cavity and diffraction grating allowed the selection of the output across a wide wavelength range from 1500 nm to 1600 nm. The cavity output was equipped with a fiber optic cable to allow for easier positioning of the beam.

Figure 5.1 displays the raw data collected during one of the laser cooling experiments using the $^4I_{15/2}$-$^4I_{13/2}$ transition. As usual, the vertical axis displays the temperature difference between the thermocouple, TC1 which measures temperature of the sample and the thermocouple TC2, which measures the sample's surrounding. A positive value on the vertical axis indicates that the sample is warmer than its surrounding. A negative value indicates that the sample is cooler than its surrounding. The horizontal axis displays time in seconds and zero on the horizontal axis corresponds to the shutoff of the laser.

For obvious reasons, the crystal used for these experiments was the same crystal that provided the best results during the $^4I_{15/2}$-$^4I_{9/2}$ cooling experiments, presented in chapter 4. It had a cross sectional area of ~18 mm^2 and a concentration of Er of 80 percent (stoichiometric). The wavelength of the laser light was tuned to 1599 nm and the crystal was irradiated for a duration of 20 minutes. The power incident on the chamber was 40.0 mW (P_{irr} = 36.8 mW). As 1599 nm was near the upper limit of the covered wavelengths and the attainable power decreased as the wavelength approached that limit, a higher power incident on the crystal was not possible.

The graph in Figure 5.1 indicates cooling measured in hundredths of a degree Kelvin. The temperature difference is small compared to the cooling obtained using the $^4I_{15/2}$-$^4I_{9/2}$ transition of $Cs_2NaYCl_6:Er^{3+}$, which was measured in several degrees K, more than two orders of magnitude better. However, it is slightly better than, but comparable to, the result reported by Bowman's group at the Naval Research Lab using the $^4I_{15/2}$-$^4I_{13/2}$ transition of Er in KPb_2Cl_5 (Condon, Bowman, O'Conner, Quimby, & Mungan, 2009).

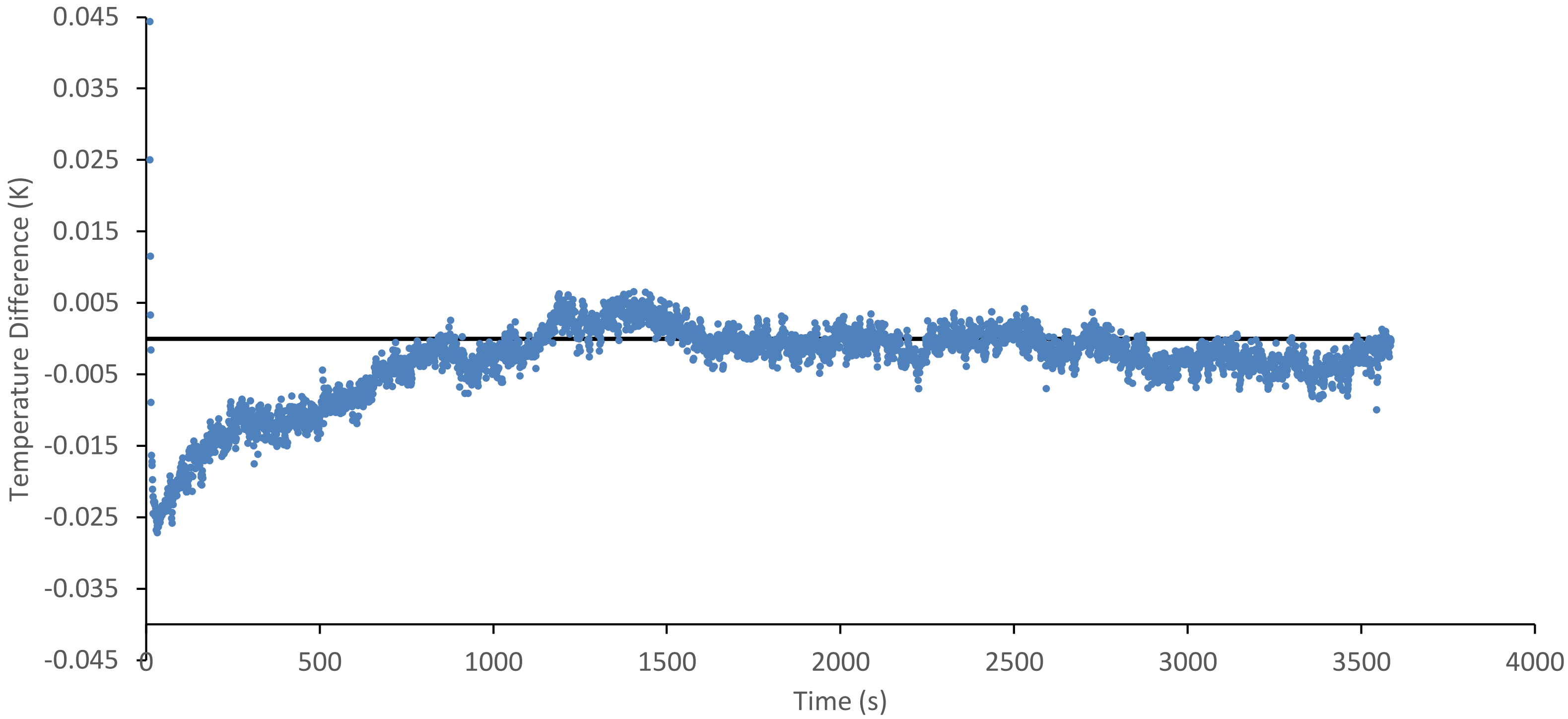

Figure 5.1 Results from a laser cooling experiment in the ${}^4I_{15/2}$-${}^4I_{13/2}$ transition. λ_{irr} = 1599 nm, t_{irr} = 20 min, P_{irr} = 36.8 mW. A positive value on the y-axis indicates that the sample is hotter than its surrounding. A negative value on the y-axis indicates that the sample is cooler than its surrounding.

Bowman's group used a sample that was in the shape of a cylinder with a cross sectional area of ~7.1 mm^2 and a length of 13.6 mm. The concentration of Er in their crystal is 3.6×10^{19} cm^{-3}. Their irradiation lasted for ~6 minutes. They report that their sample absorbed 5.3 mW. Bowman's group obtained their best cooling result irradiating their sample with a wavelength of 1567.6 nm (Condon, Bowman, O'Conner, Quimby, & Mungan, 2009). Our crystal, as mentioned above, has a cross sectional area of ~18 mm^2 and a length of ~10 mm. The concentration of Er in our crystal is ~6.5×10^{20} cm^{-3}. Our best result was obtained with a 20 minute irradiation. The power incident on our crystal was 36.8 mW. Our best cooling result with this transition was obtained with an irradiating wavelength of 1599 nm.

Two more wavelengths were attempted using the same crystal. Both were in a range where cooling was expected. Figures 5.2 and 5.3 display the data collected while irradiating the sample at wavelengths of 1577 nm and 1570 nm respectively. The crystal was irradiated for a duration of 30 minutes at a wavelength of 1577 nm. The power incident on the crystal was P_{irr} = 59.8 mW. Once again, the crystal was irradiated for a duration of 30 minutes but at a wavelength of 1570 nm. The power incident on the crystal was P_{irr} = 64.4 mW. Laser irradiation with both of these wavelengths resulted in heating the crystal.

For a direct comparison with Figure 5.1, where cooling is observed, the plots start at t= 0 s and span the same temperature difference along the y-axes. Pumping at these wavelengths significantly heated the sample and it took more than 1000 s to return to equilibrium temperature in both cases. A red region has been included in both Figures

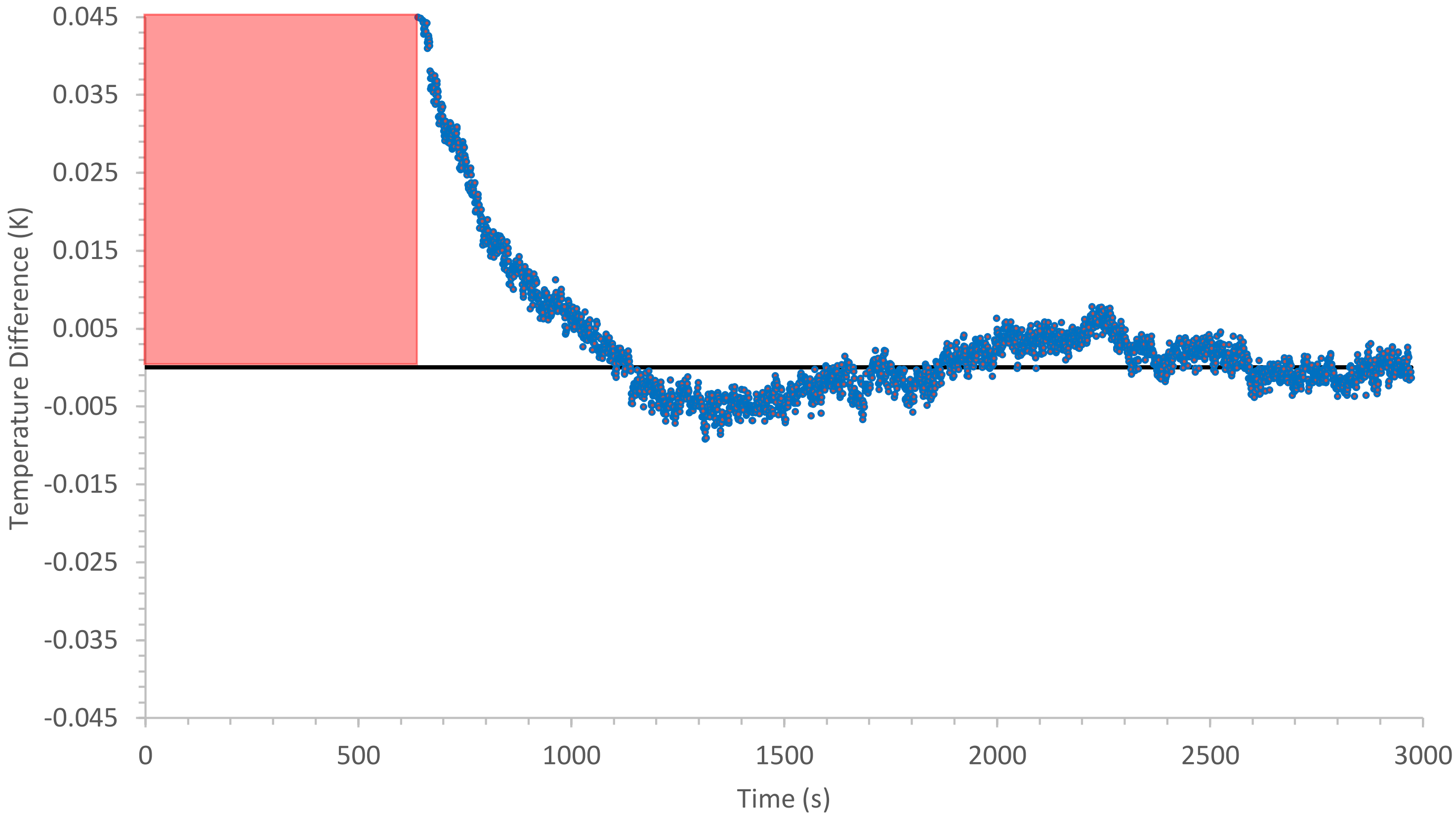

Figure 5.2 Results from a laser cooling experiment in the $^4I_{15/2}$-$^4I_{13/2}$ transition. λ_{irr} = 1577 nm, t_{irr} = 30 min, P_{irr} = 59.8 mW. For a direct comparison with Figure 5.1, where cooling is observed, the plot starts at t= 0 s and spans the same temperature difference along the y-axis. Pumping at this wavelength significantly heated the sample and it took more than 1000 s to return to equilibrium temperature.

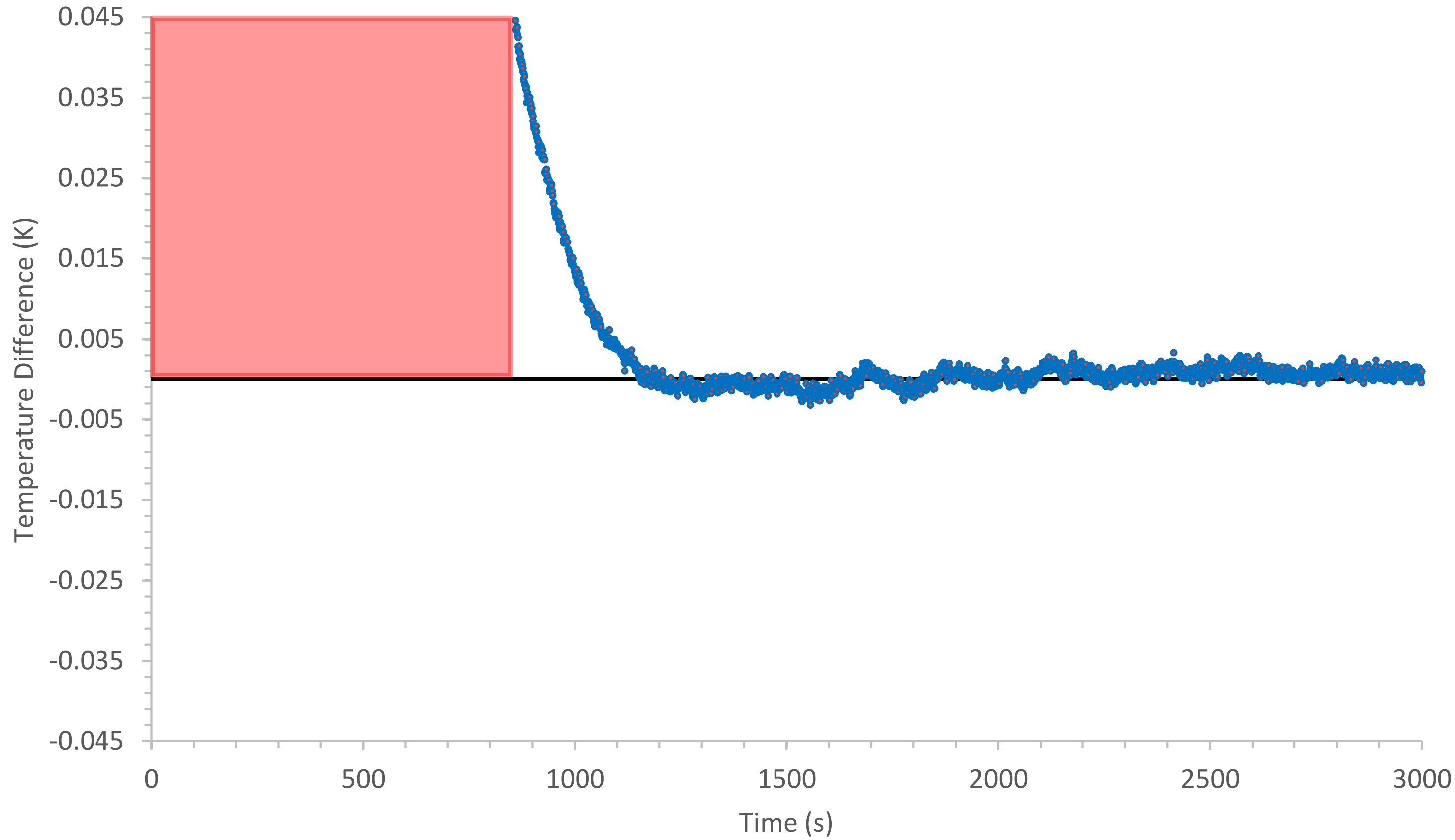

Figure 5.3 Results from a laser cooling experiment in the $^4I_{15/2}$-$^4I_{13/2}$ transition. λ_{irr} = 1570 nm, t_{irr} = 30 min, P_{irr} = 64.4 mW. Once again, for a direct comparison with Figure 5.1, where cooling is observed, the plot starts at t= 0 s and spans the same temperature difference along the y-axis. Pumping at this wavelength significantly heated the sample and it took more than 1100 s to return to equilibrium temperature.

5.2 and 5.3 where the data is not visible on the graphs due to the selected limits on the y-axes. The data presented in Figure 5.1 provided the best cooling results that we were able to obtain for the $^4I_{15/2}$-$^4I_{13/2}$ transition. Figure 5.4 displays the absorption and emission profile of the $^4I_{15/2}$-$^4I_{13/2}$ transition in Cs_2NaYCl_6:Er^{3+} at room temperature with the wavelengths of the irradiations, 1570 nm, 1577 nm, and 1599 nm, presented in figures 5.1-5.3, marked by vertical lines. The emission data was collected by a previous member of the group. No direct comparison between the absorption and emission intensities can be made except for the relative intensities.

An investigation of achievable cooling temperature as a function of the time of laser irradiation was conducted using the same experimental setup. The wavelength of the laser light was set to 1599 nm, where the most efficient cooling was observed, for the entire set of experiments. The incident power on the chamber was 40 mW for all of the experiments (P_{irr} = 36.8 mW, incident on the crystal). The time of irradiation was varied from one collection to the next ranging from 4 minutes to 20 minutes. The data has been presented in Figure 5.5. The vertical axis displays the temperature difference which corresponds to the voltage difference from thermocouples TC1 and TC2. It should be noted that this difference was adjusted to the initial voltage difference between the two thermocouples. The horizontal axis displays the time in seconds and is set such that the time of 0 seconds corresponds to the shutoff of the pump diode laser. The collection which appears to give the best result is the 20 minute irradiation.

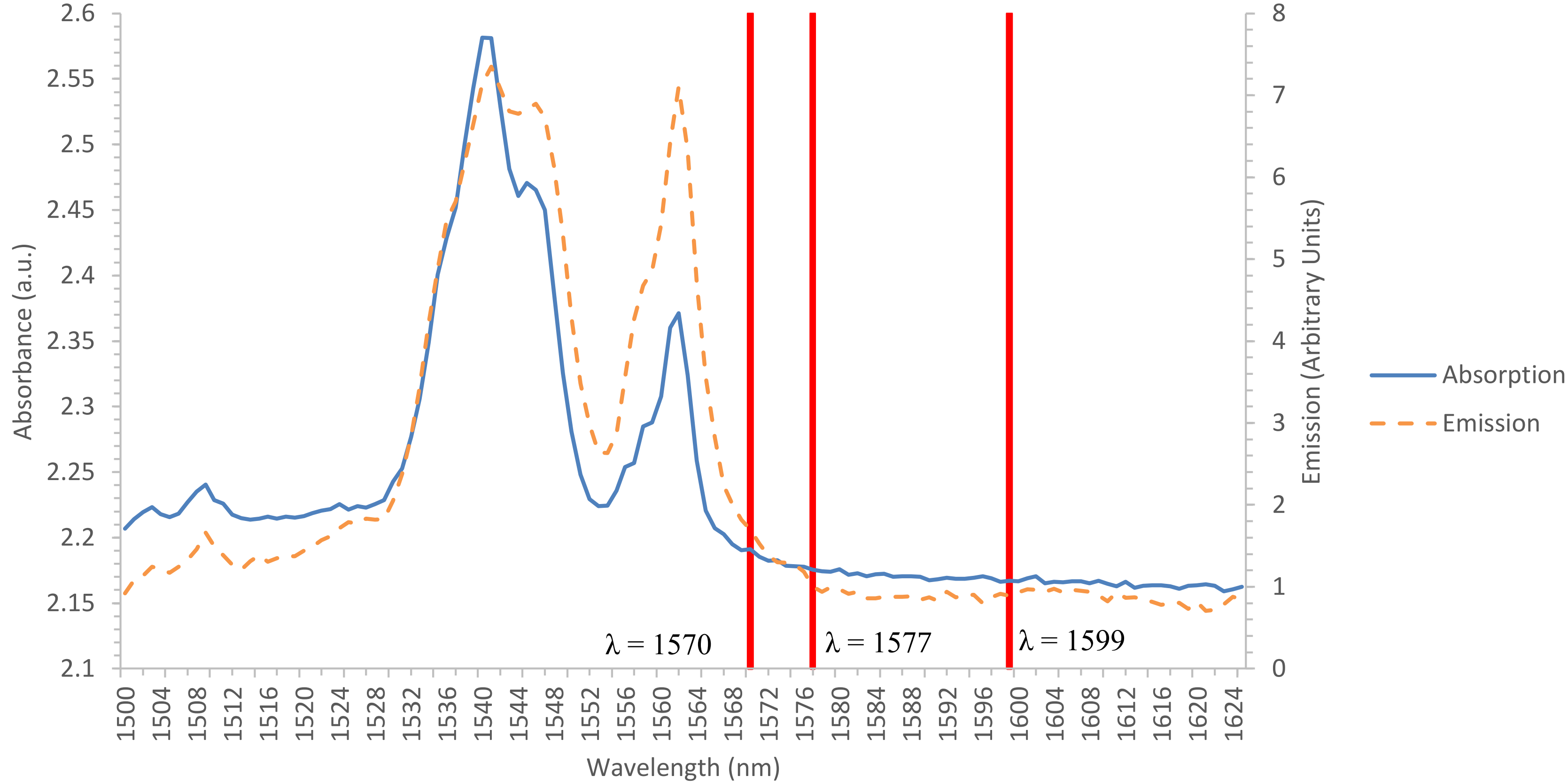

Figure 5.4 The absorption/emission spectrum of the the $^4I_{15/2}$-$^4I_{13/2}$ transition in in Cs_2NaYCl_6:Er^{3+} with vertical lines marking the three wavelengths used in the irradiations presented in Figures 5.1-5.3: 1570 nm, 1577 nm, and 1599 nm. No direct comparison between the absorption and emission intensities can be made except for the relative intensities.

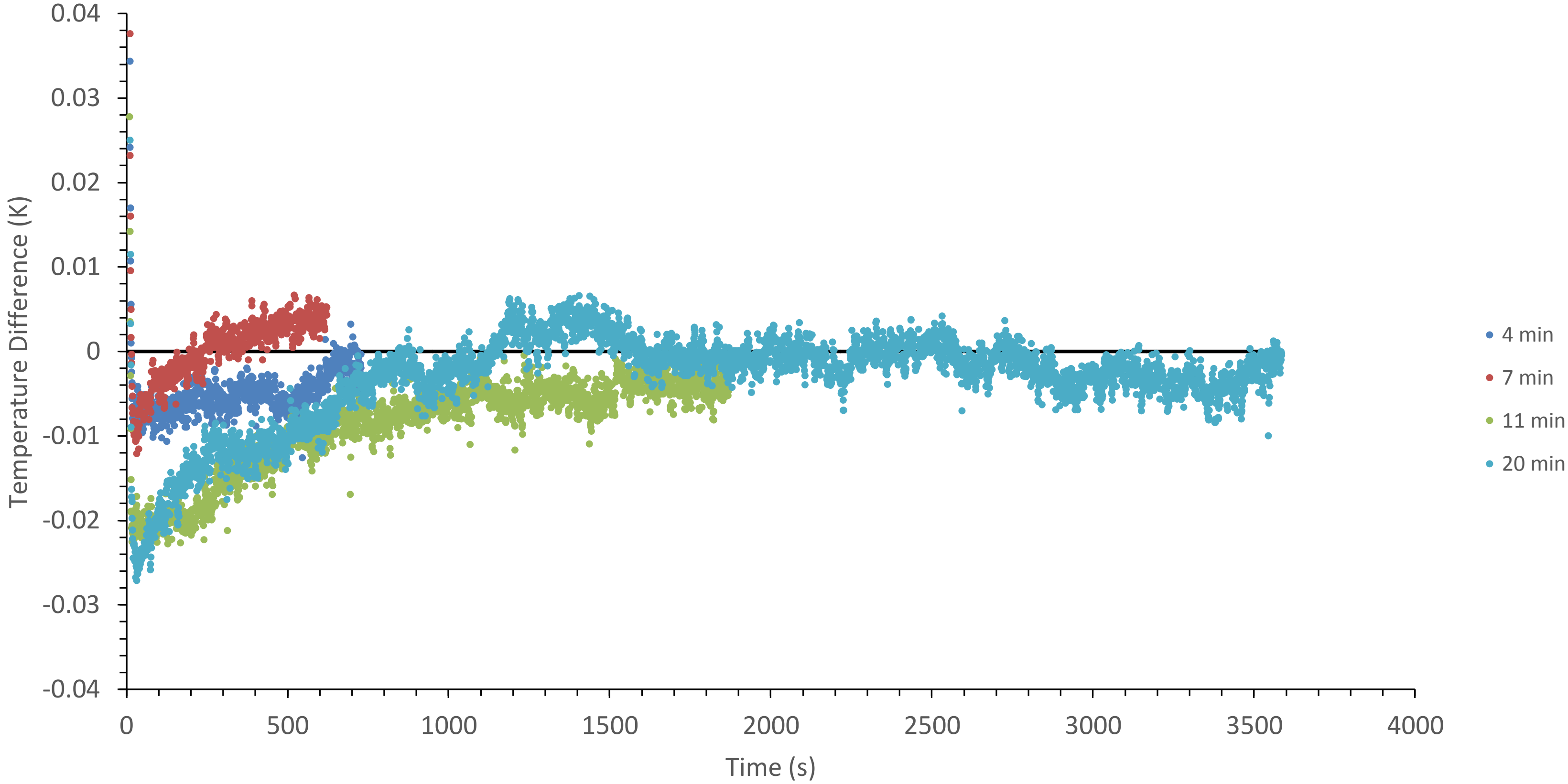

Figure 5.5 Time dependence results in the $^4I_{15/2}$-$^4I_{13/2}$ transition

The attainable power output from the laser decreased as the wavelength approached the upper limit of the tunable range, λ_{max} = 1600 nm. Even operating the laser at a current of ~690 mA, much higher than the 500 mA allowed upper limit, with kind permission from Thorlabs, gave a maximum power output of 40 mW. The pump diode laser had power variations of 1 percent over a period of 30 s. Over an extended period of 24 hours power variations can be as high as 10 percent (Thorlabs, 2014).

The tunable range of the laser extended from 1500 nm to 1600 nm. A wavelength dependence investigation was not completed in our desired wavelength region; λ_{irr} ~1675 nm was well beyond the operational limit of the diode laser on the longer wavelength side; λ_{max} = 1600 nm.

As shown above, data was collected while irradiating the crystal at more than one selected wavelength with varying incident power. This was intentionally done at the maximum available power at each wavelength to assure that increasing the laser power would not give any improved cooling results. This was necessitated by the low operational power of the diode laser.

Ultimately, the diode laser was returned to Thorlabs. As previously mentioned, cooling results obtained for the $^4I_{15/2}$-$^4I_{13/2}$ transition, while comparable to the results obtained by Bowman's group, were small compared to the unexpectedly larger temperature differences achieved using the $^4I_{15/2}$-$^4I_{9/2}$ transition. At that point we found it convenient to return to work on the $^4I_{15/2}$-$^4I_{9/2}$ transition.

CHAPTER 6: CONCLUSIONS

The objective of this study was to investigate the potential of erbium based solid state materials for laser refrigeration in bulk material. The lowest reported temperature attained through laser cooling of a bulk solid, 110 K, has been obtained with the use of ytterbium in a $LiYF_4$ crystal (Yb^{3+}: 5 mol%) (Seletskiy, et al., 2011). However, the ground state crystal field splitting of Yb^{3+} ($4f^{13}$), 180 cm^{-1}, limits the cooling that can be achieved with that ion. The ground state crystal field splitting of Er^{3+} ($4f^{11}$) provides lower lying energy levels which should allow for a lower minimum attainable temperature. In our cubic crystal, the Er^{3+} ground state splitting is such that the lowest two states are separated by 25 cm^{-1}. At low temperature, these states play the role of cooling the crystal. This energy difference could be further tailored to be less than 25 cm^{-1}. Therefore, Er^{3+} based solid state systems should provide lower attainable temperatures than Yb^{3+} based systems which has an energy difference of 180 cm^{-1}.

The work presented in previous chapters demonstrates laser cooling of a solid in a Cs_2NaYCl_6:Er^{3+} crystal. The cooling experiments utilizing the $^4I_{15/2}$-$^4I_{9/2}$ electronic transition, in the 870 nm region, presented in chapter 4, yielded an observed temperature difference of ~6.2 K. This result was obtained with 2.21 W from the laser incident on the crystal. The irradiation lasted for 20 minutes and the laser light was tuned to a wavelength of 870 nm. The crystal had a cross sectional area of ~18 mm^2 and had an 80 percent stoichiometric concentration of erbium. A temperature difference of ~6.2 K is an improvement of an order of magnitude in cooling an erbium based bulk material as compared to previous results reported by Fernandez et. al. Fernandez's group at the

Escuela Técnica in Spain obtained a temperature difference of ~0.7 K using the $^4I_{15/2}$-$^4I_{9/2}$ transition of erbium in a KPb_2Cl_5 crystal (0.5 mol% $ErCl_3$) (Fernández, García-Adeva, & Balda, 2006). We achieved a cooling result with this transition of erbium even though it was considered an unlikely transition to provide cooling due to its forbidden nature and despite the additional precautions required to protect the hygroscopic crystal, making the experiments more difficult. The mechanism of cooling in this transition is contested in this field and is subject to further investigation.

We attempted to reproduce Fernandez's result. Our investigation of laser cooling in the $^4I_{15/2}$-$^4I_{9/2}$ transition of the $KPb_2Cl_5:Er^{3+}$ (~1%) crystal did not yield any positive results. All of the experiments yielded heating results. Thus, we did not reproduce the results of Fernandez's group.

Investigation of laser cooling in our system, the erbium based elpasolite, $Cs_2NaYCl_6:Er^{3+}$, using the $^4I_{15/2}$-$^4I_{13/2}$ transition (chapter 5) at wavelengths ~ 1500 nm, was pursued, as Bowman's group at the Naval Research Lab obtained a cooling temperature difference of ~.014 K using the $^4I_{15/2}$-$^4I_{13/2}$ transition of erbium in a KPb_2Cl_5 crystal (Condon, Bowman, O'Conner, Quimby, & Mungan, 2009). Our results verified Bowman's result with a slightly better temperature difference of ~.015 K. Higher power lasers at longer wavelengths may provide improved results. It should be noted that this transition was considered far more likely to provide efficient cooling. However, cooling in this transition yielded a much smaller temperature difference in comparison to the $^4I_{15/2}$-$^4I_{9/2}$ transition. Cooling using the $^4I_{15/2}$-$^4I_{13/2}$ transition warrants further future investigation.

From several methods to detect laser cooling, we chose direct temperature measurement using two thermocouples. The two thermocouples provide the measurement of the crystal's temperature and the temperature of its immediate surrounding environment. This setup was based on a vacuum chamber with several optical windows to access the laser. The crystal was positioned at the center of the chamber. The vacuum chamber and the thermocouple connections were built or assembled in our lab or Temple University's machine shop. The infrared lasers used in these experiments were, Thorlabs (λ~1500 nm) and Coherent (Ti-Sapph. laser) (λ~870 nm).

Other possible methods of measurement of cooling include photothermal deflection, fluorescence line narrowing and thermal imaging. Photothermal deflection requires passing a probe beam through the sample. This will deflect a laser beam passing through the sample. Due to the hygroscopic nature of our crystal, surface depositions made this method impractical. Other possible methods of measurement of cooling such as thermal imaging and fluorescence line narrowing were not attempted due to time limitations and other constraints.

Our cooling results could be improved by polishing the crystal surface. However, it was not possible to the desired degree because the crystals were hygroscopic. Due to the hygroscopic nature of the crystal, surface deterioration results in a decrease in power absorbed by the crystal and increased intensity of scattered light. This increased scattered light in the chamber increases the absorption by the chamber and, hence, increases the surrounding temperature. The hygroscopic nature of the crystal also made the surfaces highly scattering. This resulted in an unknown amount of the incident light scattered by the crystal. Therefore quantitative calculations of power absorbed by the crystal and the efficiency of cooling could not be performed.

We attempted to improve our cooling temperature by using different variations of our experimental setup. Some notable attempts were as follows. In one such attempt, a smaller crystal, with a cross sectional area of ~2 mm^2 was used in the hope that the smaller volume, allowing for irradiation of a larger portion of the crystal, would improve the obtainable cooling. However, this crystal had a 60 percent stoichiometric concentration of erbium and therefore no direct comparison can be made. Another attempt involved improving the optics using tight focusing conditions. However, no noticeable improvement was observed from these attempts. The data from these experiments has not been presented in this dissertation. It may be presented in future work from this group.

The mechanism of laser cooling in this highly forbidden transition, $^4I_{15/2}$-$^4I_{9/2}$, is disputed. Therefore, an experiment to determine the mechanism of cooling by measurement of fluorescent emission of light from the sample while it is irradiated at 870 nm by an excimer pumped dye laser was in progress in our lab. These experiments were terminated by the movement of the lab to the new building and could be attempted in the future once the labs come into operation in the new building, SERC.

BIBLIOGRAPHY

(2014). Retrieved from Thorlabs: http://www.thorlabs.com/thorcat/21000/TLK-L1550M-Manual.pdf

Condon, N. J., Bowman, S. R., O'Conner, S. P., Quimby, R. S., & Mungan, C. E. (2009). Optical Cooling in ER3+:KPb2Cl5. *Optics Express*, 5466-5472.

De Bartolo, B. (1968). *Optical Interaction in Solids.* John Wiley & Sons.

Djeu, N., & Whitney, T. (1981). Laser Cooling by Spontaneous Anti-Stokes Scattering. *Physical Review Letters*, 236-239.

Epstein, R. I., Buchwald, M. I., Edwards, B. C., Gosnell, T. R., & Mungan, C. E. (1995). Observation of laser-induced flourescent cooling of a solid. *Nature*, 500-503.

Fernández, J., García-Adeva, A. J., & Balda, R. (2006). *Physical Review Letters*.

Fernández, J., García-Adeva, A. J., & Balda, R. (2012). Anti-Stokes laser-induced cooling in rare-earth doped low phonon materials. *Optical Materials*, 579-590.

Freeman, A. J., & Watson, R. E. (1962). Theoretical Investigation of Some Magnetic and Spectroscopic Properties of Rare-Earth Ions. *Physical Review*, 2058-2075.

Hasan, Z., Biyikli, L., Sellars, M. J., Khodaparast, G. A., Richarson, F. S., & Quagliano, J. R. (1997). Energy transfer and upconversions in cubic Cs2NaYCl6:Er3+ and Cs2NaErCl6. *Physical Review B*, 4518-4528.

Hasan, Z.-U., & Richardson, F. S. (1982). Optical absorption spectra and crystal field analysis of Er3+ in the Cs2NaErCl6 system. *Molecular Physics*, 1299-1326.

Hufner, S. (1978). *Optical Spectra of Transparent Rare Earth Compounds.* New York: Academic Press.

Kiel, A. (1962). Temperature-Dependent Linewidth of Excited States in Crystals. I. Line Broadening due to Adiabatic Variations of the Local Fields. *Physical Review*, 1292-1297.

Nielson, C. W., & F, K. G. (1963). *Spectroscopic coefficients for pn, dn, and fn Configurations.* Cambridge, Mass.: MIT Press.

Nielson, C. W., & Koster, G. F. (1963). *Spectroscopic Coefficients for the pn, dn, and fn Configurations.* Cambridge, MA: MIT Press.

Patterson, W., Bigotta, S., Sheik-Bahae, M., Parisi, D., Tonelli, M., & Epstein, R. (2008). Anti-Stokes luminescence cooling of Tm3+ doped BaY2F8. *Optics Express*, 1704-1710.

Pringsheim, P. (1929). Zwei bemerkungen uber den unterschied von lumineszenz- und temperaturstrahlung. *Z. Phys.*, 739-746.

Seletskiy, D. V., Melgaard, S. D., Epstein, R. I., Di Lieto, A., Tonelli, M., & Sheik-Bahae, M. (2011). Local laser cooling of Yb:YLF to 110 K. *Optics Express*, 18229-18236.

Woods, A. M., Sinkovits, R. S., Charpie, J. C., Huang, W. L., Bartram, R. H., & Rossi, A. R. (1993). Computer Modeling of the Optical Properties of Substitutional Chromium Impurities in Halide Elpasolites. *J. Phys. Chem. Solids*, 543-552.

Wybourne, B. G. (1965). *Spectroscopic Properties of Rare Earths.* New York: Interscience Publishers.

Zhang, J., Li, D., Chen, R., & Xiong, Q. (2013). Laser cooling of a semiconductor by 40 kelvin. *Nature*, 504-508.

APPENDIX A: PROGRAMS USED TO CALCULATE ENERGY LEVELS

The programs used to calculate the energy levels of Er in Cs_2NaYCl_6 were developed elsewhere for other studies. These programs, in their original form, were incompatible with modern computer systems. The input and output data from the earlier forms of the programs were contained on punch cards and magnetic tape. The programs have been modified to use input and output data files suitable for modern operating systems. A table displaying the user modified input files and the output files relevant to these calculations is included in Table A.1 at the end of this appendix. A flow diagram displaying the order in which the programs should be run and which program output is used as input by other programs appears in Figure A.1 which has been included at the end of this appendix.

The program chain begins with BCFMAN which produces the state labels for the ψ[SL]J basis. The basis is derived from the ψ[SL] terms from Nielson and Koster. A file has been added to select the stage of BCFMAN. The BCFMAN SELECT RUN.DAT file should contain a 1 to select the first stage and a 2 to select the second stage.

FFMAT calculates the electrostatic matrices, in the case of f^N configurations, in terms of the Racah radial integrals. It makes use of the output of the BCFMAN program.

SOCL calculates the spin-orbit coupling matrix elements. The reduced matrix elements of V^{11} given in Nielson and Koster are used in addition to the output of the BCFMAN program.

CI calculates the configuration interaction contribution. It calculates the individual matrices for the α, β, and γ parameters.

Previous documentation lists a conversion program which should read the output files from the previous programs and use the data to prepare one of the input files for MTXDIAG, the next program. The code for that program was not available at the time that this dissertation was written. However, the conversion program is not necessary. The program user can copy the output of the previous programs and paste the data into an input file for use in MTXDIAG.

MTXDIAG gathers together all the various Hamiltonian component matrices. Each matrix is multiplied by its appropriate parameter. The matrices are summed to produce the total Hamiltonian matrix which is diagonalized. This gives the energies of states and the associated wavefunctions as linear combinations of the $|\alpha[SL]JM\rangle$ states. This first run gives the barycenter values before the crystal field contribution is applied. For reasons that have yet to be determined, MTXDIAG compiled successfully but would only successfully run in debug mode during its first stage.

UMAT calculates the reduced U matrix elements. It makes use of output from the first stage of BCFMAN and the first stage of MTXDIAG.

CONVERT makes use of output from the first stage of MTXDIAG to prepare input files for the second stage of BCFMAN and for HZERO. The file prepared for the second stage of BCFMAN is usable. However, the file created for HZERO is faulty and in its current form, HZERO does not make use of it.

BCFMAN at its second stage generates the state labels for the Barycenter crystal field states |τ[SL]JM>. Its input file is prepared by the CONVERT program.

HZERO sets up the diagonal matrices of barycenter eigenvalues appropriate for each set of crystal field blocked |τJM> states. While the convert program prepares a file that is meant to serve as input for HZERO, the file prepared will be faulty. The HZERO program makes use of the HZERO INP.DAT file instead.

BCCF calculates the matrix elements of $U_q^{(k)}$ for the |τJM> basis states of each crystal field block.

PARMZ allows the linear combination of several of the crystal field matrices produced by BCCF. The once reduced elements are taken from the output of UMAT

MTXDIAG in its second stage produces values after the crystal field contribution is applied. The Convert2 program accesses the output of the previous programs and prepares an input file for the second stage of MTXDIAG. This is used in addition to the user-prepared input file. Running MTXDIAG in debug mode is not necessary for its second stage.

Program	Input Files	Output Files
BCFMAN	BCFMAN1 INP A	BCFMAN1 OUT A
	BCFMAN2C INP	BCFMAN2 OUT A
	BCFMAN SELECT RUN	
FFMAT	FFMAT INP A	FFMAT OUT A
	BCFMAN1 OUT A	
SOCL	SOCL INP	SOCL OUT A
	BCFMAN1 OUT A	
CI	CI INP	CI OUT
	BCFMAN1 OUT A	
MTXDIAG	MTXDIAG1 INP	MTX 611
	MTXC1 INP	MTX 631
	MTXDIAG2 INP	MTX OUT
	MTXC2 INP	
	CONVERT IN	
UMAT	UMAT INP	UMAT OUT
	BCFMAN1 OUT A	
	MTX 631	
CONVERT	CONVERT IN	CONVERT OUT2
		BCFMAN2C INP
HZERO	BCFMAN2 OUT A	HZERO OUT
	HZERO INP	
BCCF	BCCF INP	BCCF OUT
	UMAT OUT	
	BCFMAN2 OUT A	
PARMZ	PARMZ INP	PARMZ OUT
	BCCF OUT	
CONVERT2	BCFMAN2 OUT A	MTXC2 INP
	HZERO OUT	
	PARMZ OUT	

Table A.1. The programs, user modified input files and output files used by those programs

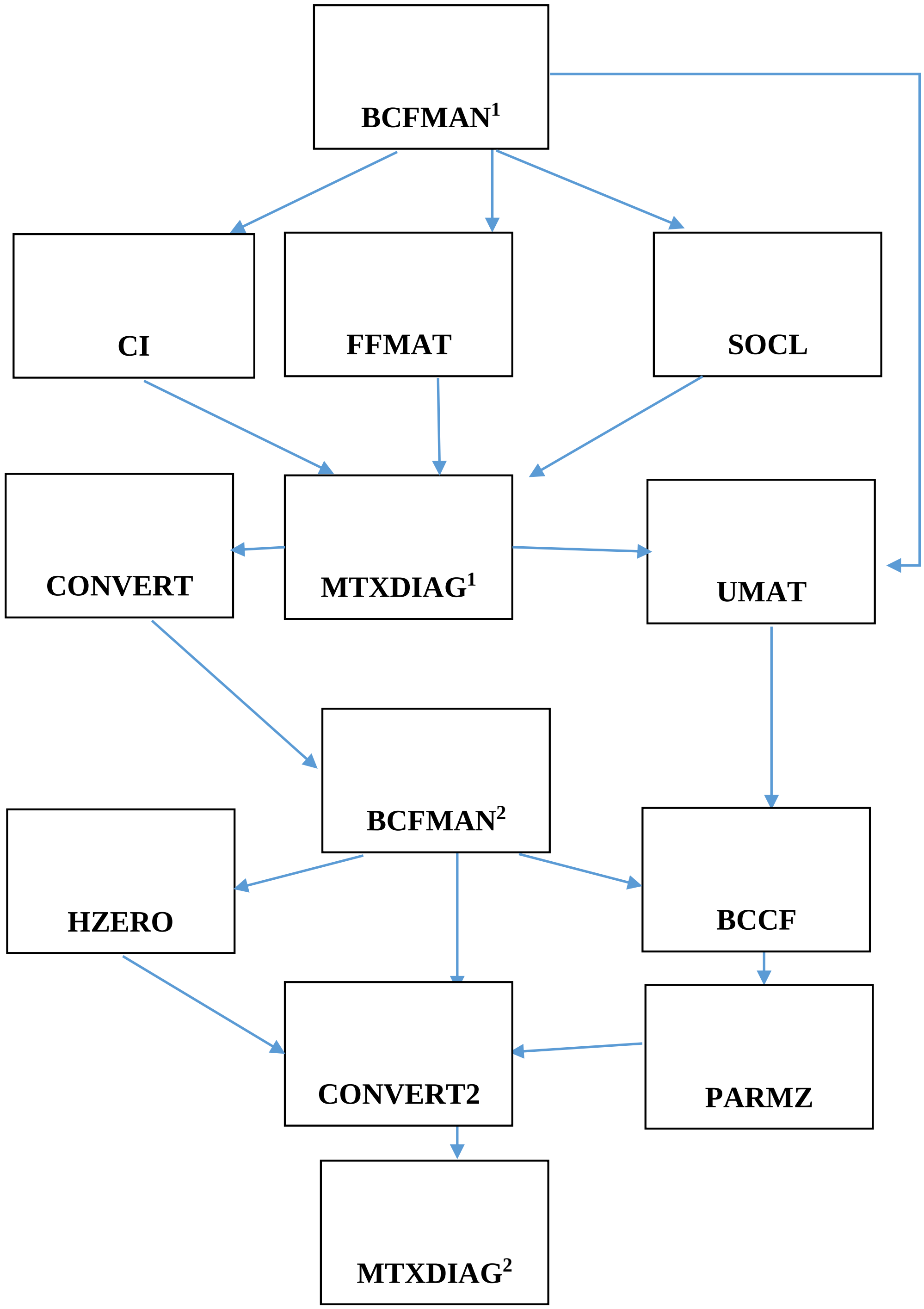

Figure A.1 A flow diagram showing the order of execution of the programs.

APPENDIX B: PERMISSIONS TO INCLUDE COPYRIGHTED MATERIAL

COHERENT.

10/1/15

I would like to request the below described material to be used in **Laser (Cooling) Refrigeration of Erbium Based Solid State Materials** by **Jonathan Lynch**

Image & Caption Requested:

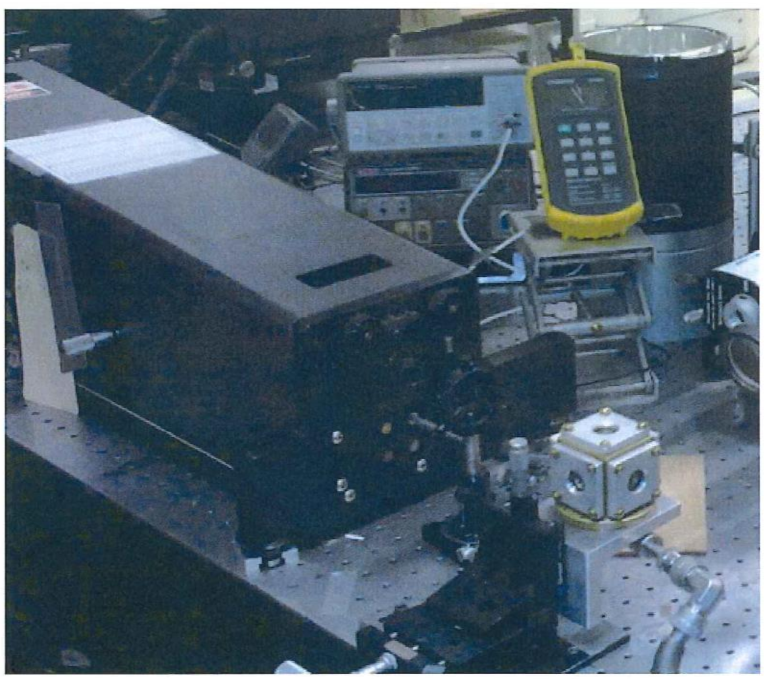

Figure 2.6 The photo of the experimental Setup for $^4I_{15/2}$-$^4I_{9/2}$ transition shows the vacuum chamber used to hold the sample and the Ti-Sapp laser and an iris can be seen in the upper left corner.

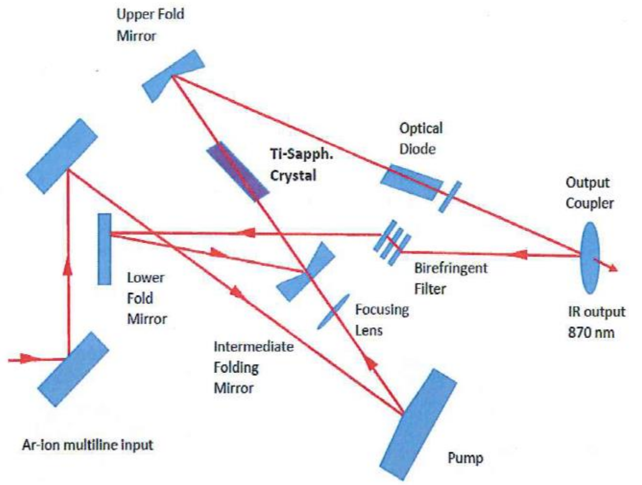

Figure 2.5 Diagram of Titanium-Sapphire laser (Coherent 899)

I hereby request permission to use the Coherent image listed above:

Jonathan Lynch

Jonathan Lynch

I hereby grant permission to use Coherent image listed above:

RSWood

Rosemarie Smith-Wood
Head of Global Communications, Coherent Inc.

tori_richmond@agilent.com <tori_richmond@agilent.com> Tue, Oct 20, 2015 at 1:29 PM
To: wendy_lowengrub@agilent.com
Cc: tub00079@temple.edu

Hi Jonathan,

Thank you for asking for permission to use the attached image and congratulations on getting to your dissertation.

As this is part of our brochure you are allowed to use this image as it appears in our literature. We ask that you cite the image as; Agilent Cary UV-Vis.

Sincerely,

Tori Richmond

Tori Richmond

Director Segment Marketing & Market Development

408-707-6059 mobile

Agilent Technologies, Inc.
Intellectual Property Group
5301 Stevens Creek Blvd, MS 1A-PB
Santa Clara, CA 95051

408-553-2772 telephone
408-553-2365 facsimile
jim_simon@agilent.com
www.agilent.com

James L Simon
Corporate Counsel

Agilent Technologies

October 14, 2015

Via email to: tub00079@temple.edu

To: Jonathan Lynch
Temple University

Dear Mr. Lynch,

It is my understanding that you are seeking permission to publish certain illustrations/images that you have listed in your email request (attached) and as to which Agilent owns the copyrights. I am pleased to advise that you have been granted permission to copy and republish Figure 2.4 (A Varian Cary 500 dual beam spectrophotometer) from the Varian Cary 100/300/400/500 Spectrophotometers brochure for use in your doctoral dissertation.

This consent extends to the above mentioned print and electronic content/imagery and all subsequent revisions of the above-referenced print and electronic content/imagery. This consent is conditioned upon the following source acknowledgement being included with each figure, with the year date being the year date shown on the original publication from which the figure was copied:

© Agilent Technologies, Inc. <year date>
Reproduced with Permission, Courtesy of Agilent Technologies, Inc.

By reproducing these materials, the authors acknowledge that the materials and the information contained therein are accepted "AS IS", and that Agilent does not make any representations or warranties of any kind with respect to the materials or the contained information and disclaims any responsibility for them as reproduced by you. You further acknowledge that Agilent Technologies has the right to terminate this consent if the terms of this consent are breached, or if the copied materials are altered, modified, or portrayed in any way that, in Agilent's opinion, is in poor taste or diminishes the reputation of Agilent or its products. Further, Agilent will not be liable for any damages, whether special, incidental, consequential, direct, indirect or punitive, resulting from/in connection with the use, copying/disclosure of the above referenced documentation.

Thank you for your interest in Agilent Technologies, Inc. and its products and services.

Sincerely,

Dominique Garcia

Dominique Garcia
Manager, Global Content Specialists

From:	VARGAS,CRISTINA (A-Santa Clara,ex1)
To:	VARGAS,CRISTINA (A-Santa Clara,ex1)
Subject:	Corporate/Legal/Use of spectrophotometer image in a PhD dissertation/Temple University/ Jonathan W. Lynch/PA/eg
Date:	Wednesday, October 14, 2015 9:14:03 AM

From: US,CONTACT (A-Americas,exgen1)
Sent: Friday, October 02, 2015 7:05 AM
To: SIMON,JIM (A-Labs,ex1)
Subject: Corporate/Legal/Use of spectrophotometer image in a PhD dissertation/Temple University/ Jonathan W. Lynch/PA/eg

Agilent's Corporate Contact Center is forwarding the email message below for your action. If you or someone in your department is not the correct owner, please confirm before the end of your current business day. Otherwise, you are accepting ownership of this request.

Sincerely,

Agilent Corporate Contact Center

Agilent Technologies, Inc.
Santa Clara, CA USA

877 424 4536 Toll Free
408 345 8474 Fax
www.agilent.com

From: JONATHAN W LYNCH [mailto:tub00079@temple.edu]
Sent: Thursday, October 01, 2015 7:49 PM
To: US,CONTACT (A-Americas,exgen1)
Subject: Use of spectrophotometer image in a PhD dissertation

Good evening,

I am a graduate student at Temple University. I am writing my doctoral dissertation and I would like to use part of a diagram that appears in a Varian brochure in that dissertation. I want to find out if there are any copyright restrictions that would be involved and find out which representative or department I would need to contact for permission.

The Varian Cary 500 spectrophotometer was used in some of my research.

I have attached the image as it would appear in my dissertation and the brochure from which it was adapted.

Can you tell me which representative or department I would need to contact to obtain any necessary permission?

Is there a specific way that I should cite a reference to Varian or Agilent in the captions?

Thank you very much for any information that you can provide,
Jonathan Lynch